MEASUREMENTS AND ANALYSIS OF FILM COOLING ON GAS TURBINE VANE ENDWALL AND SUCTION SURFACE

A Dissertation

by

CHAO-CHENG SHIAU

Submitted to the Office of Graduate and Professional Studies of
Texas A&M University
in partial fulfillment of the requirements for the degree of

DOCTOR OF PHILOSOPHY

Chair of Committee,	Je-Chin Han
Committee Members,	Hamn-Ching Chen
	Sai Chuen Lau
	Gerald L. Morrison
Head of Department,	Andreas A. Polycarpou

December 2017

Major Subject: Mechanical Engineering

ABSTRACT

Researchers in gas turbine field take great interest in the cooling performance on the first-stage vane in a more authentic configuration because of the complicated flow characteristics and intensive heat load that comes from the exit of the combustor. With the three-dimensional vane geometry and the corresponding wind tunnel design, a more realistic flow field can thus be simulated. The annular sector cascades were therefore selected and the Pressure-sensitive paint (PSP) technique was used to study the film cooling effectiveness on the endwall and vane's suction surface. On the other hand, PSP technique was also applied on a linear cascade to study the effect of upstream leakage injection angle on various endwall film cooling designs.

In the first part of the study, full-scale turbine vanes were used to construct a three-vane annular sector cascade. Two kinds of film cooling designs are attained through the layback fan-shaped and cylindrical holes dispersed on the vanes and endwalls. This study targets the film cooling effectiveness comparison on the inner endwall of turbine vane. Tests were performed under the mainstream Reynolds number 350,000; the related inlet Mach number is 0.09. Coolant-to-mainstream mass flow ratios (2%, 3%, 4%) and density ratios (1.0, 1.5) were examined. The results provide the gas turbine engine designer a direct performance comparison between two film-hole configurations on a full-scale vane endwall under the same amount of coolant usage.

The second part of the study is focused on the film cooling on the suction surface of a turbine vane under transonic flow condition. The experiments were performed in a

five-vane annular sector cascade. The exit Mach numbers were varied from 0.7, 0.9, and 1.1. Density ratios, ranging from 1.0, 1.5 to 2.0; three blowing ratios ranging from 0.7, 1.0, 1.6 for the suction surface were studied. Three rows of radial-angle cylindrical holes around the leading edge and two rows of compound-angle shaped holes on are the suction surface of the test vane. The results demonstrate the mix effects of coolant amount, density ratio, and exit Mach number on the film cooling as well as its interaction with the potential shock wave.

The third part of the study is to investigate the effects of upstream leakage injection angle on film cooling effectiveness of a turbine vane endwall with various film-hole designs. To simulate the upstream leakage flow between the combustor and the turbine vane, three potential leakage injection angles were studied: 30^o, 40^o, and 50^o. To explore the optimum endwall cooling design, five different film-hole patterns were tested: axial row, cross row, cluster, mid-chord row, and downstream row. Experiments were conducted in a four-passage linear cascade at the exit isentropic Mach number 0.5 corresponding to the inlet Reynolds number 380,000 based on turbine vane axial chord length. For a fair performance comparison, the coolant was fixed at mass flow ratio 1% and density ratio 1.5. The results provide the gas turbine designers a valuable information on how to select the best endwall cooling pattern with minimum cooling air consumption over a range of upstream leakage injection angles.

DEDICATION

This work is dedicated to my beloved parents, Wen-Sheng Shiau and Ping Tsai, and my lovely sister, Ju-Yu Shiau. My sweet family established me. I would not accomplish anything without their unconditional love and support in all things great and small.

ACKNOWLEDGEMENTS

I would like to sincerely thank the chair of my dissertation committee, Dr. Je-Chin Han, for the guidance and support throughout my whole journey at Texas A&M University. Dr. Han is such an exemplar that his discipline attitude toward research and his profound insights on both technical knowledge and life wisdom inspire me and influence me forever. I would like to thank Dr. Hamn-Ching Chen, Dr. Sai Chuen Lau, and Dr. Gerald L. Morrison not only for serving as my advisory committee members but as great instructors for the courses I took. In addition, I would like to thank Dr. Kuang-An Chang's attendance to my dissertation defense and his advice.

Thanks also to my friends and colleagues in Turbine Heat Transfer Laboratory at Texas A&M University, including all the previous and present lab members who had ever helped me before. I want to extend my gratitude especially to Andrew F Chen and Nafiz Chowdhury. It was truly a great pleasure for me to have brilliant guys like you two as peers collaborating to face challenges, as well as finish and deliver numerous research projects together.

I like to thank my first roommate, Ping Tzeng. Thank you for smoothly leading me to accommodate the new life in the United States and be familiar with the cultures in Texas. I want to express my appreciation to my second roommate, Yi Chen. I think it is very difficult to have a wonderful friend like you especially abroad. Thank you for making the apartment feels like home. I will deeply cherish the memory and our friendship.

CONTRIBUTORS AND FUNDING SOURCES

Contributors

This work was supervised by a dissertation committee consisting of Dr. Je-Chin Han as the chair, Dr. Sai Chuen Lau and Dr. Gerald L. Morrison of the Department of Mechanical Engineering, and Dr. Hamn-Ching Chen of the Department of Civil Engineering as members. In addition, Dr. Kuang-An Chang of the Department of Civil Engineering served as the substitution of Dr. Hamn-Ching Chen during the oral defense (final examination) of this dissertation.

The experiment data taking in Session 3 was assisted by Andrew F Chen. The data taking in Session 4 was assisted by Nafiz Chowdhury. The data taking in Session 5 was assisted by Nian Wang and Izzet Sahin.

All other work for this dissertation was completed by the student, under the advisement of Dr. Je-Chin Han of the Department of Mechanical Engineering.

Funding Sources

Graduate study was supported by the Graduate Research Assistantship from Dr. Je-Chin Han. In addition, the study was also supported by Ralph E. James Fellowship from Turbomachinery Laboratory at Texas A&M University and Emil Buehler Aerodynamic Analog Fellowship from Emil Buehler Foundation.

NOMENCLATURE

Symbols

A	Area [m^2]
AOI	Area of interest
C	Vane chord length [m]; concentration by volume
CCD	Charge-coupled device
DR	Coolant-to-mainstream density ratio $= \rho_c/\rho_m$
d	Cooling hole diameter [m]
I	Intensity
L	True suction side surface length [m]; cooling hole length [m]
LE	Leading edge of vane; three rows of leading edge cooling holes
LED	Light-emitting device
M	Blowing ratio $= \rho_c v_c/\rho_m v_m$
Ma	Mach number
MFR	Coolant-to-mainstream mass flow ratio $= \dot{m}_c/\dot{m}_m$
n	Number of the cooling hole in a given row
P	Pressure [Pa]
Pr	Prandtl number
r	Recovery factor $= Pr^{1/3}$
s	Hole-to-hole spacing of cooling holes [m]
Sc	Schmidt number

SS1	1st row of suction side cooling holes
SS2	2nd row of suction side cooling holes
TE	Trailing edge
TTL	Transistor-transistor logic
Tu	Turbulence intensity [%]
v	Velocity [m/s]
W	Molecular weight [kg]
X	Distance from the leading edge of hardware [m]

Greek Symbols

α	Surface injection angle [^{o}]
γ	Specific heat ratio
η	Film cooling effectiveness
ρ	Fluid density [kg/m^3]

Subscripts

air	Property with air injection
aw	Adiabatic wall
ax	Axial
b	Black condition
c	Coolant
fg	Property with foreign gas injection
is	Isentropic
m	Mainstream

ref	Reference condition
s	Static (for pressure and temperature)
t	Total (for pressure)
w	Wall; impermeable wall

TABLE OF CONTENTS

Page

ABSTRACT ii

DEDICATION iv

ACKNOWLEDGEMENTS v

CONTRIBUTORS AND FUNDING SOURCES vi

NOMENCLATURE vii

TABLE OF CONTENTS x

LIST OF FIGURES xiii

LIST OF TABLES xvii

1. INTRODUCTION 1

2. OBJECTIVE 3

3. FILM COOLING EFFECTIVENESS COMPARISON ON FULL-SCALE TURBINE VANE ENDWALLS 4

- 3.1 Literature Review 4
  - 3.1.1 Geometry Effect 4
  - 3.1.2 Coolant-to-Mainstream Condition Effect 5
  - 3.1.3 Endwall Flow Field and Heat Transfer 6
- 3.2 Experimental Setup and Method 11
  - 3.2.1 Three-Vane Annular Sector Cascade 11
  - 3.2.2 Film Cooling System 15
  - 3.2.3 Experimental Method – Pressure-Sensitive Paint 20
- 3.3 Test Matrix 26
- 3.4 Experimental Uncertainty 27
- 3.5 Results and Discussion 27
  - 3.5.1 Image Transformation 27
  - 3.5.2 Design1 28
  - 3.5.3 Design2 37
  - 3.5.4 Design Comparison 43

4. TRANSONIC TURBINE VANE SUCTION SIDE FILM COOLING WITH SHOWERHEAD EFFECT....48

4.1 Literature Review....48
4.1.1 Mainstream Condition Effect....48
4.1.2 Film Cooling on Vane/Blade Surface....50
4.2 Experimental Setup and Method....52
4.2.1 Five-Vane Annular Sector Cascade....52
4.2.2 Film Cooling System....54
4.2.3 Experimental Method – Pressure-Sensitive Paint....57
4.3 Test Matrix....60
4.4 Experimental Uncertainty....62
4.5 Results and Discussion....63
4.5.1 Static Pressure Measurement on the Vane Suction Side....63
4.5.2 Adiabatic Film Cooling Effectiveness....66
4.5.3 Effect of Blowing Ratio....69
4.5.4 Effect of Density Ratio....71
4.5.5 Effect of Exit Mach Number....73
4.5.6 Engine-like Condition....75

5. TURBINE VANE ENDWALL FILM COOLING COMPARISON FROM DIFFERENT FILM-HOLE PATTERNS AND UPSTREAM LEAKAGE INJECTION ANGLES....84

5.1 Literature Review....84
5.1.1 Endwall Film Cooling with Upstream Leakage....84
5.1.2 Effect of Injection Angle....87
5.2 Experimental Setup and Method....88
5.2.1 Four-Passage Linear Cascade....88
5.2.2 Film Cooling System....90
5.2.3 Experimental Method – Pressure-Sensitive Paint....94
5.3 Test Matrix....94
5.4 Experimental Uncertainty....95
5.5 Results and Discussion....96
5.5.1 Upstream Injection Angle Effect....96
5.5.2 Design Comparison....108

6. CONCLUSIONS....112

6.1 Film Cooling Effectiveness Comparison on Full-Scale Turbine Vane Endwalls....112
6.2 Transonic Turbine Vane Suction Side Film Cooling with Showerhead Effect....113
6.3 Turbine Vane Endwall Film Cooling Comparison from Different Film-Hole Patterns and Upstream Leakage Injection Angles....114

REFERENCES.....116

LIST OF FIGURES

Page

Figure 1. Flow loop for the full-scale endwall test section and facility. 12

Figure 2. Schematic of the annular sector cascade. 12

Figure 3. Schematic of the test facility. (a) Upstream view; (b) Downstream view. 13

Figure 4. Turbulence grid. 14

Figure 5. Flow deflector caps. (a) For inner plenum; (b) For outer plenum. 16

Figure 6. Perforated plates. (a) For inner plenum; (b) For outer plenum. 16

Figure 7. Planar projected cooling hole distribution on the AOI of vane test section. (a) Design1; (b) Design2. 18

Figure 8. Test section in the camera-point-of-view. (a) Design1, downstream view; (b) Design1, upstream view; (c) Design2, downstream view; (d) Design2, upstream view. 19

Figure 9. PSP system/working principle. 21

Figure 10. PSP calibration setup. 22

Figure 11. PSP calibration results. (a) For room temperature as reference temperature; (b) For operating temperature as reference temperature; (c) For different camera view angles. 23

Figure 12. Test section painted with PSP. (a) Design1, downstream view; (b) Design1, upstream view; (c) Design2, downstream view; (d) Design2, upstream view. 24

Figure 13. Isentropic Mach number distribution: (a) downstream view and (b) upstream view. 29

Figure 14. Cross-flow visualization (DR = 1.5, MFR = 4%): (a) downstream view and (b) upstream view. 31

Figure 15. Film cooling effectiveness distributions of design1 at DR = 1.0. 34

Figure 16. Film cooling effectiveness distributions of design1 at DR = 1.5. 35

Figure 17. Laterally (spanwise) averaged film cooling effectiveness of design1. 36

Figure 18. Film cooling effectiveness distributions of design2 at DR = 1.0.....41

Figure 19. Film cooling effectiveness distributions of design2 at DR = 1.5.....42

Figure 20. Laterally (spanwise) averaged film cooling effectiveness of design2.....43

Figure 21. Area averaged film cooling effectiveness of design1 and design2.....47

Figure 22. Flow loop for the test section and facility.....53

Figure 23. Schematic view of the vane cascade and instrumentation setup. (a) Cascade assembly; (b) Cascade and DAQ facility setup. 54

Figure 24. Test vane. (a) Film cooling hole locations and plenum; (b) Section view of coolant supply passages (the red dashed line is the top view of DAQ area). ...56

Figure 25. Test section with true data capturing angle and the schematic of coolant loop. 57

Figure 26. PSP calibration results under different reference temperature. 59

Figure 27. Exit Mach number history for the current test section.....60

Figure 28. Vane surface. (a) Static pressure distribution; (b) Isentropic Mach number distribution.....65

Figure 29. Load distribution at mid-span of vane's suction side. (a) Static pressure; (b) Isentropic Mach number.....66

Figure 30. Laterally averaged effectiveness for a selective case. (a) Time-dependent effectiveness; (b) Deviation percentage due to effectiveness fluctuation. 67

Figure 31. Film cooling effectiveness distribution on AOI for exit Ma = 0.7. (a) DR = 1.0; (b) DR = 2.0.....77

Figure 32. Film cooling effectiveness distribution on AOI for exit Ma = 1.1. (a) DR = 1.0; (b) DR = 2.0.....78

Figure 33. Film cooling effectiveness distribution on AOI for DR = 1.0. (a) M = 0.7; (b) M = 1.6.....79

Figure 34. Film cooling effectiveness distribution on AOI for DR = 2.0. (a) M = 0.7; (b) M = 1.6.....80

Figure 35. Laterally (spanwise) averaged effectiveness for M effect comparison. 81

Figure 36. Laterally (spanwise) averaged effectiveness for DR effect comparison. 82

Figure 37. Laterally (spanwise) averaged effectiveness for exit Ma effect comparison..83

Figure 38. Flow loop for the test section and facility.....89

Figure 39. Schematic view of the vane cascade assembly. 90

Figure 40. Schematic of the endwall test section. 92

Figure 41. Schematic of different injection angle for two-row upstream leakage. 92

Figure 42. Schematic of film-hole patterns on endwall. 93

Figure 43. Exit Mach history for the current test section. 95

Figure 44. Film cooling effectiveness of axial row configuration under different upstream leakage injection angle. 99

Figure 45. Laterally (spanwise) averaged film cooling effectiveness of axial row configuration under different upstream leakage angle. 99

Figure 46. Film cooling effectiveness of cross row configuration under different upstream leakage injection angle.....101

Figure 47. Laterally (spanwise) averaged film cooling effectiveness of cross row configuration under different upstream leakage injection angle.....101

Figure 48. Film cooling effectiveness of cluster configuration under different upstream leakage injection angle.....103

Figure 49. Laterally (spanwise) averaged film cooling effectiveness of cluster configuration under different upstream leakage injection angle.....103

Figure 50. Film cooling effectiveness of mid-chord row configuration under different upstream leakage injection angle.....105

Figure 51. Laterally (spanwise) averaged film cooling effectiveness of mid-chord row configuration under different upstream leakage injection angle.....105

Figure 52. Film cooling effectiveness of downstream row configuration under different upstream leakage injection angle.....107

Figure 53. Laterally (spanwise) averaged film cooling effectiveness of downstream row configuration under different upstream leakage injection angle.....107

Figure 54. Laterally (spanwise) averaged film cooling effectiveness when upstream leakage injection angle is 30^{o}.....110

Figure 55. Laterally (spanwise) averaged film cooling effectiveness when upstream leakage injection angle is 40^{o}.....110

Figure 56. Laterally (spanwise) averaged film cooling effectiveness when upstream leakage injection angle is 50^{o}.....111

Figure 57. Area-averaged film cooling effectiveness for all the design combinations..111

LIST OF TABLES

Page

Table 1. Summary of the test matrix for the full-scale vane endwall film cooling study.....26

Table 2. Summary of the test matrix of the transonic vane suction surface film cooling study.....62

Table 3. Summary of the test matrix for the vane endwall film cooling study with upstream leakage.....95

1. INTRODUCTION

Gas turbine has been proven to be the most important part in the prosperous of industries including aviation and power generation applications. Thermodynamic analysis of Brayton cycle, which describes all gas turbine concept, indicates that higher turbine inlet temperature (T_4) is beneficial to the thermal efficiency for engine running under both simple and combined cycle. It initiates the studies about proper ways to accommodate the turbine component under elevated heat load since a better engine performance when the higher firing temperature is achieved. However, in the modern gas turbine engine, the elevated turbine inlet temperature has already exceeded the melting point of the material for turbine hardware. In addition, the material yield strength drops dramatically under high temperature. It is the implementation of the cooling technology that makes the current turbine hardware survives. Without such protection, numerous forms of mechanical failure associated with the extreme temperature condition like creep, thermal fatigue, oxidation, incipient melting as indicated by Brooks [1] will happen on turbine hardware. For the perspective to further reach better engine performance as projected to bring the turbine inlet temperature above 1700 ^{o}C, it is crucial to have better cooling schemes applied on the turbine hardware to protect them from thermal failures mentioned above. The improved cooling approach implemented can ensure temperature distribution is not beyond operation limits of the materials used as well as a satisfactory engine lifespan from early breakdown [2].

Among the existing cooling technologies applied on gas turbine, film cooling is an effective approach to have the low-temperature secondary flow ejecting through the discrete holes on the turbine hardware and forming a barrier layer on the surface to reduce the heat load to the hardware [3]. Film cooling has already been implemented on the first stage turbine vanes and endwalls, as they are located right at the exit of the combustion chamber, particularly face the most intensive heat load among all the turbine parts. Especially for turbine endwall, it is a critical portion to cool due its complicated three-dimensional flow field and considerably exposed area in modern design [4]; in addition, the trend of low NOx engine emission also suggests that the temperature profile from the combustor needs to be more uniform (flat) that directly increases the heat load on the endwall compared to before. Currently, multi rows of cooling holes are often dispersed on the vanes' surface and endwall to attempt a full coolant coverage [4]. Nonetheless, the film cooling performance on vane surface and endwall highly depend on geometry. Besides, the introduction of coolant for film cooling directly deteriorates the engine efficiency due to the decrease of the mainstream's mass flow rate that goes through the combustor to produce work. It is an endless goal for gas turbine designers to have higher engine thermal efficiency by effectively handle the heat load on the first stage vane and endwall regions under the premise that only limited amount of compressor bleed air is utilized. And this goal is mainly feasible through more in-depth studies of film cooling on various areas of interests in gas turbine hardware.

2. OBJECTIVE

Knowing the importance of better understanding of film cooling, however, most of the experiment in gas turbine researches were conducted in linear cascade, which has been a favorable choice for most of the researchers in gas turbine field. In fact, the radial pressure gradient does not establish in the linear cascade. Luque and Povey [5] indicated that the secondary flow from linear cascade is different from the characteristic that exists in the real engine. The measurement of the surface heat transfer rate in the linear cascade is not representative if without proper correction, which ought to be highly influenced by the secondary flow structure. Another drawback for linear cascade is that the three-dimensional airfoil and endwall design which is prevalent in modern real engines cannot be implemented before geometrically simplified to a two-dimensional profile. Annular sector cascade is a balanced approach between fully annular cascade and simplified linear cascade. Three-dimensional real engine hardware can be adapted to the test section which is expected to create a more authentic flow field for the experiment. The manufacturing cost is also considerably lower than the fully annular cascade. In terms of these edges comparing to simplified linear cascade and costly fully annular cascade, the advantage of the annular sector cascade has not been utilized by researchers yet. Therefore, the objective of the studies in this proposal is to conduct more thorough measurement and analysis of film cooling on gas turbine vane and endwall regions under various conditions in annular sector cascade.

3. FILM COOLING EFFECTIVENESS COMPARISON ON FULL-SCALE TURBINE VANE ENDWALLS

3.1 Literature Review

Film cooling effectiveness/performance highly relies upon cooling hole itself like orientation, geometry, and arrangement. It also depends on the mainstream flow characteristics such as Reynolds number, Mach number, and turbulence intensity. Further, the thermal and flow interaction between the coolant and mainstream including the pressure ratio of coolant plenum to the mainstream, the temperature ratio of coolant to mainstream both play critical roles. While the introduction of similitude matches the thermal and flow characteristics of laboratory condition to engine's design point, it is unpractical to achieve the high-pressure and high-temperature environment like the real engine in the academic setting. Researchers hence proposed the coolant-to-mainstream blowing ratio or mass flow ratio to simulate the pressure ratio, the coolant-to-mainstream density ratio to simulate the temperature ratio. These two parameters allow the researchers to systematically track the film cooling performance of a particular design in the laboratory setting.

3.1.1 Geometry Effect

Cooling hole orientation has a substantial influence on the film cooling effectiveness. Ligrani et al. [6] indicated that coolant ejected at an angle to the mainstream results in greater film cooling effectiveness due to better lateral diffusion of coolant.

Schmidt et al. [7] validated that compound-angle holes provide better lateral coolant distribution, especially at high momentum flux ratios. Berhe and Patankar [8] demonstrated the effect of curvature on film cooling effectiveness of discrete holes. They reported higher effectiveness on the convex surface than the flat plate at low blowing ratio and reverse at high blowing ratio. The concave surface showed an opposite trend. For the hole geometry, cylindrical holes and fan-shaped holes are found to be feasible in terms of machining and are extensively adopted in the modern gas turbine engine. The film cooling effectiveness of cylindrical hole is found to be increased with the increasing of blowing ratio until an optimal value (around M = 0.5 to 0.65). The higher blowing ratio results in jet lift-off and less coolant coverage on the surface (effectiveness decreases). On the other hand, with the expanded exit area which reduced the coolant jet momentum, the shaped hole has a lower tendency to lift-off and hence exhibit a better coolant coverage and higher film cooling effectiveness [7, 9, 10]. That is to say, under a given amount of coolant supplied, the cooling hole geometry can deliver a substantially different scenario of the coolant coverage from the reduction of coolant momentum [11,12].

3.1.2 Coolant-to-Mainstream Condition Effect

The coolant-to-mainstream temperature ratio varies from 0.5 to 0.85 which the corresponding density ratio varies from 2.0 to 1.5 in a typical gas turbine engine. While the realization on these density ratios in the experiment can be simulated by heat transfer technique through the utilization of cryogenic coolant as reported by Pietrzyk et al. [13] and Sinha et al. [14]. Another approach is the adoption of heat and mass transfer analogy,

established on the assumption that Lewis number is around 1. This unity of Lewis number indicates strong turbulent mixing in the flow field which matches the flow characteristic of the hot mainstream from the exit of combustion chamber entering the turbine. In this manner, the effect of density ratio can be examined with mass transfer technique by using foreign gasses of larger molecular weight as coolant [15]. This method has been prevalently embraced to systematically study the density ratio effect on the film cooling effectiveness on a simplified geometry like flat plate [16-18] as fundamental studies. While the studies on the flat plate film cooling [13,14,16-19] suggest that increasing the density ratio leads to higher effectiveness, the conclusion from flat plate may not exactly project to the situation in other turbine parts like endwall/platform due to the presence of horseshoe vortex, passage vortex, and the nonuniform pressure gradient existed inside endwall passage [20,21].

3.1.3 Endwall Flow Field and Heat Transfer

In terms of flow and thermal characteristics, the endwall region is the most challenging task for gas turbine researchers and engineers, due to complicated three-dimensional flow field and a large fraction of the surface to be cooled. Blair [22], Langston [23], Graziani et al. [24], Goldstein and Spores [25], Chyu [26] presented thorough investigations on the flow field of the endwall region and the corresponding influence on the heat transfer. They pointed out that the secondary flow from the pressure gradient in the vane passage, which makes the small horseshoe vortex from the flow stagnation on the vane further developed into larger passage vortex. The passage vortex migrates from

the leading edge of one vane's pressure side toward the suction side of the neighbor vane. Those vortices result in three-dimensional cross flow on the pressure side and the suction side of the vane. They concluded the secondary flow greatly affects the heat transfer in the endwall and suction side of the vane.

Regarding the film-cooling studies on the endwall portion, Takeishi et al. [27] studied the film cooling effectiveness on the endwall of a fully annular low aspect ratio nozzle guide vane. They concluded that the horseshoe vortex decreases the film cooling effectiveness near the leading edge on the endwall. And the film cooling distribution on the endwall is dependent on the passage vortex, cross flow, and nozzle wake. Harasgama and Burton [28] performed heat transfer experiment on outer endwall of nozzle guide vane with discrete holes film cooling under engine conditions through similarity. They indicated that the secondary flow in the passage convects the coolant toward the suction side and results in a high heat load region on the trailing edge of pressure side. Jabbari et al. [29] concluded that discrete location measurement up to 60 gas concentration sampling taps in the turbine endwall covered by cooling holes is still insufficient to determine the film cooling effectiveness distribution in this region due to its strong local variations. They further used ammonium-diazo paper to visualize the qualitative information of coolant trace under different blowing ratios and density ratios. Friedrichs et al. [30] studied film cooling effectiveness of turbine endwall using ammonia diazo. They found that coolant ejection modifies the endwall flow field, which makes the liftoff lines move to downstream as delay three-dimensional separation of inlet boundary layer. Thus, the separation line for the horseshoe vortex moves closer to leading edge and the separation

line from pressure leg of horseshoe vortex crosses to the suction side and moves further downstream. Meanwhile, the strong cross-flow inside the passage turns toward mainstream streamline due to film injection, makes the coolant trajectories different from the cooling hole exit angle except for the location very close to the hole exit. Friedrichs et al. [31] further investigated the aerodynamic characteristic of endwall film cooling and claimed the necessity of considering the three-dimensional endwall flow nature for proper endwall film cooling design configuration. They concluded that when the coolant stagnation pressure is higher than mainstream stagnation pressure, the ejected coolant can re-energize the boundary layer to reduce the passage vortex and the subsequent flow mixing. Simon and Piggush [32] documented a comprehensive review regarding endwall aerodynamics and heat transfer. Generally speaking, they pointed out that it is difficult to have an optimal arrangement of cooling holes/slots on endwall since the performance of aerodynamic for the endwall region is sensitive to the passage geometry, pressure distribution, and the corresponding secondary flow structure including horseshoe vortex, passage vortex, and corner vortex. On the other hand, endwall heat transfer is driven by complicated interdependence between endwall and vane geometries, mainstream and coolant flow characteristic including cooling hole/flow locations and injection angles. It is also challenging to isolate those individual effects as well as to predict the cumulative effect.

Kwak et al. [33] performed the heat transfer and pressure distribution under different turbulence intensities on turbine vane endwall in a five-vane linear cascade. The pressure data demonstrates as a complementary information to the identification of local

hot spot on the endwall. Barigozzi et al. [34] studied endwall film cooling through fan-shaped hole with different area ratio. They found that the thermodynamics loss coefficient of the hole exit on the endwall surface is practically the same level as smooth endwall. They concluded that the wider hole exit area allows better lateral spreading of coolant but increases the turbulent mixing near the hole exit which the jet decays in downstream direction faster. Colban et al. [10] studied the film cooling on a vane endwall with different hole geometries at low and high freestream turbulence levels. They concluded that the fan-shaped holes increase area averaged effectiveness by an average 75% over cylindrical counterparts. The fan-shaped hole is also relatively insensitive to the level of turbulence. On the other hand, high turbulence level counteracts the coolant liftoff for cylindrical hole configuration and reduce the sensitivity of effectiveness to the coolant flow rate. Mahmood et al. [35] conducted experiments on flow and temperature field near a three-dimensional asymmetric contour endwall in a linear cascade with and without film cooling. They indicated vortex flow axis changes as the flow yaw angle and pitch-wise velocity changes when the film cooling is presented. When higher blowing ratio, the coolant flow strengthens the boundary layer when injected under the boundary layer so the vortices get pushed even higher above the endwall. Andrei et al. [36] performed adiabatic film cooling effectiveness measurement on an annular sector cascade of heavy duty gas turbine vane by PSP method. Due to their wind tunnel design, film cooling coverage was visualized from the upstream view only, but the capability of measuring film cooling effectiveness on annular sector cascade is validated preliminarily.

In addition to the turbine endwall itself, researchers tried to see if inherent features from the engine hardware near endwall can actually play a vital role to alter the local pressure/flow field and be beneficial for local film coverage once the coolant is introduced. The slashface or mateface, which is the interface between two turbine hardware are brought to researchers' attention. Cardwell et al. [37] studied the effect of the misalignment between the mid-passage gap and endwall on endwall film cooling. Their results indicate that the slot ejection from mid-passage gap can almost take care the cooling of the suction side passage. However, a later study from Cardwell et al. [38] claimed that the mid-passage gap leakage flow (0-0.3%) proved to have little effect on endwall adiabatic effectiveness level. Endwall flow measurements from Piggush and Simon [39] came up with an interesting argument that with the slashface presents, the pressure leg of horseshoe vortex toward the suction side may be reduced by either ingestion into the gap (upstream) or by being lifted off the endwall by the ejected flow from the gap (downstream). They concluded that the main effect is due to the addition of low-streamwise-velocity flow issuing from the gap and the thicker endwall boundary layer it creates, especially in the downstream portion of the passage where the passage velocity is high and the locally injected mass flux is also high. Significant losses are thus created due to the injected leakage flow, especially at higher blowing rate. Roy et al. [40] studied heat transfer performance of a transonic turbine blade passage including mateface gap and endwall contouring. Their findings agree with Cardwell et al. [38] that with mateface flow presents, the leakage from mateface provides coolant coverage near the suction side aft portion but cannot extend all the way up to the whole suction side due to mixing between

mainstream and mateface jet and the inherent pressure gradient that drives the secondary flow. They also mentioned that the relative spreading of the coolant is highly dependent on the location of the mateface gap with respect to the passage and also on the airfoil design. Recently, vane endwall studies from Shiau et al. [41] on full-scale annular sector cascade with realistic slashface seal and Chowdhury et al. [42] on scaled-up linear cascade with simulated slashface both proved that the coolant injection from slashface gap can form a wedge-shaped coolant coverage to protect the vane passage near suction side. On the other hand, a blade endwall (platform) study from Chen et al. [43] demonstrated a different shape of coolant coverage from slashface coolant injection due to the dissimilar pressure gradient inside the blade passage from vane. Providing that the existing coolant coverage contributed by slashface injection, these studies open the possibility of endwall cooling hole rearrangements under a fixed amount of coolant consumption.

3.2 Experimental Setup and Method

3.2.1 Three-Vane Annular Sector Cascade

The measurements were conducted in a three-vane annular sector cascade, which the whole flow loop is shown in Figure 1. Three full-scale vanes (green parts shown in Figure 2), which joined followed the real assembly condition (orientation and gap clearance) are adopted as test section to simulate the radial pressure gradient and reflect the three-dimensional secondary flow effect in the engine. The test facility is shown in Figure 3. The wind tunnel inlet cross-section shape is designed as an annular sector of the combustor transition duct in order to match the geometry of real vanes test section, so is

the outlet. The mainstream air is supplied by a 450 horsepower, 3-stage centrifugal compressor that is capable of delivering a volume flow rate up to 6.14 m^3/s at its design point. The volume flow rate is regulated by a frequency controller with an operational range from 0 to 60 Hz.

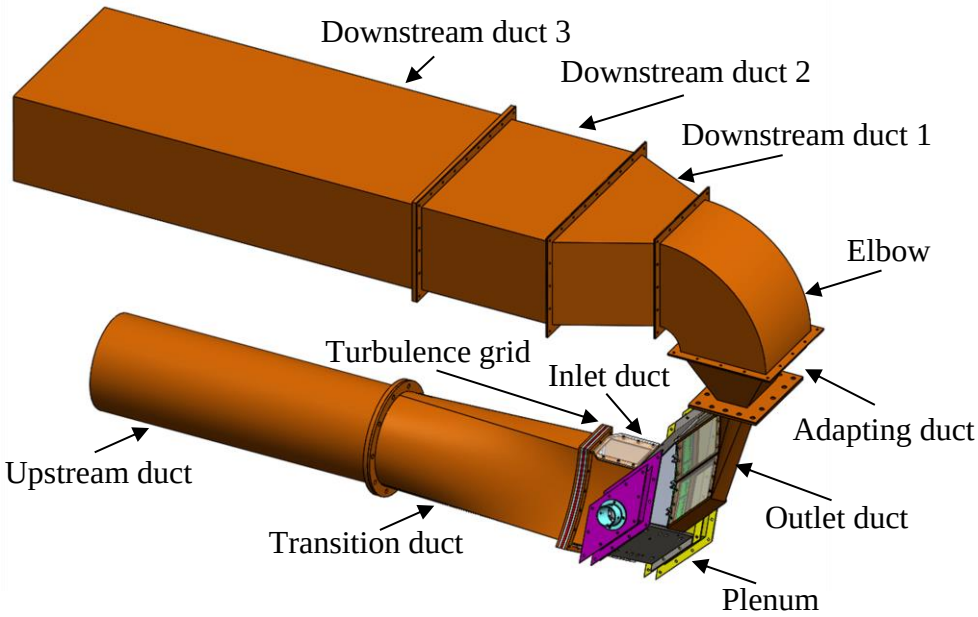

Figure 1. Flow loop for the full-scale endwall test section and facility.

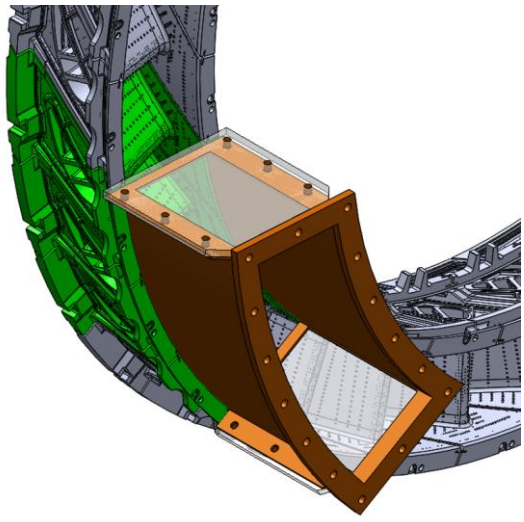

Figure 2. Schematic of the annular sector cascade.

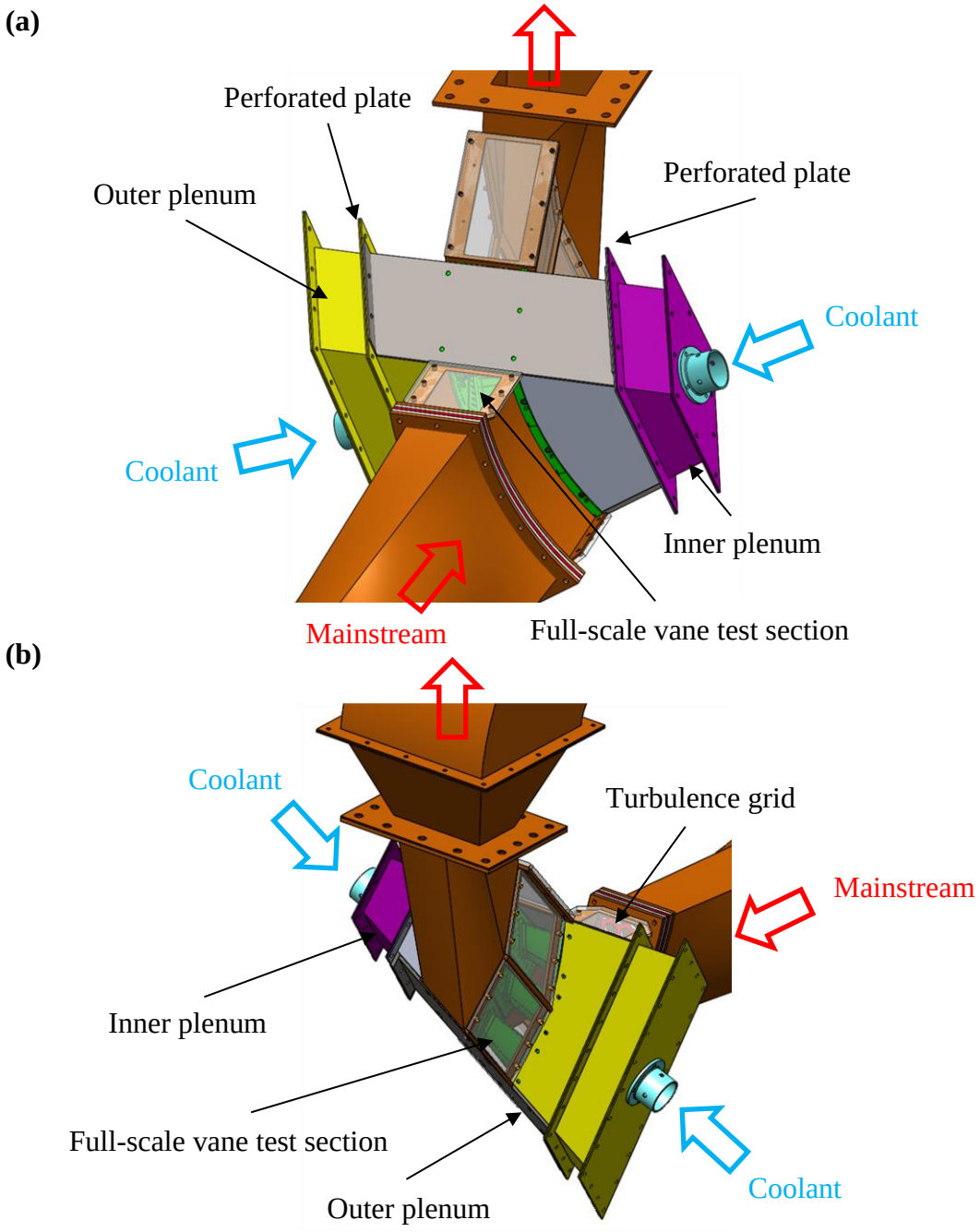

Figure 3. Schematic of the test facility. (a) Upstream view; (b) Downstream view.

The cascade inlet and exit velocities are set to be 32.35 m/s and 83.62 m/s corresponding to the inlet and exit Mach numbers of 0.092 and 0.237, respectively. The

mainstream Reynolds number is calculated to be 350,000 according to inlet velocity and vane chord length (C = 17.5 cm). The overall pressure ratio ($P_t/P_{s,exit}$) is about 1.05. To simulate the turbulence intensity from combustor exit entering the turbine vane, a turbulence grid design that based on the correlation of grid-generated turbulence decay [44] was implemented. The designed turbulence grid is shown in Figure 4, with the same cross-section as inlet, is a staggered circular mesh with the hole diameter 4.445 cm, hole-to-hole distance 5.715 cm (equivalent bar width 1.27 cm), 55% porosity and placed 30.48 cm upstream of the hardware to create a freestream turbulence intensity (Tu) about 12% with integral length scale around 1.5 cm. The top and bottom walls of the inlet duct and the side walls of outlet duct are geared with 1.27 cm thickness transparent Plexiglas (as shown in Figure 3) to ensure a wide optical access to the test section from both upstream and downstream.

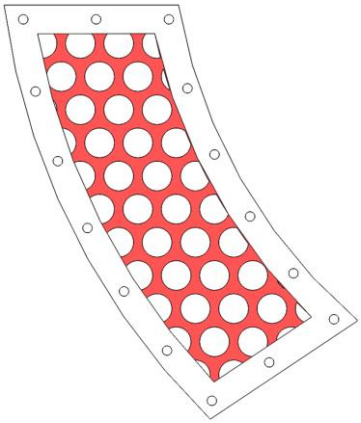

Figure 4. Turbulence grid.

Inlet and exit velocity were monitored by Pitot-static probe as both the total and static pressure of the cascade were recorded during the experiment. They were stationed at 5.08 cm upstream and 2.54 cm downstream of the center vane hardware, respectively.

The mainstream temperature was monitored by a T-type thermocouple equipped with the inlet Pitot-static probe. A LED excitation light and a monochrome CCD camera were used for measuring PSP emission intensity for film cooling effectiveness calculation and arranged in upstream and downstream, respectively. The camera and light source were adjusted (angle, distance) to a clear view with good visual extension reciprocally (upstream-to-downstream, downstream-to-upstream) subjected to the spatial constraint.

3.2.2 Film Cooling System

The film cooling system consisted of coolant source, flow meter, and plenums. The coolant source is either gas cylinders (N_2, CO_2) or air compressor (dry air). Coolant flow rate is adjusted and monitored by an orifice flow meter. Two separate annular sector plenums on the hub and the tip portion of the test section were designed accordingly: one to supply inner endwalls, the other to supply both vanes and outer endwalls. Single coolant inlet of 10.16 cm diameter in each plenum was used. By using the flow deflector caps of different pattern (as shown in Figure 5) on the coolant inlet as well as having the perforated plates (as shown in Figure 6, 5% and 10% open area for inner and outer plenum, respectively), the pressure inside plenums were found to be uniform from the measurement of pressure taps at each side of the plenum.

(a) **(b)**

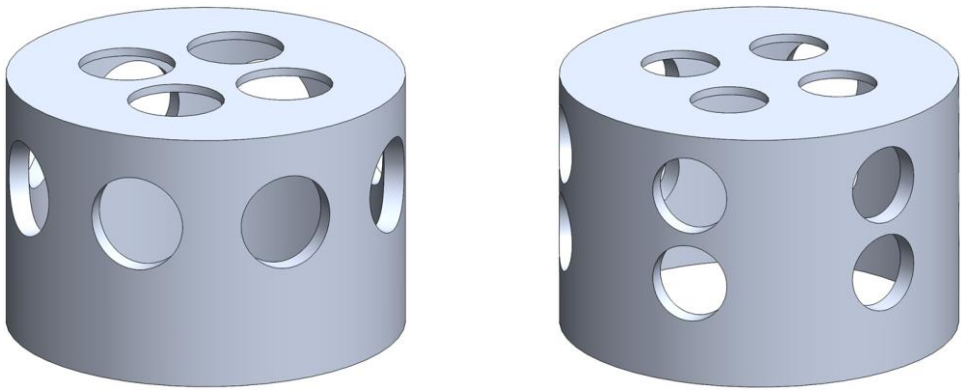

Figure 5. Flow deflector caps. (a) For inner plenum; (b) For outer plenum.

Unit: cm

(a) **(b)**

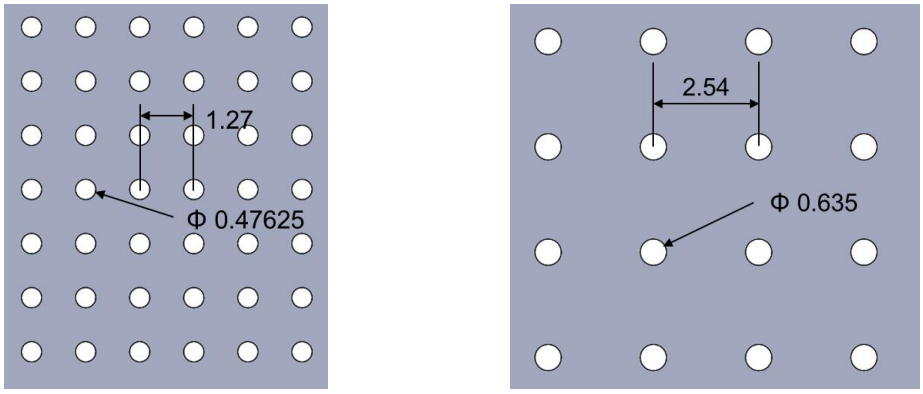

Figure 6. Perforated plates. (a) For inner plenum; (b) For outer plenum.

The impingement plates were installed on the endwalls of test section inside both plenums to support the necessary internal cooling. The coolant will travel inside the plenum, flow through the impingement plate and then eject through the discrete film cooling holes to protect the surface. Two kinds of endwall cooling designs will be studied. For design1, there are 95 typical layback fan-shaped holes dispersed within the majority of the vane passage, 14 angled cylindrical holes are dispersed within the beginning of the

passage. Also, there are 16 and 16 angled cylindrical holes along both sides of the slashface gap, respectively. In addition, 31 angled cylindrical holes are uniformly dispersed inside the whole slashface gap. For design2, there are 51 typical layback fan-shaped holes dispersed within first 40% of the vane passage, 14 angled cylindrical holes dispersed within the beginning of the passage. Also, there are 9 and 5 angled cylindrical holes along both sides of the slashface gap, respectively. There are 5 big angled cylindrical holes dispersed within the middle to the aft portion of the passage. In addition, there are 14 angled cylindrical holes dispersed inside the first half of the slashface gap. In short, the discrete film cooling hole pattern in the upstream passage of design1 is identical to design2 up to 40% of the normalized axial distance. For the rest of the passage (mid to downstream), 44 fan-shaped holes and 13 angled cylindrical holes in design1 are substituted for 5 big angled cylindrical holes adopted in design2. This makes the total cooling hole inlet area for design1 8.1% higher than design2.

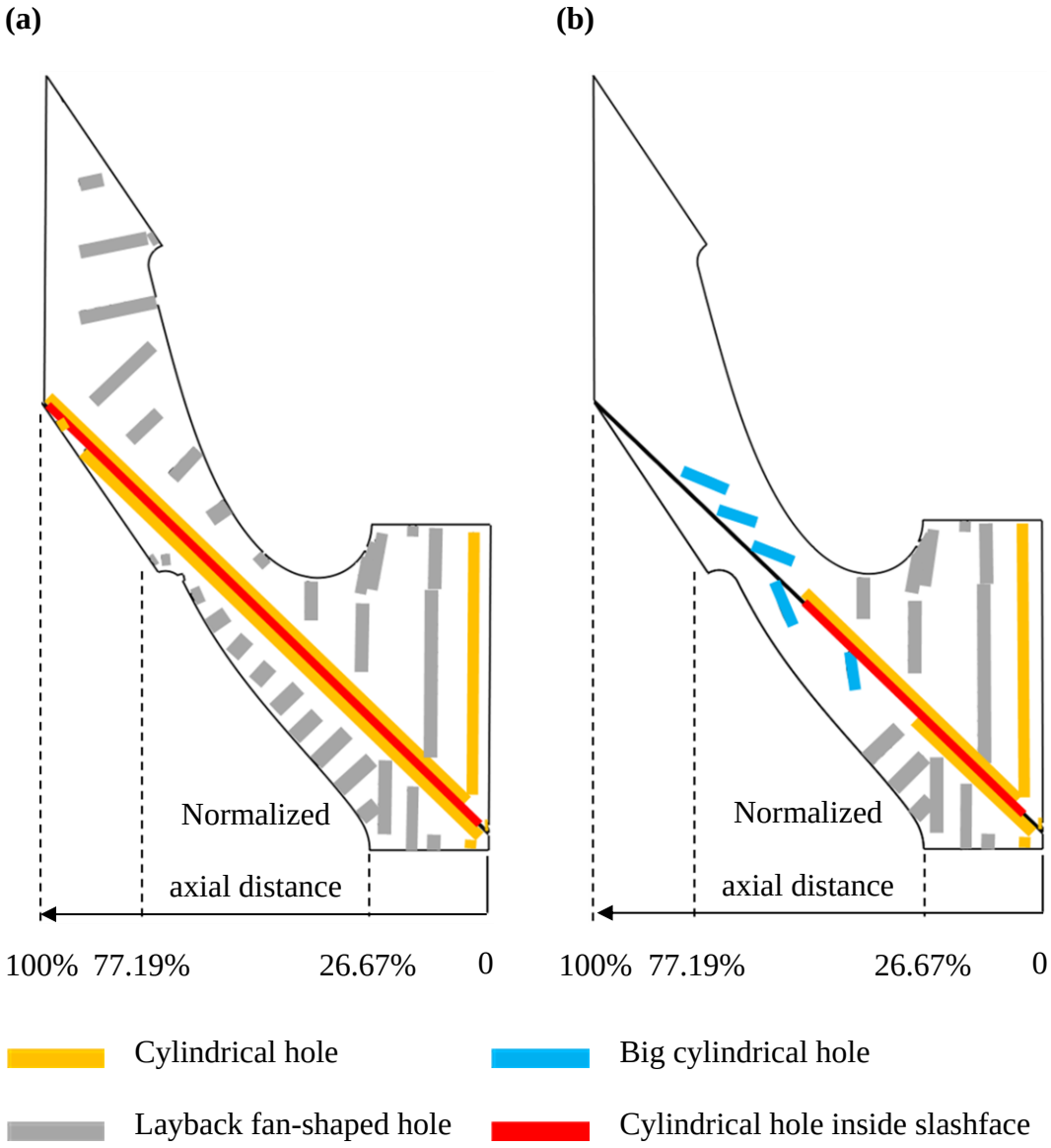

Figure 7. Planar projected cooling hole distribution on the AOI of vane test section. (a) Design1; (b) Design2.

Figure 7 shows the planar projection of the cooling hole arrangement on the area of interest (AOI). Different kinds of the cooling hole are shown in different color in Figure 7. While most color lines in Figure 7 represent rows of cooling holes, each light blue line represents a single big hole. It should also be addressed that the vane boundaries in AOI are not the true vane profile but the fillet edge of the vane on the endwall. Figure 8 shows the test section in the camera-point-of-view during the experiment from downstream and upstream, respectively. Red lines enclosed region in Figure 8 indicate the same AOI of Figure 7 from different views. Color lines in both Figure 7 and Figure 8 represent the cooling hole rows locations in the vane inner endwall as well as the vane surface.

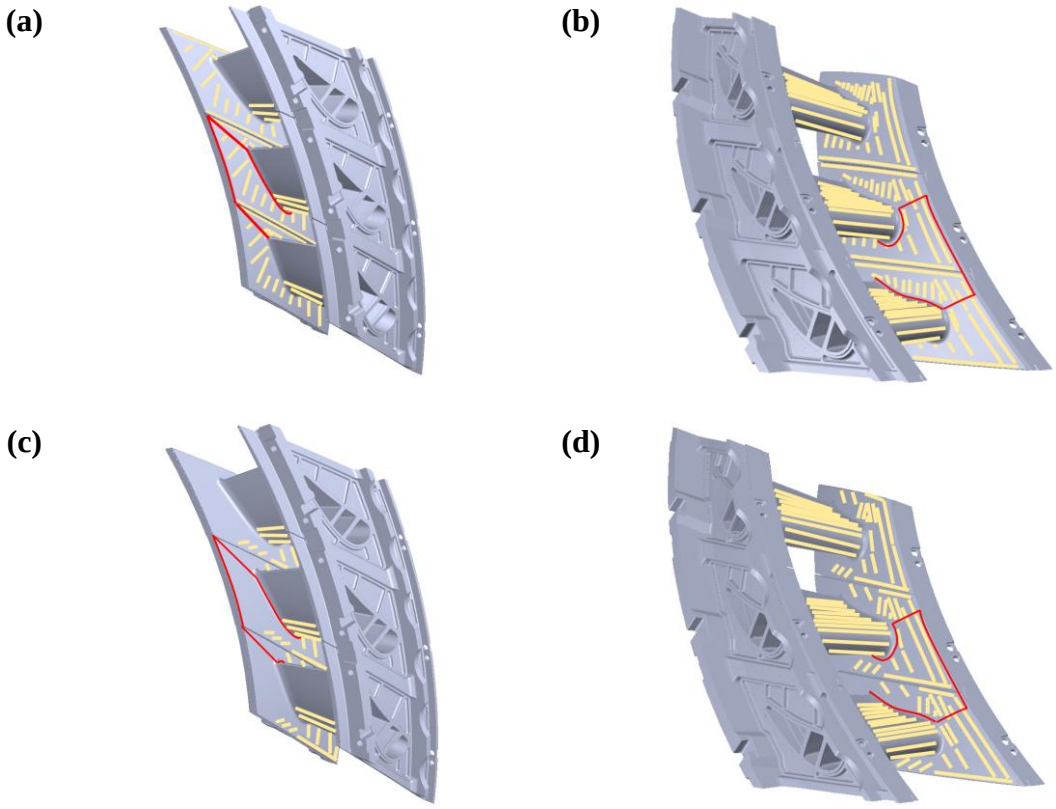

Figure 8. Test section in the camera-point-of-view. (a) Design1, downstream view; (b) Design1, upstream view; (c) Design2, downstream view; (d) Design2, upstream view.

3.2.3 Experimental Method – Pressure-Sensitive Paint

Film cooling effectiveness distributions were achieved by using Pressure-sensitive paint (PSP) on the target surface that based on mass transfer method under the assumption that heat and mass transfer analogy holds. As a reliable and relatively economical method with the advantages of non-intrusive and high spatial resolution measurement on various geometry, it is popular in aerodynamic testing for capturing full pressure field. PSP (Innovative Scientific Solutions Inc., UF-750) is comprised of luminescent molecules and an oxygen-permeable polymer binder dissolved in a solvent. With the presence of oxygen molecules, the luminescent molecules will interact and transmit energy to oxygen molecules in their path to the ground state. This radiationless deactivation results in smaller emission intensity is called oxygen quenching, serving as the working mechanism. For the UniFIB PSP used in this study, the excitation wavelength is ranging from 380 nm to 520 nm, a 400 nm LED-based light source (Innovative Scientific Solutions Inc., LM2X-DM-400) was therefore used to excite the luminescent molecules in the polymer binder. Since the wavelength of PSP emission intensity is ranging from 620 nm to 750 nm, to prevent the capturing of excitation light instead of emission light, the emission intensity of painted surface is recorded through a long-pass filter (600 nm) using monochrome scientific grade CCD camera (Innovative Scientific Solutions Inc., PSP-CCD-M, with 1608 x 1208 resolution, 35 fps, 14-bit dynamic range). A typical PSP system is shown in Figure 9.

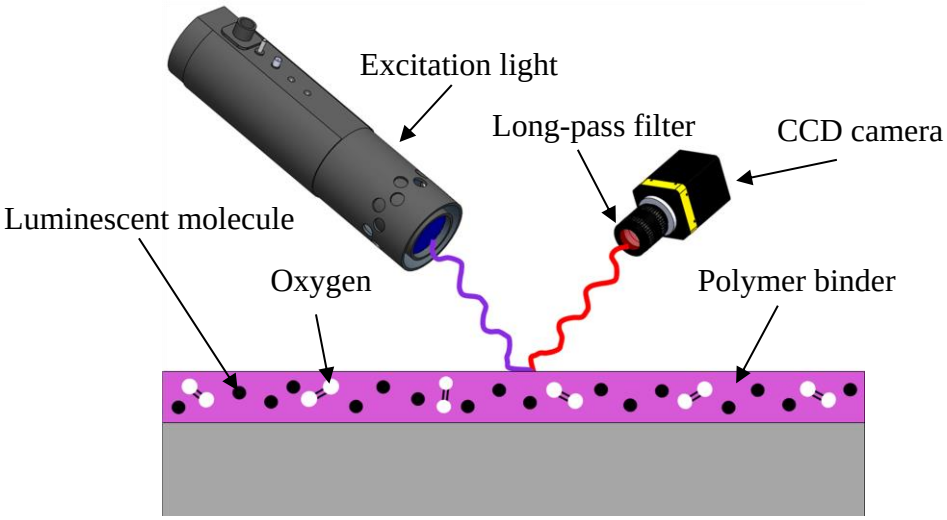

Figure 9. PSP system/working principle.

To correlate the variation of PSP emission intensity to the oxygen partial pressure (since the concentration of oxygen in the ambient air is constant, this is equivalent to the partial pressure of air) on the painted surface, a pressure-controlled chamber with a transparent Plexiglas top wall was used. A small strip of copper was sprayed with black paint to reduce stray reflection from the surface, and then painted with 4-5 layers (30-40 μm thickness per layer) of PSP. It is served as the calibration coupon. One T-type thermocouple was embedded in the coupon and a flexible heater mat was attached to the other side of the coupon. The coupon was placed inside the chamber. The relative positions of LED and CCD camera to the calibration coupon were adjusted to a similar view angle and distance to the test surface close to the same configuration of the real test. The CCD camera was set to capture 100 grayscale images at each target pressure to eliminate the measurement noise. The calibration setup is shown in Figure 10. The emission intensity of PSP under known pressure was recorded as I. The reference intensity I_{ref} was the

measured intensity under the reference pressure P_{ref} (ambient pressure) condition. The intensity acquired with the excitation light source off is the background noise of camera called I_b. The emission intensity was then measured covering the expected experiment pressure range. In these particular calibrations, the intensity was recorded at a 2-inHg interval from -26 inHg (gauge pressure) to 0 inHg (gauge pressure, which is identical to 1 atm) and then at a 2-psi interval from 2 psig to 8 psig. The oxygen partial pressure adjacent to the painted surface can thus be correlated with the surface emission intensity by a power fitting curve as shown in Figure 11(a).

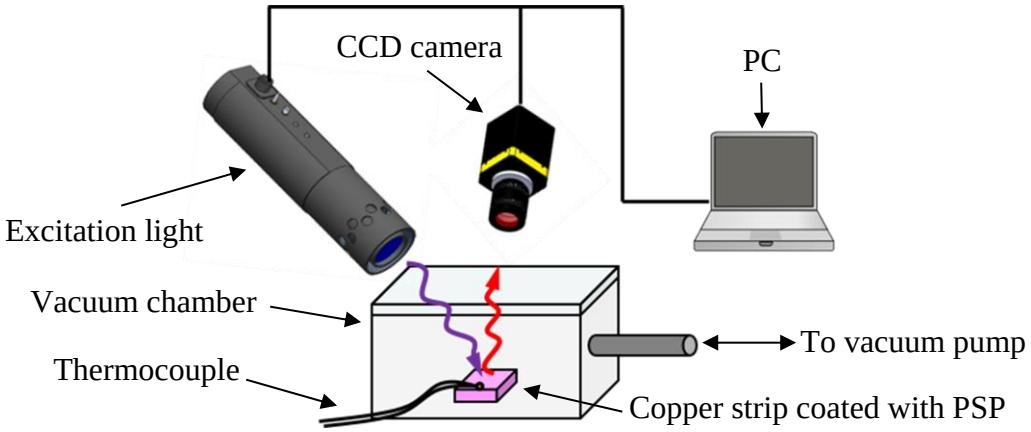

Figure 10. PSP calibration setup.

However, the emission intensity depends on oxygen partial pressure as well as the temperature of the surface. To properly address this uncertainty, the complete calibration processes were performed with test strip heated to different temperatures. As shown in Figure 11(a), the emission intensity decreases as the surface temperature increases if the reference condition is set at room temperature (unheated). It is found that if the reference condition is set at corresponding heated surface temperature, all the curves collapse into one (Figure 11(b)), promised the viability of deduced calibration curve in different surface

temperatures. Besides, Figure 11(c) is the calibration curve from different calibration strip for camera view angle effect study. It is found that the emission intensities are insensitive to the camera view angle from upright (90 degrees) to 20 degrees. This fact guarantees the accuracy of the emission intensity measurement when perspective distortion exists due to view angle disparity and it further eliminates the data uncertainty when different camera angle was used during the experiment.

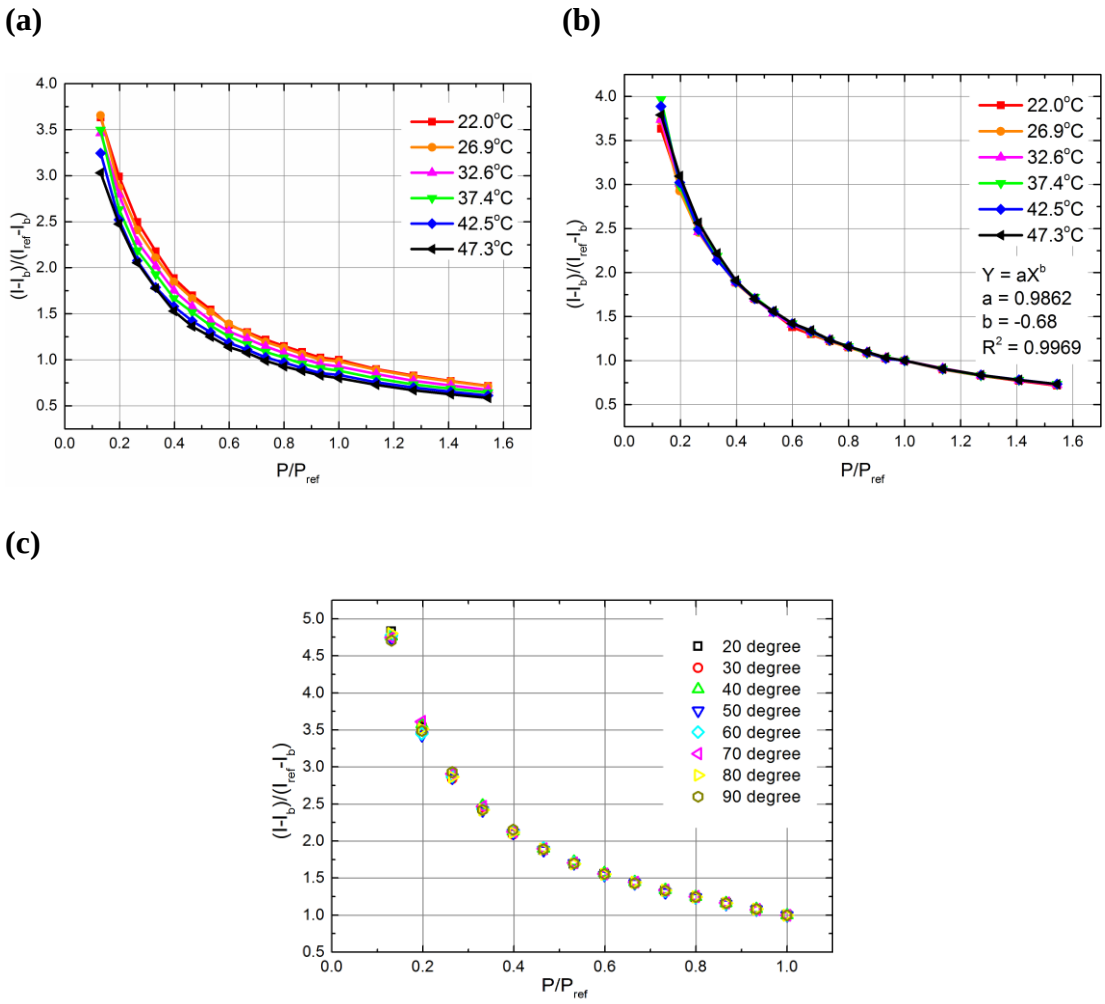

Figure 11. PSP calibration results. (a) For room temperature as reference temperature; (b) For operating temperature as reference temperature; (c) For different camera view angles.

The inner endwalls from two vane hardware were first sprayed with black paint to reduce the surface stray reflection and then painted with 4-5 layers of PSP by using an airbrush. Due to cooling hole dimension, to avoid the cooling hole from clogging, special care was carried out to plug all the holes during the painting process. The PSP coated hardware is shown in Figure 12, the pink and orange color lines in Figure 12 portray the cooling hole array locations in the same fashion as Figure 7 and Figure 8.

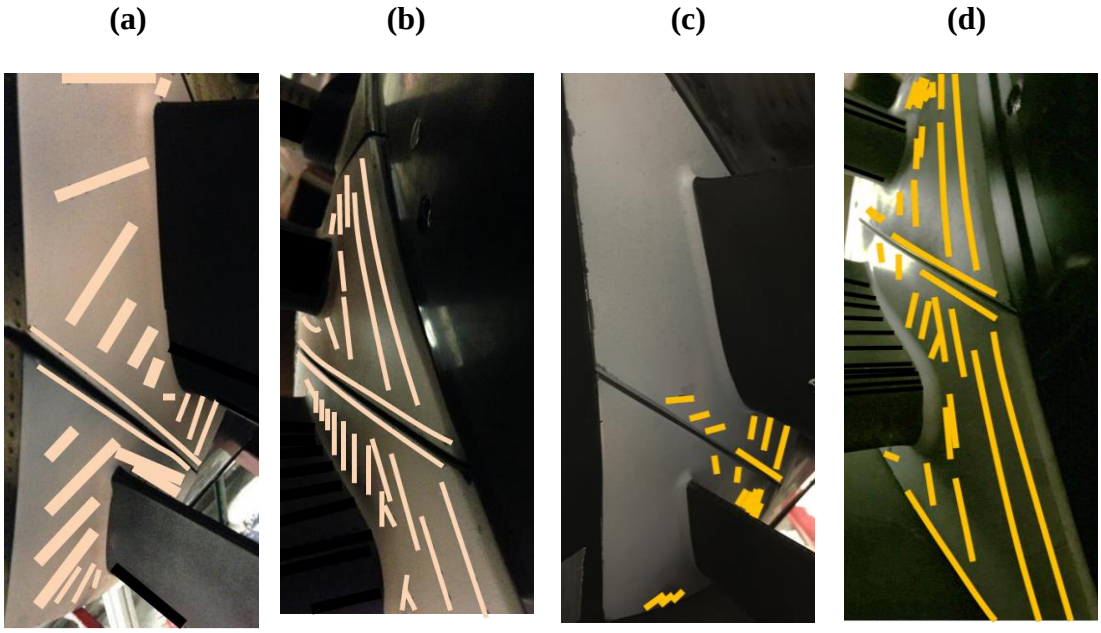

Figure 12. Test section painted with PSP. (a) Design1, downstream view; (b) Design1, upstream view; (c) Design2, downstream view; (d) Design2, upstream view.

Having the calibration curves, four image sets are needed to determine the film cooling effectiveness for each tested flow condition: the black image, the reference image, the foreign gas injection image, and the air injection image. Similar to the calibration, the black image (I_b) is to correct the background noise of camera sensor from dark current. The reference image is the intensity taken with LED light source switched on called I_{ref}.

Both I_b and I_{ref} are conducted under the condition with neither mainstream nor coolant flow present. The foreign gas injection image (I_{fg}) is taken with the mainstream flow and LED illuminated, an oxygen-free foreign gas is adopted and injected as the coolant in lieu of the PSP characteristic and to achieve high density ratio (e.g. CO_2, DR = 1.52 ≈ 1.5) under room temperature condition. The corresponding oxygen partial pressure is $P_{O_2,fg}$. The air injection image is taken under the same condition as foreign gas, but the foreign gas is replaced by air as coolant. The corresponding oxygen partial pressure is $P_{O_2,air}$. There were 100 grayscale images recorded in each image set to average out the measurement noise.

Using the heat and mass transfer analogy, the adiabatic film cooling effectiveness when using oxygen-free gas as coolant can be expressed as,

$$\eta = \frac{T_w - T_m}{T_c - T_m} \approx \frac{C_w - C_m}{C_c - C_m} = \frac{C_{O_{2,fg}} - C_{O_{2,air}}}{C_{O_{2,c}} - C_{O_{2,air}}} = 1 - \frac{C_{O_{2,fg}}}{C_{O_{2,air}}} \quad (1)$$

It is noted that T_m is considered to be the freestream recovery temperature when the mainstream is compressible flow. When the concentration terms are replaced with oxygen partial pressure, Eq. (1) can be rearranged and becomes [45],

$$\eta = 1 - \frac{1}{\left[\left(\frac{P_{O_2,air}/P_{O_2,ref}}{P_{O_2,fg}/P_{O_2,ref}} - 1\right)\frac{W_{fg}}{W_{air}} + 1\right]} \quad (2)$$

By the merit of using PSP, the adiabatic effectiveness calculated from Eq. (2) is conduction-error free.

3.3 Test Matrix

Six sets of experiments were conducted to study effects of coolant-to-mainstream mass flow ratio (MFR) and density ratio (DR) on the film cooling effectiveness of inner endwalls of full-scale engine hardware under the fixed mainstream condition for both design1 and design2, respectively. Since the mainstream accelerates along the passage, the surface pressure of test section varies accordingly and so as the blowing ratio. A wide range of local blowing ratios from upstream to downstream along the passage can be expected. Summary of the test matrix is shown in Table 1.

Table 1. Summary of the test matrix for the full-scale vane endwall film cooling study.

Experiment no.	MFR (%)	DR
1	2	1.0
2	3	1.0
3	4	1.0
4	2	1.5
5	3	1.5
6	4	1.5

From the conventional definition, MFR was calculated based on the mass flow rate of mainstream and coolant supply per passage. In the present study, three mainstream passages and two out of three cooling system on the inner endwalls were actively

functioned. A 3/2 ratio was applied to account for this factor when calculating the required coolant mass flow rate.

3.4 Experimental Uncertainty

The uncertainty of the measurement in this experiment comes from the fluctuation of mainstream velocity (±1%), the fluctuation of coolant flow rate (±1.8%), and the thermocouple reading (±0.5℃). For the film cooling effectiveness calculation, the major uncertainty is the variation of PSP emission intensity value captured by the camera. Multiple reference and black images were first taken to quantify the intensity fluctuation. By the method proposed by Kline and McClintock [46] based on a 95% confidence level, the uncertainty of film cooling effectiveness deduced from the calibration curve at $\eta = 0.1$, 0.3, 0.5 and 0.7 are 13.8%, 4.1%, 2.4% and 1.8%, respectively in the present study.

3.5 Results and Discussion

3.5.1 Image Transformation

The nature of this vane hardware and wind tunnel design prevent a single data taking view angle from capturing the whole AOI. Therefore, both upstream and downstream views need to be recorded individually for each test condition. To have a better representation of AOI (passage from LE up to nozzle wake region after TE) on the inner endwall for easy data comparison, other than the static pressure distribution and crossflow visualization part, the upstream and downstream data in the same test condition are undergone a perspective transformation by using the in-house MATLAB code. The

converted data are then stitched together to form a single image for further data processing including the spanwise averaged and area averaged effectiveness.

3.5.2 Design1

3.5.2.1 Static Pressure Measurements on the Endwall

The full static pressure distribution on the endwalls was measured by PSP under the condition with mainstream only. Therefore, this information is considered also valid for design2. Two measurements were performed from both upstream and downstream views. The static pressure measurements were converted to isentropic Mach number as showed in Figure 13. The presented values are calculated by the inlet total pressure and the local static pressure along the endwalls. The black line in Figure 13(a)(b) are the location where different views are joined together.

Low Mach number (high static pressure) zone near the vane's LE can be located clearly. This is due to the flow stagnation near the vane's LE portion. Mach number contour from both upstream and downstream views depict two important information: 1. The Mach number is increasing from LE of endwall toward the TE, which interprets that the mainstream accelerates along the passage. So as the decreasing trend of static pressure along the passage. 2. The Mach number near vane's pressure side is lower than that near the suction side. This Mach number difference represents the pressure difference, which is the primary reason for the strong cross flow inside the passage which affects the film cooling coverage and effectiveness on the endwall.

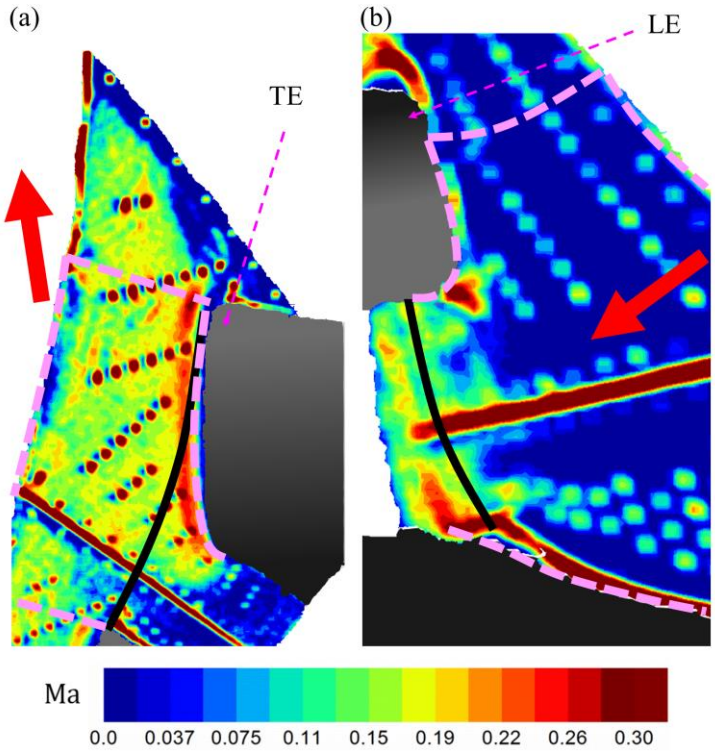

Figure 13. Isentropic Mach number distribution: (a) downstream view and (b) upstream view.

3.5.2.2 Adiabatic Film Cooling Effectiveness

The film cooling effectiveness distributions can precisely disclose the flow behavior which comes from the interaction between the coolant and mainstream flow. Moreover, it differentiates the whole endwall into the region that being cooled appropriately and the region that might susceptible to the high heat load.

First, the strong cross-flow effect is clearly visualized in Figure 14, which is the zoom in cropped view of one of the cases studied. It is distinctive that some of the coolant ejections demonstrate a huge difference to the hole exit direction (tiny black arrows in Figure 14). For example, the coolant deflection in Figure 14(b) is considered to be greatly

affected by the horseshoe vortex near the vane's LE. Detail film-cooling effectiveness of all cases examined are shown in Figure 15 and Figure 16. For the upstream region, a low effectiveness region can be located between the first row of cylindrical holes and the second row of shaped holes in front of the vane's LE. The hole orientation of the first row is nearly perpendicular to the mainstream flow direction, which attributes the resulting low coolant coverage. Starting from the second row, a good film cooling effectiveness spreads inside the passage along the vane curvature can be observed, representing strong coolant protection. However, the passage vortex that developed from the horseshoe vortex and the pressure gradient dominates the coolant distribution. A curve uncooled portion right near LE suction side of vane passage can be related to inlet boundary layer flow which is vigorously rolled up by horseshoe vortex to avoid the coolant remaining near endwall. The pressure gradient also prevents the coolant from staying near pressure side in the vane passage. This leads to an uncooled pressure side starting from the LE fillet to the TE. For the downstream region, the footprint of the strong passage vortex can be detected partly from the coolant coverage near the TE of suction side vane passage as well. In addition to that, mainstream deflects the coolant in a great manner as shown in all cases. It carries the coolant from lower endwall to the middle one, which turns out a better effectiveness. It also leaves the tail part of the endwall low film cooling effectiveness. After the TE of the vane passage, it is easily discernible that there is an unprotected region because of the nozzle wake flow. From Figure 15 and Figure 16, a peak effectiveness region that existed near the downstream section is evidently noticed. In consideration of 31 cooling holes dispersed inside the interface (slashface) gap between the vane hardware

(as shown in Figure 12(a)(b)), it is perceived to create intentional ejections from the slashface gap. Besides, these gaps can also serve the purpose to trap the film from lower endwall and then the film re-attaches on the gap downstream of middle endwall for better protection near the TE of vane suction side passage. The disparate cooling traces between the bottom of lower endwall and the target region can be an evidence for this argument. Unlike the complete passage in the target region, half passage existed in virtue of the flat duct wall enclosed the bottom of the lower endwall (refer to Figure 8(a)(b)). The cooling holes on the bottom of the lower endwall were blocked and no film was carried over from the neighbor vane endwall. This makes the film cooling configuration near the bottom of lower endwall inconsistent to the target region endwall.

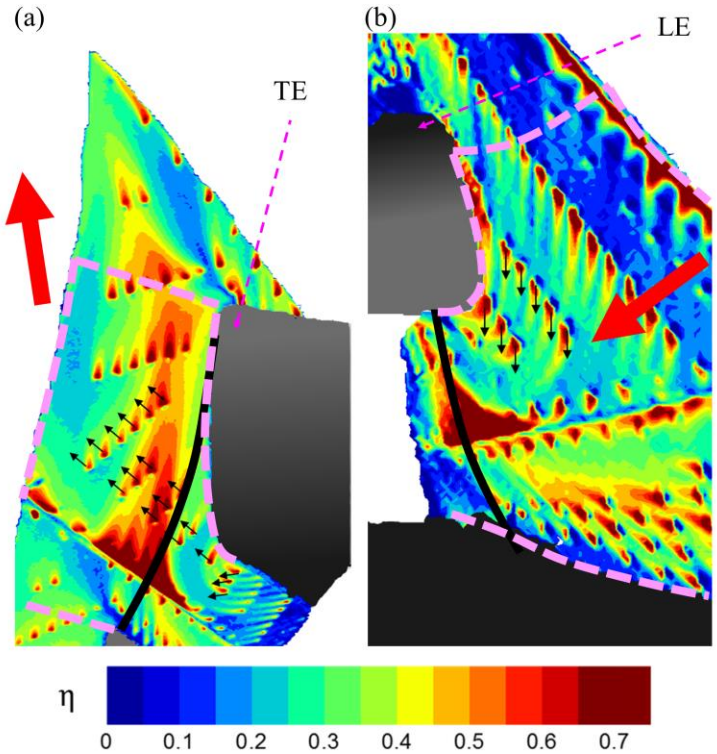

Figure 14. Cross-flow visualization (DR = 1.5, MFR = 4%): (a) downstream view and (b) upstream view.

3.5.2.3 Effect of Mass Flow Ratio

Figure 15 and Figure 16 show the film cooling effectiveness under different MFR for a given DR. For the cylindrical holes in the first row of the endwall passage, the coolant trace indicated its lift-off when higher MFR case was studied. This is consistent with the conclusion in the open literature that the cylindrical holes are ineffective design when coolant bears higher momentum. Due to the majority holes on the endwalls are shaped-holes, the expanded hole exit area vastly reduces the coolant jet momentum and hence no coolant lift-off is observed in most area in all the experiment cases. As the MFR increases, higher film cooling effectiveness is found near the hole exit and longer coolant trace can be recognized. While the longer trace improves the protection of all the originally cooled area in the vane passage, the benefit of higher MFR can be directly reflected on coolant protection of the fillet near the vane's LE. For MFR = 2%, scarce coolant distribution can be found near the fillet of vane's LE. When MFR = 4%, the coolant jets have relatively larger momentum to overcome the pressure to approach the fillet to a certain extent. The higher momentum of coolant in larger MFR also demonstrates a lower proclivity to the mainstream, extends the film cooling dissemination to a larger extent including the coverage to tail part of endwall.

3.5.2.4 Effect of Density Ratio

Film cooling effectiveness under different DR for a given MFR can be compared with the same index number of subfigures in Figure 15 and Figure 16. For a higher DR, it

is noticeable that a remarkable increase of film cooling effectiveness is achieved. As stated earlier, the DR is to simulate the temperature ratio of the coolant to mainstream in the real engine operation. Since under the same MFR, coolant with higher density actually possesses lower momentum, the injected heavier coolant has better tendency to stay attached to the surface from lift-off. Further, the higher density coolant exposes a better lateral coolant coverage, therefore, a preeminent care of the whole endwall passage including the effectiveness increase of nozzle wake flow region. Nonetheless, the comparison for different DR reveals that the film cooling effectiveness near the slashface gap in the middle endwall and near the TE of suction side vane passage is higher for the DR = 1.5 case. It is because if the denser coolant already interacted with mainstream or passage vortex, since retaining lower momentum, it is more easily to deflect by the mainstream along with the strong secondary flow.

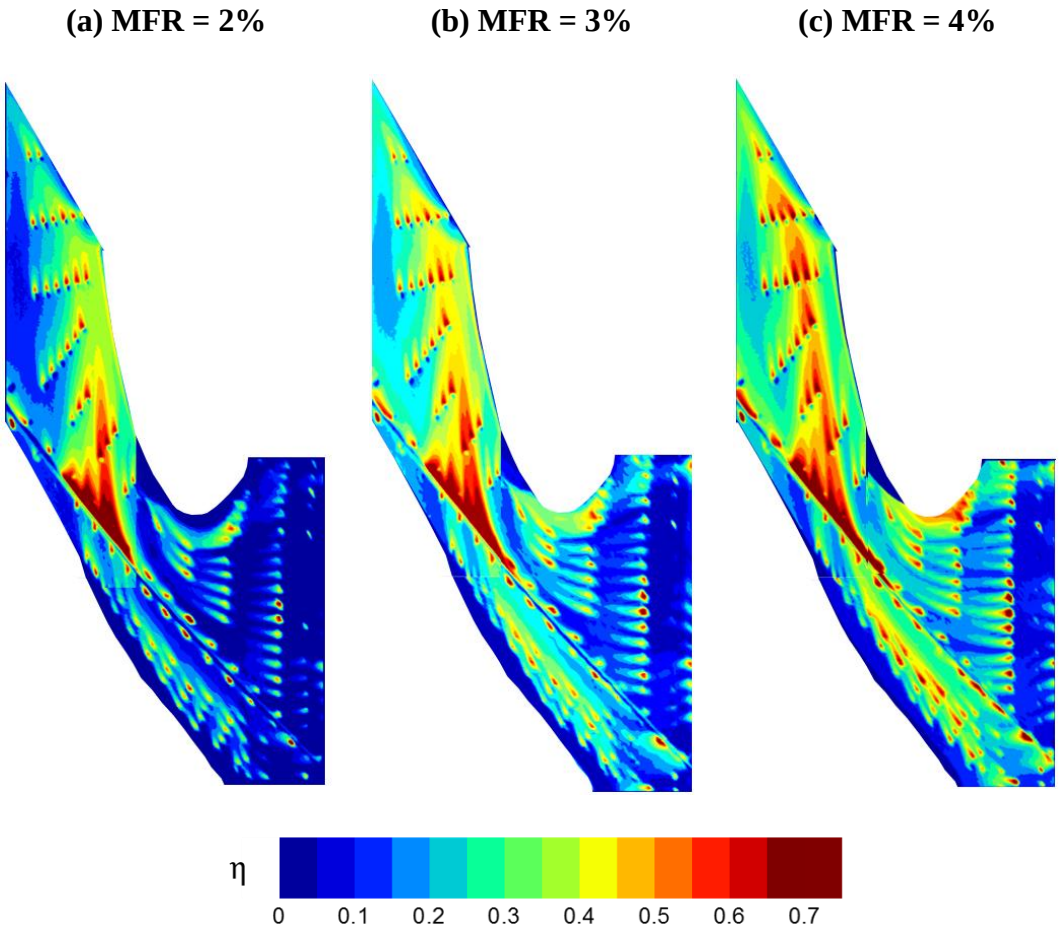

Figure 15. Film cooling effectiveness distributions of design1 at DR = 1.0.

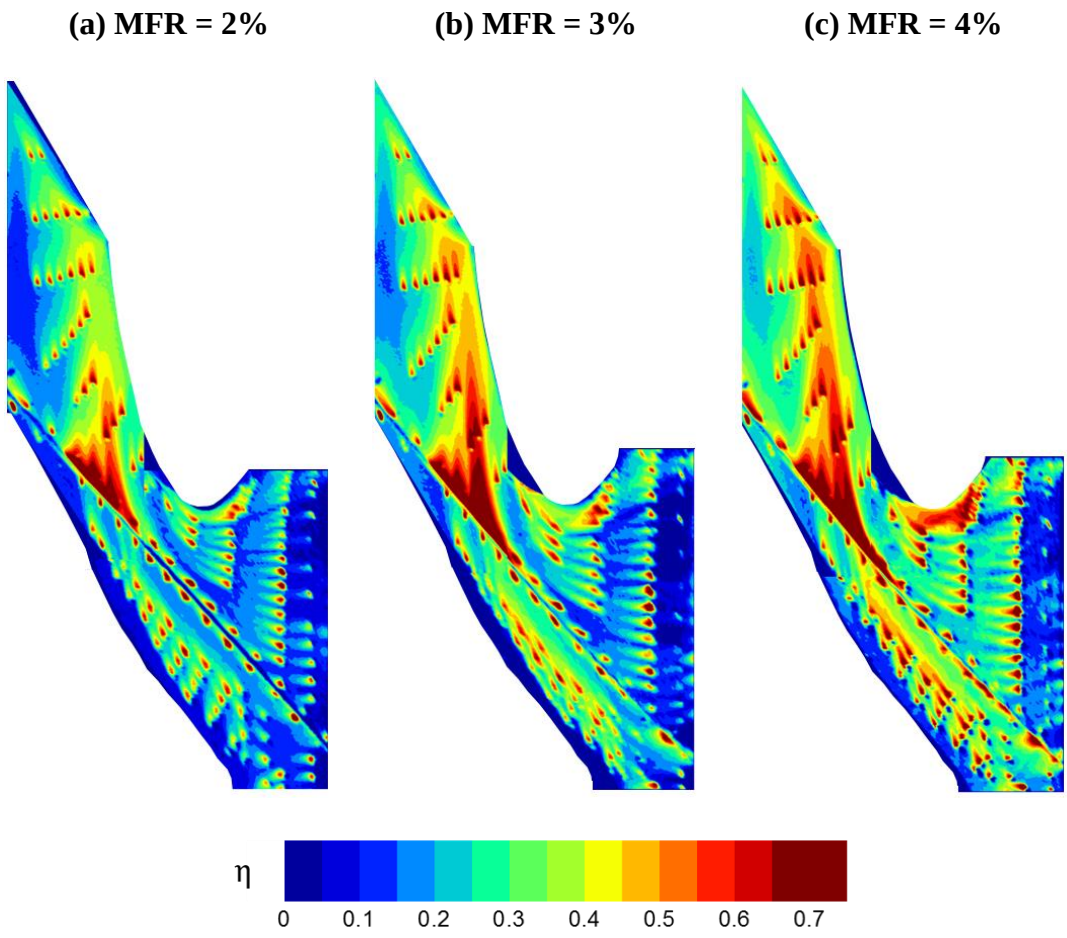

Figure 16. Film cooling effectiveness distributions of design1 at DR = 1.5.

3.5.2.5 Lateral Averaged Film Cooling Effectiveness

Due to the three-dimensional curvature of real hardware and the resulting limitation on view angle, the laterally (spanwise) averaged film cooling effectiveness calculation along the full endwall is not feasible through a single view. Thus, the presented result is the combination of two independent calculations of upstream and downstream contour plots, respectively to prevent from biased data because of visual limitation. From the data trend as shown in Figure 17, two high effectiveness locations can be specified.

The first big peak can be attributed to the dense cooling hole arrangement from holes in the second row of the passage, near LE of the middle vane, and the pressure side of the lower vane. Along the passage, the accumulation of coolant leads to the higher effectiveness toward the downstream. The highest peak is where the mix effect of amassing coolant from upstream and the intentional ejections from the slashface gap of vanes achieves the topmost effectiveness among all locations. To a further downstream, the unprotected tail part of vane and the nozzle wake flow region deeply reduce the calculated averaged effectiveness. More significantly, from the laterally averaged film cooling effectiveness along the endwall for different cases, the argument on the influence of MFR and DR to the effectiveness from the contour plots can be easily justified.

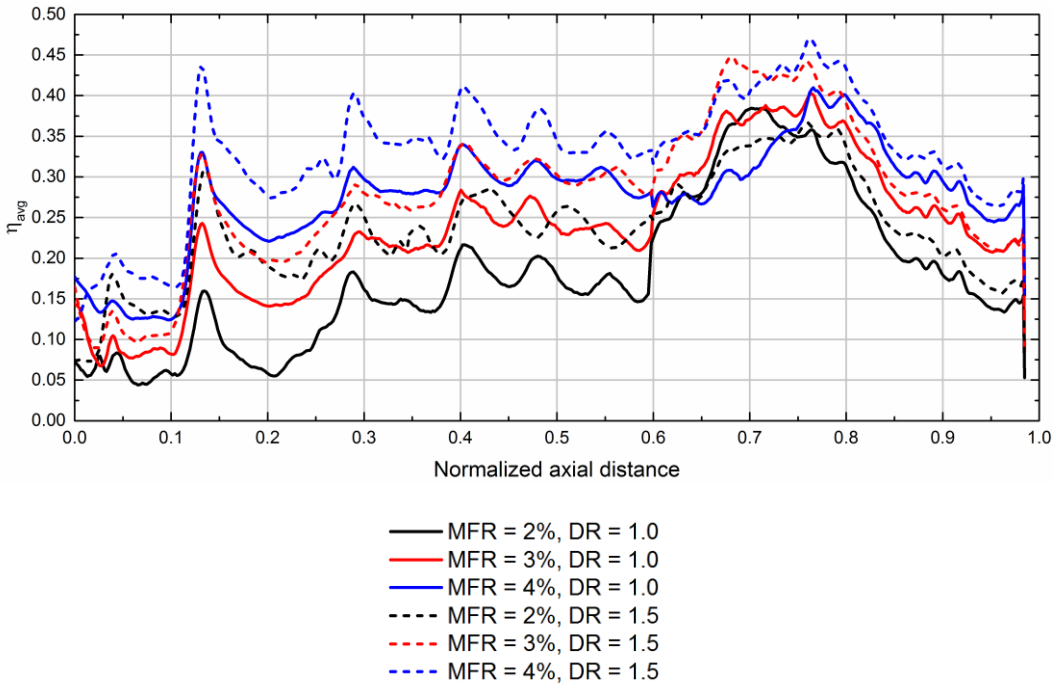

Figure 17. Laterally (spanwise) averaged film cooling effectiveness of design1.

3.5.3 Design2

3.5.3.1 Adiabatic Film Cooling Effectiveness

The detail film cooling effectiveness of all cases examined is shown in Figure 18 and Figure 19. Starting from the upstream portion, a low effectiveness region can be located between the first row of cylindrical holes and the second row of shaped holes in front of LE. The holes in the first row are of extreme injection angle (90^o) designed to let the mainstream completely deflects the ejection direction. However, very poor coolant contribution can be detected from this row especially the middle portion. The reason can be attributed to the steep injection angle design that these surface normal jets will mostly have intense mixing with mainstream and be diluted readily. Starting from the second row, considerable coolant traces are observed inside the passage along the vane curvature, indicating better coolant protection. The exposed fillet shape boundary near LE is a clear evidence of horseshoe vortex that prevents coolant to approach. The source of the passage crossflow, pressure gradient, prevents the coolant from staying near pressure side in the vane passage. This leads to an uncooled pressure side starting from near vane's LE fillet to the TE. The 5 big cylindrical holes are designed to take care of the cooling from mid-passage to TE and aft portion of the hardware. Those 2 big cylindrical holes near pressure side are supposed to take care the pressure side passage. However, it turns out mainstream deflects the coolant in a great extent as the trace is unable to protect the pressure side passage. From Figure 18 and Figure 19, a low effectiveness curve band close to the vane's suction side is identified as the lift-off line of passage vortex described by Friedrichs et al. [30]. Mid-passage near suction side and a considerable downstream portion are expected

to be protected by the coolant trace from 3 big cylindrical holes as their staggered configuration in this particular location could facilitate the coolant from upstream hole to contribute to the downstream and later accumulate to form a better downstream coverage. Visually, this arrangement seemed to be quite promising as most of the hardware aft portion is covered by long and wide coolant trace from 3 big cylindrical holes. From the vane's TE, it is noticeable that the current film-hole pattern is unable to take care of the wake region. It is worthwhile to mention that the slashface injection acts as a dominant factor in this particular endwall cooling hole design. As the cooling holes inside the slashface gap are located in the first half of the gap only, it is expected to control the ejection to occur mostly near upstream. A strong coolant injection is thus observed along the slashface starting from very upstream. Though affecting the cooling holes near pressure passage, the high effectiveness zone created by slashface in upstream is somewhat locally confined instead of propagating to downstream.

3.5.3.2 Effect of Mass Flow Ratio

Figure 18 and Figure 19 show the film cooling effectiveness under different MFR for a given DR. The suppression of horseshoe vortex when increasing MFR can also be observed near the LE of vane's pressure side as more coolant is approaching to the vane. Since the majority of the cooling holes except 5 big cylindrical ones are shaped holes, the coolant momentum is reduced as well as the tendency of coolant lift-off. As long as coolant does not detach from the surface, higher streamwise effectiveness is expected because more coolant is present with higher momentum when increasing MFR. While this

is generally true in this study, it is interesting to see that the effectiveness variation is quite different especially in upstream when increasing MFR if we separate the AOI into passage near pressure side and the one near suction side from slashface. For the pressure side passage, the trend is quite monotonic that the higher MFR directly leads to higher effectiveness near hole exit and longer coolant trace which reduces the unprotected area near vane's pressure side. The effusive coolant from upstream of slashface injection not only fills up the gap but also floods out toward the pressure side when MFR is high, similar to the scenario reported by Ranson et al. [47]. For the suction side passage, the effectiveness enhancement of increasing MFR is perceivable inside the passage as the longer trace gradually eliminates the unprotected portion like the region very close to the suction side. However, the upstream suction side passage actually shows a reduced coverage when MFR increases from 3% to 4%. The higher momentum of coolant in larger MFR moves the lift-off line of passage vortex to downstream as the low effectiveness curve band gradually detaches from the vane's suction side. High momentum coolant also demonstrates a lower tendency to be deflected from the mainstream. A clear example is when the MFR is 4%, which the coolant momentum from 3 big cylindrical holes in the mid to aft of the passage is so strong that is totally departed from the vane's suction side. In addition, this strong coolant momentum makes the lateral coolant spreading from 3 big cylindrical holes drops as the MFR increases, which indicates a typical cylindrical hole's behavior when increasing the coolant flow rate.

3.5.3.3 Effect of Density Ratio

Film cooling effectiveness under different DR for a given MFR can be compared with the same index number of subfigures in Figure 18 and Figure 19. For the region using shaped holes, wider traces compared to lower DR cases are observed as the heavier coolant increases the lateral spreading and stay attached to the surface better due to the lower momentum in high DR cases. Thus, for a given MFR, the effectiveness of high DR demonstrates the enhancement throughout most of the AOI except for MFR = 2%. The effusive coolant from upstream of the slashface are enhanced and seemed to be covering more area near pressure side passage, which directly boosted the performance of neighbor cooling holes. Since Piggush and Simon [39] mentioned that the low-streamwise-velocity flow issuing from the slashface makes a thicker endwall boundary. This boundary layer could be even thicker for higher DR case under the same MFR. Increased turbulence within the thicker boundary layer may bring the jets closer to endwall as the situation described by Anderson et al. [48]. For 3 big cylindrical holes, the reduced coolant momentum in higher DR have a better lateral coverage but also directly lead to the higher dependency of coolant trace on the mainstream compared to the lower DR cases. This results in wider film protection near the suction side passage but at the same time, slightly worse protection for the downstream part of hardware can be seen provided that a fixed amount of coolant is distributed toward suction side instead of the whole hardware.

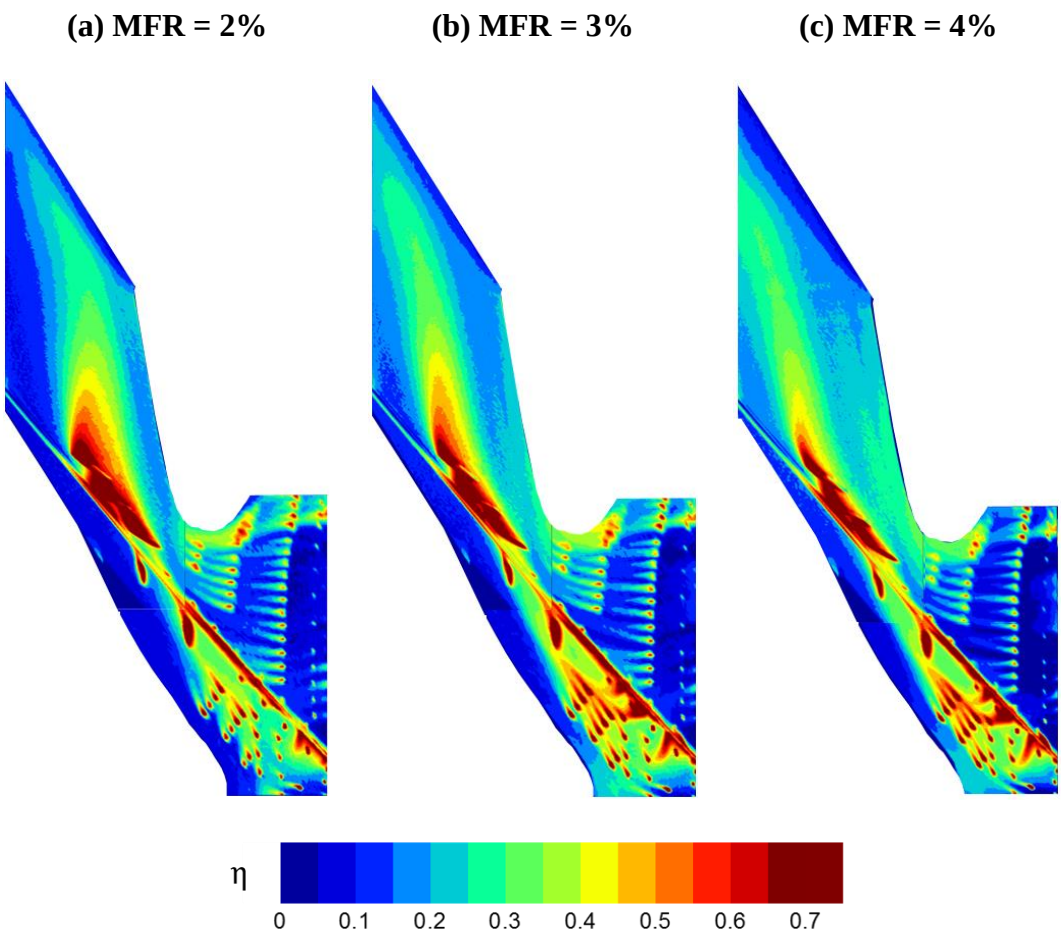

Figure 18. Film cooling effectiveness distributions of design2 at DR = 1.0.

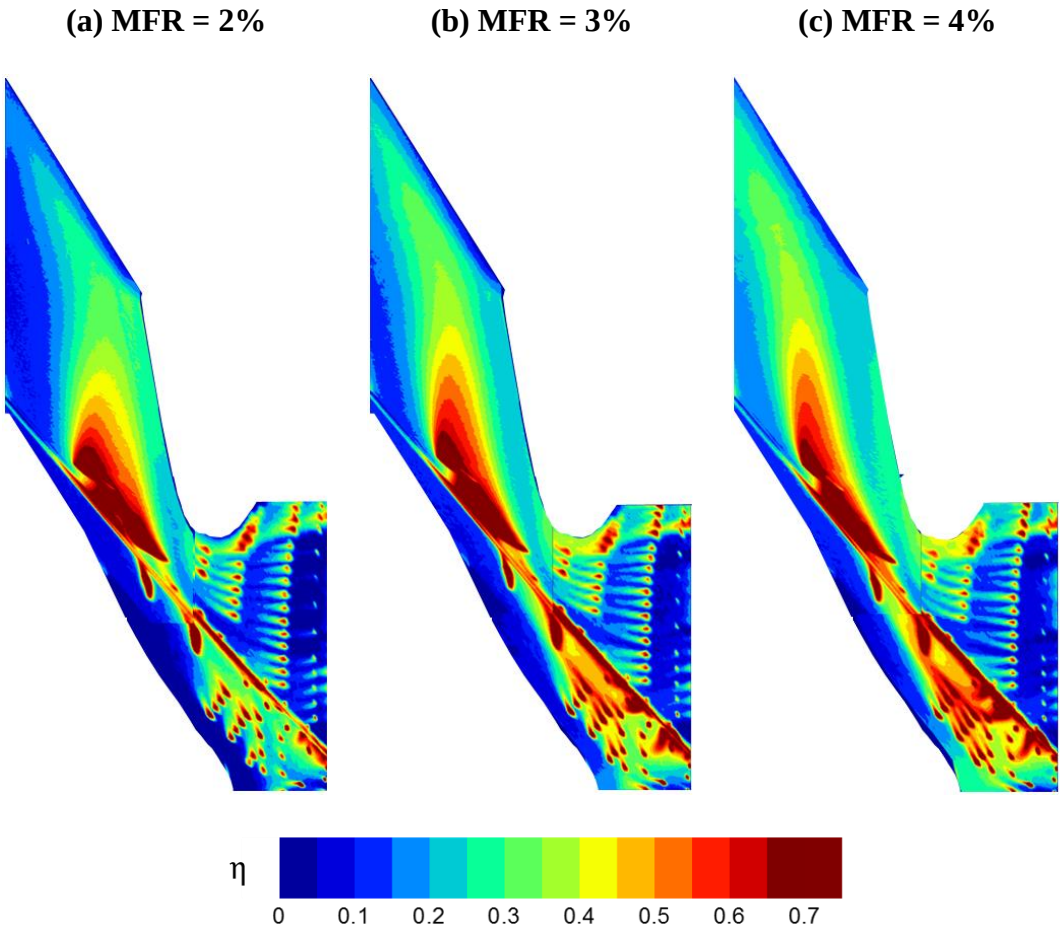

Figure 19. Film cooling effectiveness distributions of design2 at DR = 1.5.

3.5.3.4 Laterally Averaged Film Cooling Effectiveness

The presented spanwise averaged effectiveness is shown in Figure 20. From the data trend, we can see the effectiveness is first gradually increasing up to 43% of the normalized axial distance, with several peaks indicating the local cooling hole locations. And then, a significant effectiveness drops at the location right after the first big cylindrical hole near pressure side passage due to insufficient coolant coverage near vane's pressure side. Following is the effectiveness increase contributed by 3 big cylindrical holes at mid

to downstream of the suction side passage starting from 50% of the normalized axial distance. The effectiveness peak of this region moves according to the MFR and DR. The case with higher coolant momentum (higher MFR and lower DR) will have a local peak value resides in relatively downstream location due to the stronger coolant penetration to further downstream and less tendency of being deflected by the mainstream.

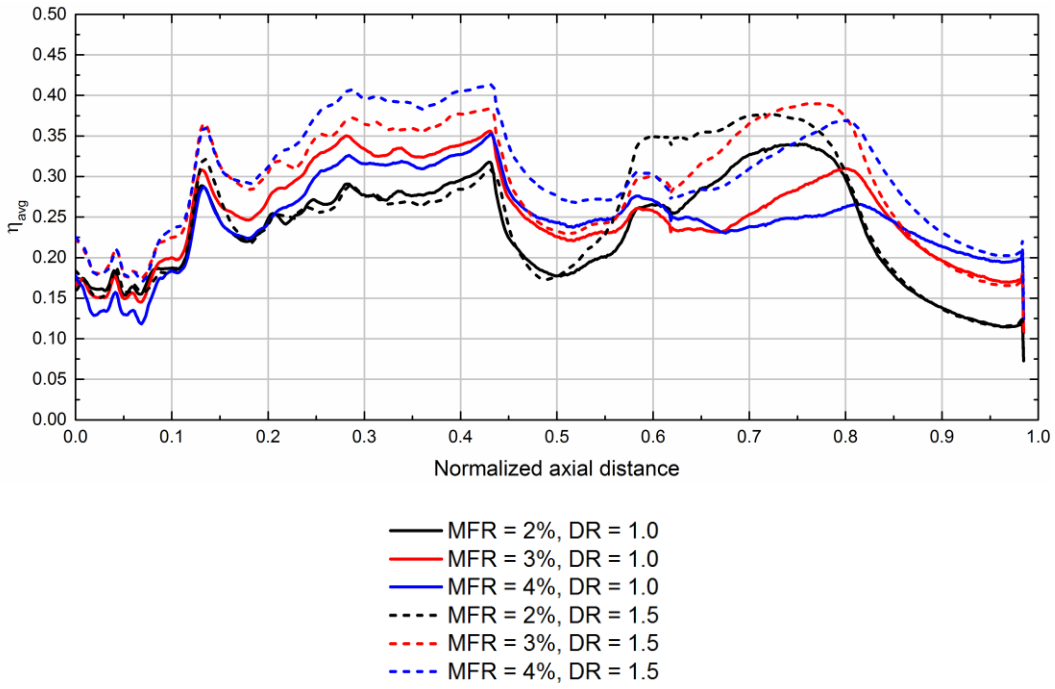

Figure 20. Laterally (spanwise) averaged film cooling effectiveness of design2.

3.5.4 Design Comparison

Differences in the converted contours are observed as the data capturing angle for current design is slightly different from the previous study. For design1, there are 95 typical layback fan-shaped holes dispersed within the majority of the vane passage, 14 angled cylindrical holes are dispersed within the beginning of the passage. Also, there are

16 and 16 angled cylindrical holes along both sides of the slashface gap, respectively. In addition, 31 angled cylindrical holes are uniformly dispersed inside the whole slashface gap. The discrete film cooling hole pattern in the upstream passage of design1 is identical to design2 up to 40% of the normalized axial distance. For the rest of the passage (mid to downstream), 44 fan-shaped holes and 13 angled cylindrical holes are substituted for 5 big angled cylindrical holes adopted in design2. This makes the total cooling hole inlet area for design1 8.1% higher than design2. Under the same amount of coolant supplied, we can see that the effectiveness of two designs is quite different even in the upstream 40% region with identical cooling hole configuration. This is attributed to the different arrangement of cooling holes inside the slashface as well as the cooling hole configuration on the endwall as the local flow resistance for coolant changes. The local blowing ratio for design1 and design2 is expected to be quite different even in the upstream region of the same cooling hole configuration. One key difference is the slashface injection, the effusive coolant from upstream slashface is only visible in design2. On the other hand, the slashface injection for design1 occurs near downstream and creates the signature wedge shape coverage. By comparing Figure 7(a) and (b), the reason for this discrepancy is clearly the hole configurations inside the slashface. For design2, the cooling holes inside the slashface are only dispersed within the first half of the slashface which the coolant can only be ejected through the upstream of the slashface. This effusive coolant alters the upstream local flow fields by introducing additional velocity component which locally reduces the flow resistance near pressure side passage and enhances the effectiveness. The coolant driving force near this area increases by having higher local blowing ratio due to higher

discharge coefficient. On the other hand, when the cooling holes inside the slashface are uniformly arranged along the whole length like design1, the inherent pressure gradient inside the passage will allow the coolant be ejected only near downstream. Another factor is that design2 has very limited amount of cooling holes compared to design1 from the mid to downstream portion of the endwall passage. This downstream blockage in design2 also leads to the front-oriented passage coolant distribution as shown in Figure 18 and Figure 19. By comparing the spanwise averaged effectiveness in Figure 17 and Figure 20, we can see that the effectiveness of both designs gradually increases from leading toward trailing of the vane endwall passage and start to decay at about 80% of the normalized axial distance. Regarding the value, for the first 45% of the normalized axial distance, the effectiveness of design2 is generally higher than design1. Opposite trend is observed for the rest 55% portion. Especially near the nozzle wake region, the film-hole pattern in design1 can effectively diminish the wake effect when increasing MFR while design2 offers only limited coverage. Major differences between two designs are the effectiveness drop in 43% of the normalized axial distance due to poor coverage near mid vane pressure side and the aft passage effectiveness peak shifting due to the coolant momentum change on design2. The above-mentioned two phenomena are not seen on design1. In terms of overall trend, the streamwise effectiveness variation for design1 is less than design2, which is considered beneficial that could lead to more uniform metal temperature and reduced thermal stress. Finally, the area averaged effectiveness for both designs are shown in Figure 21. Design2 outperforms design1 in terms of area-averaged effectiveness for maximum difference of 15% but 6% for most cases at MFR = 2% and 3%, while the

design1 has higher area averaged effectiveness compared to design2 for around 10% at MFR = 4%. Nonetheless, it is not appropriate to simply judge from the area averaged effectiveness to determine which design is better under the same amount of coolant supply due to the dissimilarity of coolant distribution in these two particular designs as shown in Figure 15, Figure 16, Figure 18, and Figure 19. For design2, the effusive coolant from the upstream slashface can be considered over-cooled, as it is not an efficient access to arrange the coolant in such a way that strengthens the portion with existing coolant coverage but leave some regions totally unprotected due to lack of local cooling hole arrangement like the passage near vane's pressure side. In contrast, the region without coolant protection on design1 is relatively limited due to the uniform cooling hole arrangement on the hardware and can be considered a better configuration for this particular vane/endwall passage.

Practically speaking, better/optimum endwall design includes the good thermal performance as well as the low manufacturing cost if possible. The simple hole design in design2 deserves the credit that directly saves lots of manufacturing cost by using simple hole geometry and less number of holes. In design2, it is worthy to reemphasize that the aft portion of the hardware is successfully taken care by 3 big cylindrical holes near suction side of the passage. This is considered a brilliant design to achieve the similar coolant coverage as design1 with merely 3 simple holes for this particular region. However, those 2 big cylindrical holes near pressure side must be shifted since their contribution is pretty limited. Another possible way is to replace them by shaped holes. The better lateral spreading can effectively reduce the unprotected region. Besides, since the total cooling

hole inlet area for design2 is lower than design1, proper modification like placing few more holes near the vane's pressure side and wake region are also recommended on design2 to achieve a full endwall coverage.

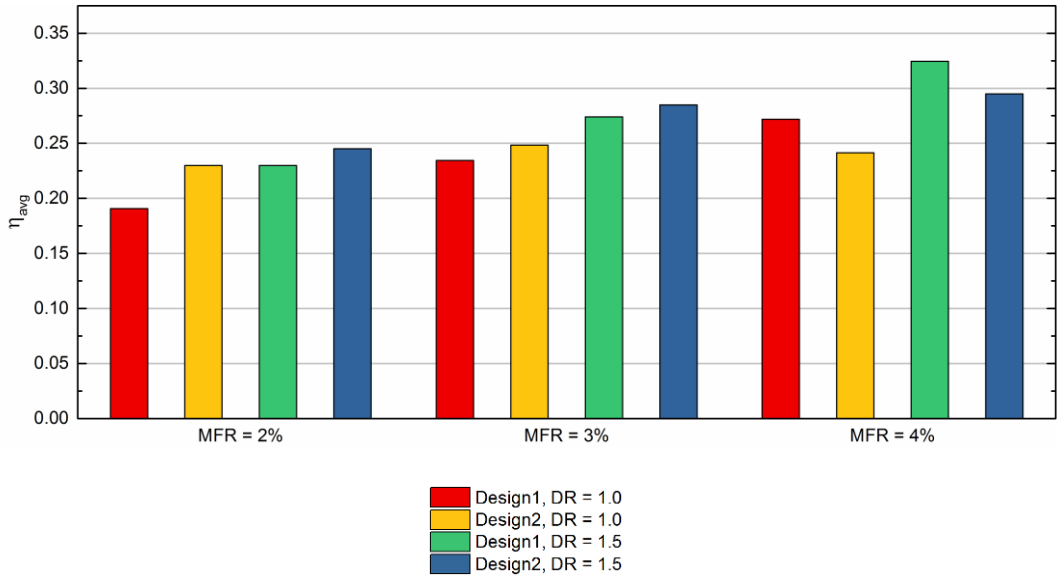

Figure 21. Area averaged film cooling effectiveness of design1 and design2.

4. TRANSONIC TURBINE VANE SUCTION SIDE FILM COOLING WITH SHOWERHEAD EFFECT*

4.1 Literature Review

As mentioned in Section 3.1, from the numerous studies in the open literature, it is found that two major factors affecting the film cooling performance. They are the coolant-to-mainstream condition and the cooling hole design. Considering the pressure and temperature in a real engine, it is difficult to realize the exact mainstream and coolant-to-mainstream condition in the laboratory. Proper scaling factors like coolant-to-mainstream blowing ratio and density ratio were proposed and extensively adopted to simulate the coolant-to-mainstream pressure and temperature ratio in film cooling study. On the other hand, the cooling hole design demonstrates vivid variations including hole geometry and hole spatial arrangement as discussed in Section 3.1 as well. The situation is more complicated than it seems due to the fact that the effects of these parameters are often intertwined and highly related to the vane geometry.

4.1.1 Mainstream Condition Effect

Amid the parameters describing the mainstream condition in film cooling study, Mach number is the one that dictates the flow compressibility but unable to be easily scaled by varying geometry dimension like matching Reynolds number. Studies on

*Reprinted with permission from Shiau, C. C., Chowdhury, N., Han, J. C., MirzaMoghadam, A., Riahi, A., 2017, Transonic Turbine Vane Suction Side Film Cooling with Showerhead Effect Using PSP Measurement Technique, ASME Paper No. GT2017-63143., Copyright 2017 ASME.

matching the typical Mach number in the engine provide insights about how film cooling situation will be under a more realistic flow condition. Further, the geometry induced shock wave in transonic or supersonic flow condition will change the local flow field and affect the film cooling. Liess [49] studied the effectiveness on the flat plate with cylindrical holes under mainstream Mach number from 0.3-0.9 with the favorable pressure gradient. No measurable effect of Mach number on film cooling effectiveness can be seen from his results. Gritsch et al. [50] studied the film cooling with expanded exits under external Mach number from 0.3-1.2. They found that the transonic crossflow at hole exit will alter the flow field in the vicinity of the ejection location. Effectiveness is increased compared to subsonic cases but this enhancement is less prominent for the fan-shaped hole. From their laser light sheet flow visualization, they also found the pressure ratio will affect the coolant distribution in the hole exit plane. And since the higher coolant pressure ratio is required to apply the same blowing ratio under the higher Mach number, it will result in more coolant being ejected at the hole centerline and the lateral spreading is thus reduced. Lutum et al. [51] found that the freestream acceleration generally decreases the adiabatic film cooling effectiveness especially in the far-field of coolant ejection, the reduction can go up from 10-30%. In contrast, increased effectiveness can be achieved in the near hole region due to the reduced tendency of jet separation in the accelerated mainstream. Their data shows the effectiveness obtained at higher Mach number (0.8) is generally higher than those obtained at lower Mach number (0.4). Ochs et al. [52] investigated the effect of shock on film cooling on a simulated suction side with five rows of cylindrical or fan-shaped holes at different locations upstream of the shock. Their results showed that the

effectiveness of cooling hole at the subsonic region is slightly affected by the adverse pressure gradient. However, the mainstream oblique shock does not have a significant effect on the effectiveness of cooling holes at the supersonic region. They also concluded that the increased pressure ratio enhances the flow separation inside the shaped hole which decreases the shaped hole performance and makes it sensitive to blowing ratio similar to the cylindrical hole. Results from Saumweber and Schulz [53] under mainstream Mach number from 0.15-0.45 in 14^o shaped hole show that the performance gain with fan-shaped holes as compared to cylindrical holes is clearly overestimated when it is based on conditions with low turbulence levels and low Mach numbers. At conditions with high pressure ratios across the hole (increased Mach number), separation at the diffuser sidewall will lead to significant performance degradation. Cascade study from Xue et al. [54] demonstrated that the shock causes the effectiveness on blade suction side to drop rapidly and then stays at a low level further downstream. Their CFD results show that pressure gradient drives the near surface flow toward the center and lead to the formation of reversed kidney vortices. Anderson et al. [48] studied the freestream Mach number effect on film cooling of 7-7-7 shaped holes. In the 0.02-0.15 Mach number range, minimal effects on laterally-averaged effectiveness can be detected.

4.1.2 Film Cooling on Vane/Blade Surface

Numerous works of film cooling on the simplified geometry like flat plate were conducted by different groups as a parametric study [9,14,16-19,55]. However, it is expected that the conclusion from flat plate may not necessarily be applicable to the vane

surface, e.g. like the insensitivity of coolant lift-off when using the shaped hole, as the pressure gradient from the vane curvature changes the boundary layer and the characteristics of flow interaction between mainstream and coolant. Also, on the vane surface, the coolant carryover from leading edge showerhead cooling affects the film cooling performance on both vane's pressure side and suction side. For the film cooling study on the vane surface, Colban et al. [56] tested the heat transfer and film cooling on a stator vane with fan-shaped cooling holes. The film cooling effectiveness of four cooling hole rows on the suction side from 9-35% of the surface length showed a large amount of separation with increasing blowing ratio. They considered this to be due to the severe curvature and high acceleration in this region where increasing blowing ratio tends to accentuate the jet lift-off. Najafabadi et al. [57,58] studied showerhead effect on the vane suction side film cooling. For the double rows of fan-shaped cooling holes on the suction side, an increase in blowing ratio from 0.6-0.9 can result in higher effectiveness but will decrease after blowing ratio further increases. They also concluded that showerhead cooling makes a major contribution to improving cooling performance when the cooling row is located at high convex surface curvature with accelerating flow as it can decrease the severity of the jet separation. Based on the above survey and the previous studies on transonic vane film cooling [59-61] from The Turbine Heat Transfer Laboratory (THTL) at Texas A&M University, it is clear that the film cooling performance on the vane surface under different mainstream Mach numbers cannot be simply predicted from the flat plate study and the more in-depth investigation is needed especially when dealing with specific vane geometry.

4.2 Experimental Setup and Method

4.2.1 Five-Vane Annular Sector Cascade

The flow loop for the current test rig is shown in Figure 22. Referring to Figure 23, the measurements were conducted in a five-vane annular sector cascade. The cascade consists of four guide vanes and one removable center vane as test vane to simulate the radial pressure gradient and reflect the three-dimensional secondary flow effect in the true geometry. The shape of cascade inlet cross-section is designed as an annular sector of the combustion chamber exit in order to match the flow entering the geometry of vanes in the test section. The metal cascade and the reinforcement cover for the window are made by selective laser sintering (SLS) process. The removable scaled test vane is made from a sturdy resin material called Somos® NanoTool using stereolithography (SLA) process. The test vane is of three-dimensional design with aspect ratio around 0.7 and solidity around 0.5. Due to the cascade design and the safety concerns when operating this wind tunnel, a limited size transparent Plexiglas window is used to ensure reasonable optical access to part of the suction side of test vane (Figure 23(a)). The mainstream air is supplied by a blowdown facility including a high-pressure compressor, a dryer, and a storage tank. The mainstream is regulated by an electronic flow control valve that regulates the flow velocity through the feedback signal from the pressure transducer in the wind tunnel flow loop.

Both the inlet and exit velocities from the total pressure and static pressure of the cascade were continuously monitored by Pitot-static probes, which were stationed at 2.87

C_{ax} upstream and 0.75 C_{ax} downstream of the center vane, respectively. Three nominal mainstream conditions with exit Mach number from 0.7, 0.9, to 1.1 were tested. The corresponding Reynolds number based on axial chord length are $6.6x10^5$, $8.9x10^5$, and $1.36x10^6$. To simulate the flow turbulence intensity entering the turbine vane, a turbulence grid design based on grid-generated turbulence decay correlation [44] was used. The grid has an equivalent bar width 1.43 cm and 54% porosity, was set 25.45 cm upstream of vanes' LE plane with an estimated turbulence intensity of 12% and integral length scale of 1.5 cm. A strobe light and a monochrome CCD camera were used for surface intensity capturing for film cooling effectiveness calculation. The whole cascade and setup of the data acquisition facility are shown in Figure 23(b).

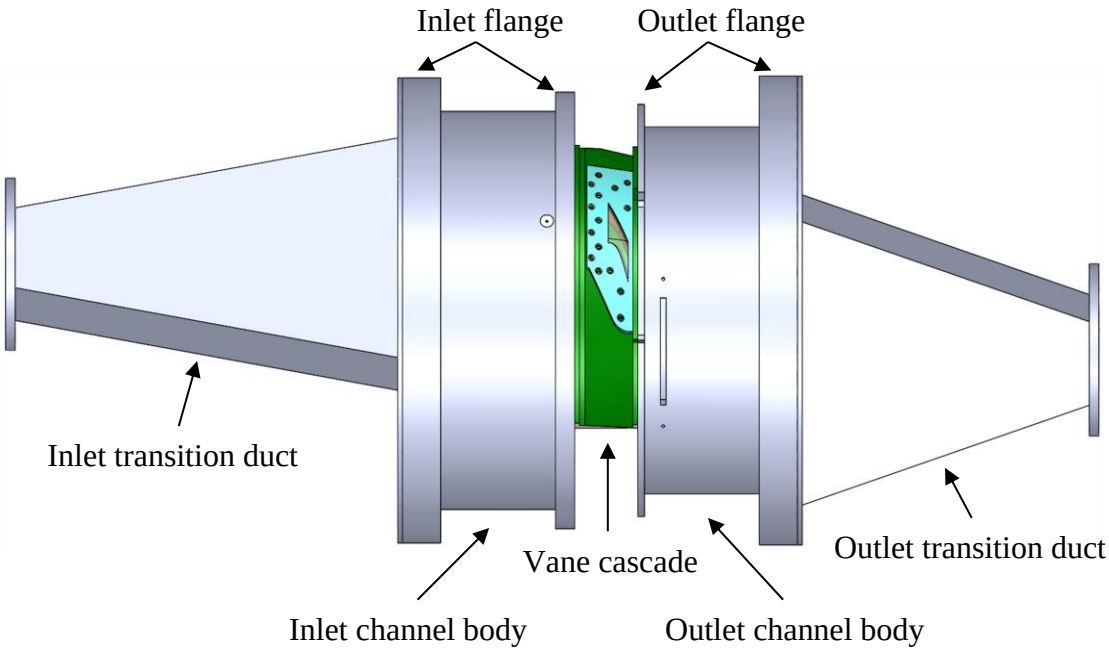

Figure 22. Flow loop for the test section and facility.

(a)

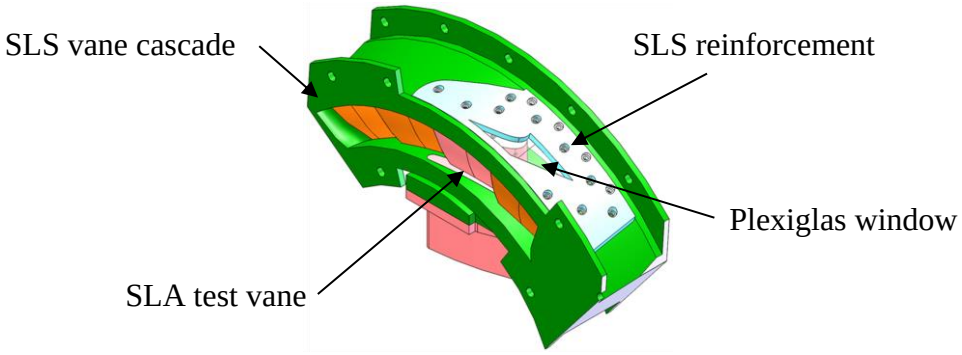

(b)

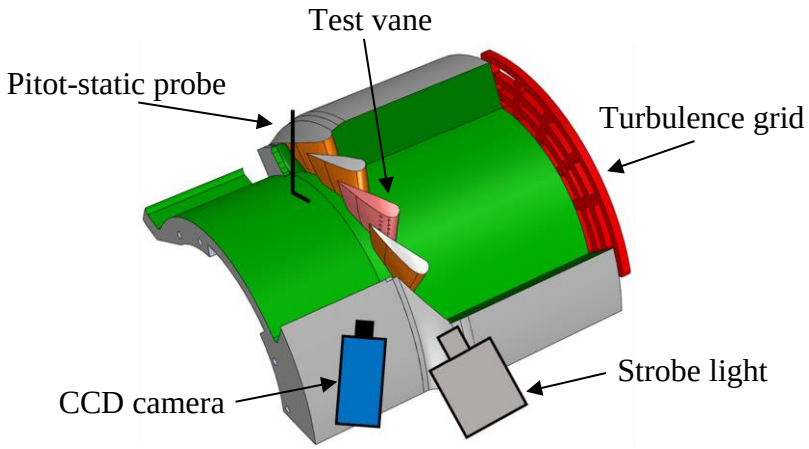

Figure 23. Schematic view of the vane cascade and instrumentation setup. (a) Cascade assembly; (b) Cascade and DAQ facility setup.

4.2.2 Film Cooling System

There are five rows of film cooling holes dispersed on the surface of center test vane as shown in Figure 24(a). The diameter (d) of the cooling hole is around 0.12 cm. Purple shaded area indicates the area of interest (AOI) on the vane's suction side, which represents the optically accessible portion through the window in this study (the red dashed line in Figure 24(b)). The LE of the test vane is equipped with three rows of

showerhead film cooling holes (LE) in a staggered configuration. The middle row is aligned with the stagnation line. Each showerhead row has seven radial-angle (injecting towards the vane tip) cylindrical holes with a hole-to-hole spacing of s/d = 6.9. Two rows of compound-angle shaped holes (SS1, SS2) are on the suction side of the test vane with a wide hole-to-hole spacing of s/d = 7.3. The shaped holes have a typical design of metering length and expansion angle in three directions. The injection angles for SS1 and SS2 are approximately 45^o and 35^o, respectively. These two angles are different due to the local vane curvature. The bottom of the test vane is extended 5.08 cm and serves as a three-passage plenum for the film cooling hole rows to enhance the uniformity of coolant delivery (Figure 24(a)). Three white cavities, which are inside the vane cross-section shown in Figure 24(b) represent three passages of the plenum. One of the plenum passages supplies coolant for three rows of leading edge cooling holes (LE), the other two plenum passages supply coolant for SS1 and SS2, respectively. The true data capturing angle and the schematic of the coolant loop are shown in where coolant source is either the dry air from the compressor loop or the foreign gas cylinders including N_2 (DR = 0.97 ≈ 1.0), CO_2 (DR = 1.52 ≈ 1.5), and Argon/SF_6 mixture (DR = 1.93 ≈ 2.0). Coolant flow rate for different plenum chamber/passage is controlled by individual rotameters. The coolant volume flow rates are further adjusted with the specific gravity correction when flowing foreign gas and applied density correction from the pressure tap reading at rotameter exits.

(a)

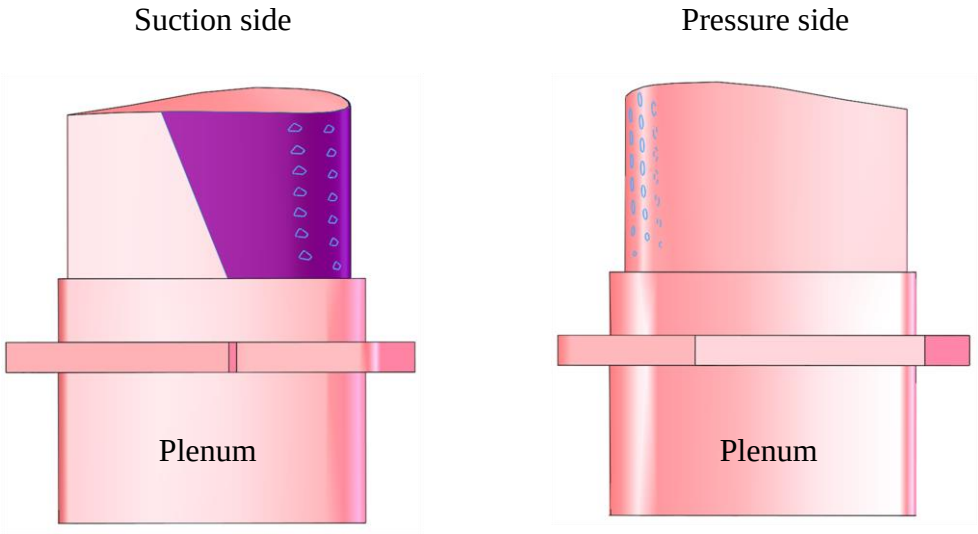

(b)

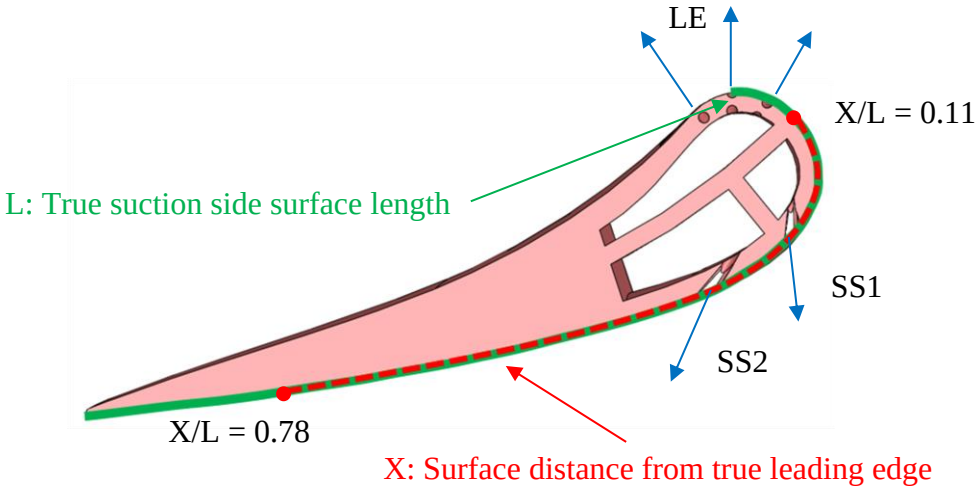

Figure 24. Test vane. (a) Film cooling hole locations and plenum; (b) Section view of coolant supply passages (the red dashed line is the top view of DAQ area).

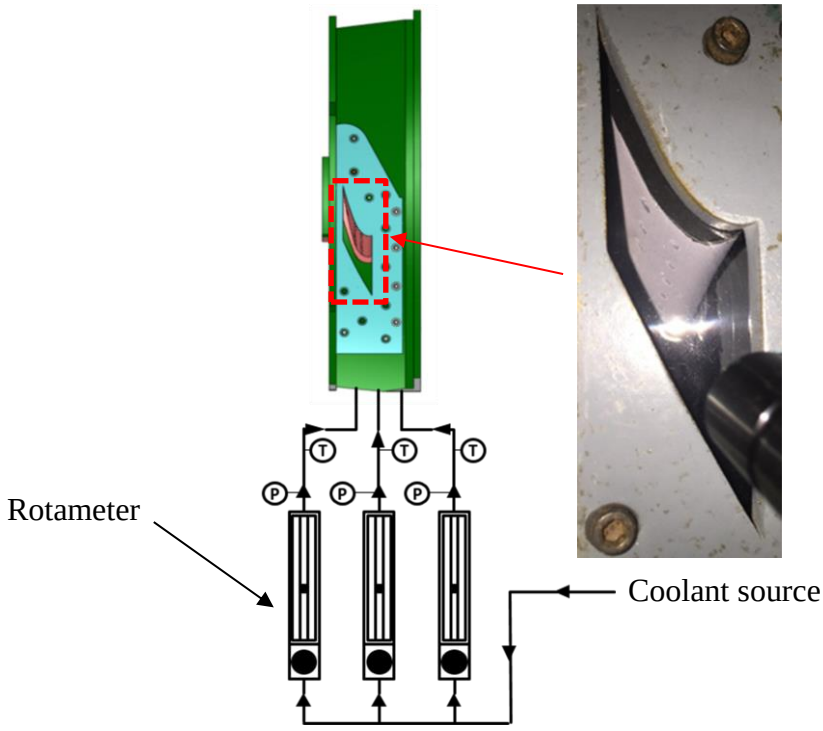

Figure 25. Test section with true data capturing angle and the schematic of coolant loop.

4.2.3 Experimental Method – Pressure-Sensitive Paint

Mass transfer based pressure-sensitive paint (PSP) is used to capture the film effectiveness as mentioned in Section 3.2.3. The major difference between Section 3 and the current one is the light source and therefore the PSP (Innovative Scientific Solutions Inc., UF-470) with a shifted excitation peak wavelength (470 nm) is used. Strobe light (PerkinElmer MVS-7000 Series) fitted with a narrow bandpass interference filter (optical wavelength 520 nm) is used to excite the luminescent molecules in the polymer binder. A pair of flexible fiber optic guides directs the light onto the vane surface. The emission intensity of the painted surface is recorded through a long pass filter (600 nm) using monochrome scientific grade CCD camera (Cooke Sensicam QE with CCD temperature

maintained at 258 K using 2-stage Peltier cooler, 12-bit dynamic range). The camera and strobe light were synchronized by a TTL signal from a function generator to achieve 10Hz data acquisition frequency.

Due to the transonic flow condition, there is a potential concern whether the heat and mass transfer analogy is valid in compressible flow, regardless which mass transfer method is being used. For the case without film cooling, Häring and Weigand [62], and Häring et al. [63] revised the analogy equations and verified the validity of heat and mass transfer analogy in compressible flow by using naphthalene sublimation technique and compared with the transient liquid crystal technique in compressible flow (Ma = 0.4-0.8) for various geometries including a flat plate, cylinder, and the turbine airfoil. For the film cooling effectiveness using PSP technique, its validity has been verified with thermal techniques as shown by Wright et al. [64] and Wiese et al. [65]. However, the results were obtained in the low-speed wind tunnel (incompressible flow), and such direct comparison is yet available for compressible flow in the open literature. Therefore, it will be more appropriate to reexamine the key basis that enables the foreign gas injection technique to be used in film effectiveness measurement. To use the mentioned technique for film cooling measurement, the nature of turbulent boundary layer dictates that the diffusivity between heat and mass needs to be established for molecular ones as well as for turbulent ones. Such relationship is not the case for most of the applications, but for the turbulent/mixing nature of film cooling particularly, there is a consensus that the turbulent Sc and Pr are approximately equal and the shear layers present in film cooling flows help to facilitate this relationship as indicated by Jones [66]. It is reasonable to consider the

thermal and mass diffusion happening in the turbulent boundary layer is expected to follow the revised analogy indicated by [62]. From the analogy, the effect of Ma is eliminated when a unity Lewis number presents. In addition, high-speed flow directly relates to high dynamic pressure, but the static pressure varies accordingly and so as the local flow density. From the definition of thermal and mass diffusivity, density variation from pressure affect these two diffusivities equally and the effect is canceled out. The resulting Lewis number is not being affected. It is therefore considered valid to use PSP technique for adiabatic film cooling effectiveness measurement in compressible flow.

As the AOI in this study, the suction side of the test vane was first sprayed with black paint to reduce the surface stray reflection and then painted with 4-5 layers (30-40 μm thickness per layer) of PSP by using an airbrush. The relationship between this particular PSP emission intensity is calibrated separately. The final result is one correlation as shown in Figure 26. In addition, since PSP is insensitive to camera angle as mentioned in Figure 11(c), the steep data taking angle in this experiment did not cause any concern.

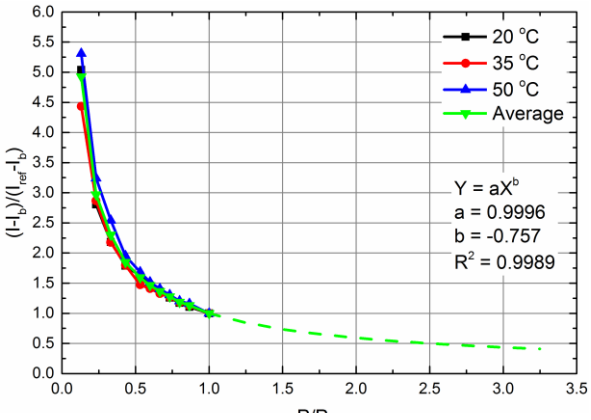

Figure 26. PSP calibration results under different reference temperature.

4.3 Test Matrix

Since the current setup uses the blowdown facility to supply the mainstream, it is important to confirm the mainstream is kept on the desired steady condition within the data taking duration. Figure 27 is the Mach number history of the current test facility. It is confirmed that the claimed flow conditions can be sustained steady for at least 10 seconds which is sufficient considering the data acquisition frequency described in Section 4.2.3.

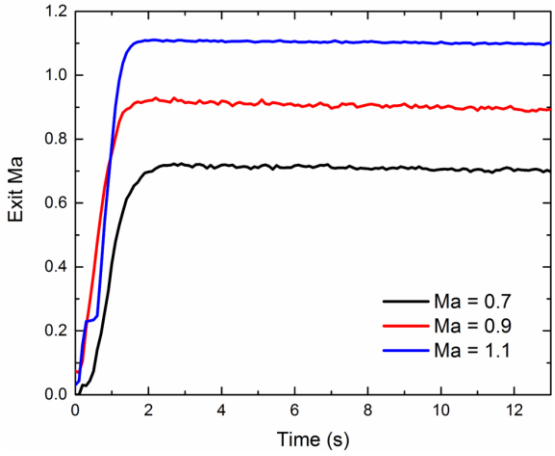

Figure 27. Exit Mach number history for the current test section.

To systematically study the film cooling performance under different mainstream flow conditions, 27 sets of experiments were conducted to study the effects of coolant-to-mainstream blowing ratio (M) and density ratio (DR) on the film cooling effectiveness from high subsonic to transonic flow condition. As the mainstream accelerates from the vane's LE toward TE, the local mainstream mass flux for cooling hole row at different locations of the vane suction side is subjected to vary and affects the M calculation. Since the individual passage supplies the coolant in a particular cooling hole group (LE, SS1, SS2), row-average M is used and calculated by

$$\dot{m}_c = M \times \sum_{i=1}^{n} (\rho_m v_m)_r \times (A_c)_r \quad (3)$$

Where r represents the cooling hole group. For row-averaged M calculation in this study, the local mainstream mass fluxes for SS1 and SS2 rows were calculated based on the isentropic Mach number distribution on the vane surface from the surface static pressure measurement by PSP and the inlet total pressure from Pitot-Static probe. On the other hand, since the LE rows are not in the optically accessible portion, the surface Mach numbers in this region were obtained from the interpolation of in-house CFD simulation.

In addition, the vane experienced surface temperature change from aerodynamic heating due to the transonic freestream velocity. The recovery temperature on the vane surface varies locally according to surface Mach number distribution. It can be calculated by

$$T_r = T_s \left(1 + r \frac{\gamma - 1}{2} Ma^2\right) \quad (4)$$

The maximum temperature difference between recovery and freestream is around 6.2 ^{o}C at exit Ma = 1.1. Since this flow-induced temperature distribution is not reproducible in the reference condition (without flow), this will result in a maximum 2.5% discrepancy in the measured PSP emission intensity from the temperature sensitivity suggested by PSP manufacturer. The corresponding uncertainty in the effectiveness will thus be included in the uncertainty analysis. Summary of the test matrix is shown in Table 2.

Table 2. Summary of the test matrix of the transonic vane suction surface film cooling study.

Experiment #	Exit Ma	DR	Row-averaged M (LE, SS1, SS2)
1-3	0.7	1.0	0.7, 1.0, 1.6
4-6	0.7	1.5	0.7, 1.0, 1.6
7-9	0.7	2.0	0.7, 1.0, 1.6
10-12	0.9	1.0	0.7, 1.0, 1.6
13-15	0.9	1.5	0.7, 1.0, 1.6
16-18	0.9	2.0	0.7, 1.0, 1.6
19-21	1.1	1.0	0.7, 1.0, 1.6
22-24	1.1	1.5	0.7, 1.0, 1.6
25-27	1.1	2.0	0.7, 1.0, 1.6

4.4 Experimental Uncertainty

The uncertainty of the measurement in this experiment comes from the fluctuation of mainstream velocity (±1.5%), and the fluctuation of coolant flow rate (±3.8%). For the film cooling effectiveness calculation, the major uncertainty is the variation of PSP emission intensity value captured by the camera. Multiple reference and black images were first taken to quantify the intensity fluctuation. Also, the discrepancy in surface temperature distribution between the conditions with and without flow will result in additional 5.6% uncertainty in the measured pressure ratio (w.r.t. to atmospheric pressure). By the method proposed by Kline and McClintock [46] based on a 95% confidence level,

the uncertainty of film cooling effectiveness deduced from the calibration curve at $\eta = 0.1$, 0.3, 0.5 and 0.7 are 13%, 4.2%, 2.4% and 1.8%, respectively in the present study.

4.5 Results and Discussion

4.5.1 Static Pressure Measurement on the Vane Suction Side

The static pressure distributions of AOI on the vane suction side were measured by PSP under the condition with mainstream only as shown in Figure 28(a). Red dashed line in each subfigure represents the same portion mentioned in Figure 24(b). Black dashed lines in each subfigure represent SS1 and SS2 hole locations. The static pressure distributions were converted to isentropic Mach number distribution by incorporating the total pressure value from the inlet Pitot-Static probe under different mainstream conditions as shown in Figure 28(b). To better highlight the local variation in both surface static pressure and Mach number, each figure has its own color bar range. The static pressure and isentropic Mach number at the mid-span of the current vane's suction side are also extracted from Figure 28(a)(b) to demonstrate the loading as well as to label the throat location as shown in Figure 29. Although the true LE is not visible in the AOI, there is a clear trend that the static pressure is very high in the vicinity portion of the LE and then gradually decreased toward the TE. This demonstrates a typical flow behavior at which the mainstream accelerates along with the vane surface. The higher Ma after SS2 in the near hub portion is due to the flow acceleration from the passage contraction toward TE. From Figure 28(a) and Figure 29(a), the static pressure is nearly monotonically decreasing toward the throat and then gradually recovering as shown in exit Ma = 0.7 and 0.9 cases.

From Figure 29(b), it is clear that for these two subsonic conditions, the maximum Ma happened at the throat location. But when the exit Ma = 1.1, static pressure abruptly recovers, then further decreases after SS2 as can be seen in Figure 28(a) and Figure 29(a). From Figure 29(b), the corresponding abrupt Ma decreasing then increasing starting from X/L = 0.55 is also observed for exit Ma = 1.1. Since the flow is still in supersonic condition before and after this abrupt velocity change as shown in Figure 28(b) and Figure 29(b), it is therefore considered a direct evidence of oblique shock wave that impinges on the vane suction side. Under the transonic flow condition, this is identified as the TE oblique shock which is generated from the pressure side of the neighbor vane and impinges on the suction side of the test vane which alters the surface Mach number/static pressure distribution. The interaction between the shock wave and local film cooling will be further discussed.

(a)

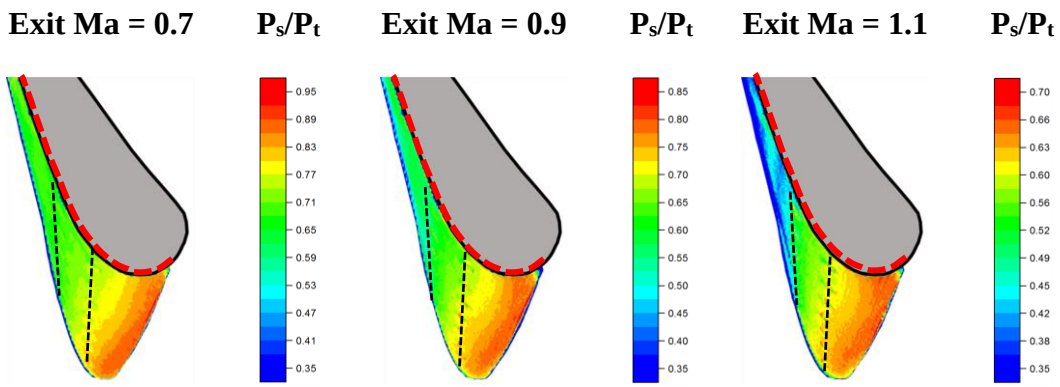

P_t = 7.6 psig **P_t = 13.9 psig** **P_t = 28.6 psig**

(b)

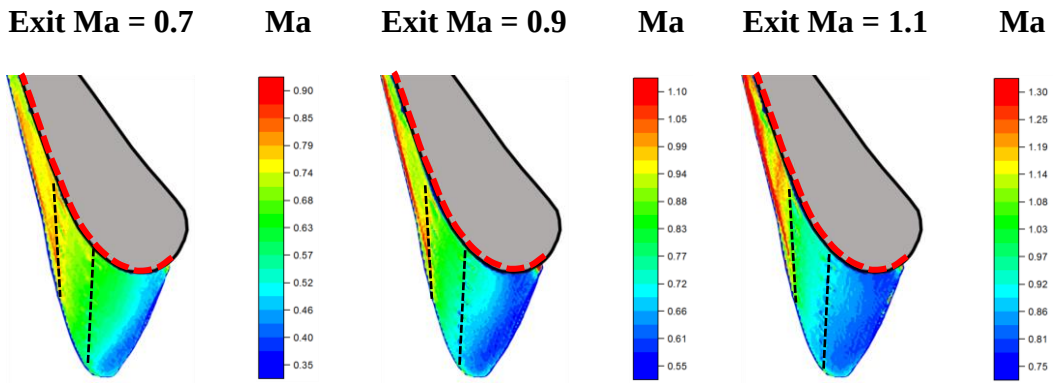

Figure 28. Vane surface. (a) Static pressure distribution; (b) Isentropic Mach number distribution.

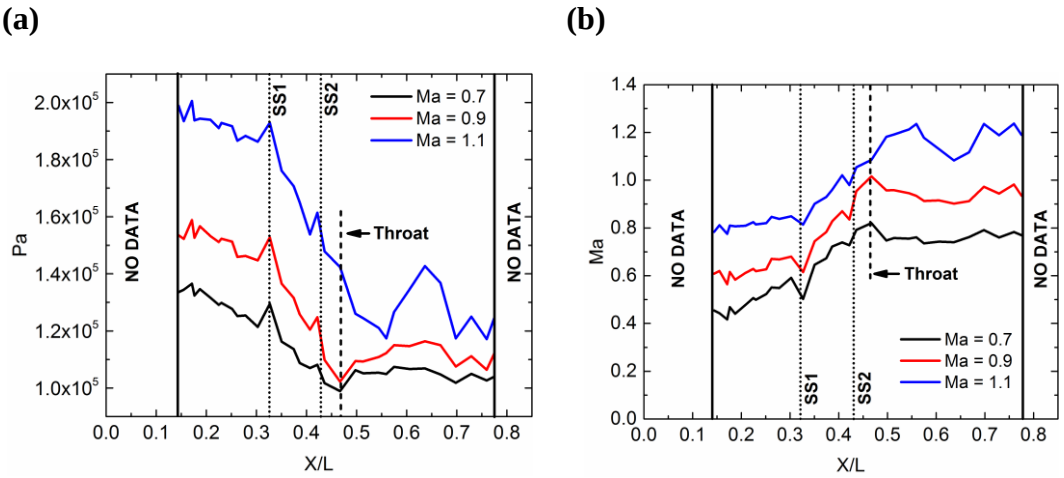

Figure 29. Load distribution at mid-span of vane's suction side. (a) Static pressure; (b) Isentropic Mach number.

4.5.2 Adiabatic Film Cooling Effectiveness

First, an interesting phenomenon that was brought to the authors' attention is the unsteady behavior of the coolant carryover from LE observed during the experiments. The reason can be attributed to the pressure pulsating from the high turbulence. This high turbulence is originated from the enhanced equivalent Tu of flow stagnation as mainstream approaches the LE and the showerhead injection, as it is already confirmed in the literature that the showerhead cooling will locally produce high turbulence due to coolant-mainstream interaction. Results in Figure 30(a) are the laterally averaged effectiveness reduced from 9 different time sub-periods in one representative case during measurement. The laterally averaged effectiveness is divided into three regions, R1, R2, and R3 for regional discussion. They represent regions before SS1, between SS1 and SS2, and after SS2, respectively for easy identification on vane's suction side. It can be seen that the results are actually time-dependent. The deviation% shown in Figure 30(b), is defined as

the standard deviation divided by the average of these sub-cases. It clearly shows the fluctuation of R1 region is highest as it can go up to 24%. This is considered the outcome of both the pressure pulsating and the inherent higher uncertainty from low effectiveness value. However, time-averaged Tu effect on the effectiveness is considered included in the measurements already. As the film effectiveness in LE region is relatively low and therefore with higher uncertainty, it will require further investigation to separate and quantify the pulsating behavior observed.

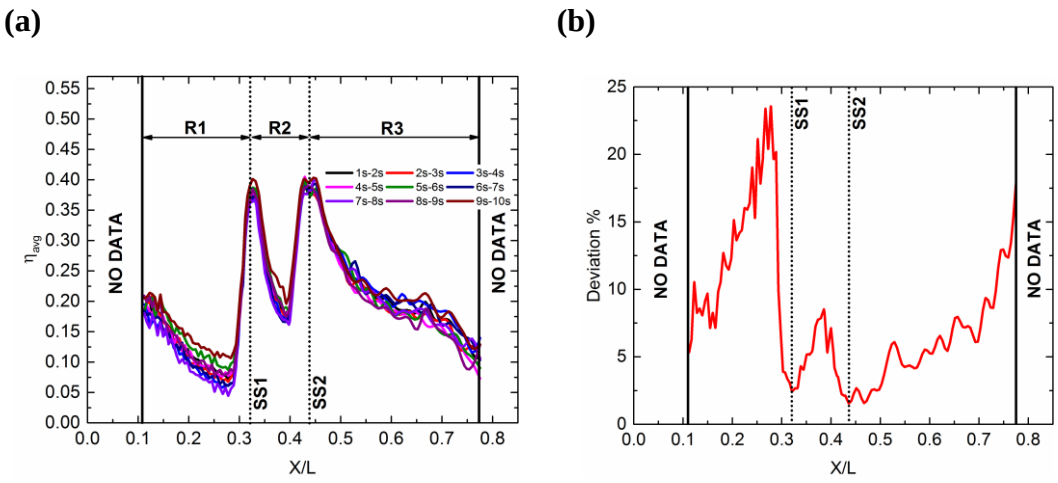

Figure 30. Laterally averaged effectiveness for a selective case. (a) Time-dependent effectiveness; (b) Deviation percentage due to effectiveness fluctuation.

The adiabatic film cooling effectiveness for selective cases are shown from Figure 31 to Figure 34. Red dashed line in each subfigure represents the same portion mentioned in Figure 24(b). Firstly, 7 distinct coolant traces can be observed in the region near LE, they are the coolant carryover from the LE holes. The radial angle of the showerhead holes on LE explains the situation that the carryover near the vane tip is slightly stronger than near the hub. Secondly, the coolant traces from SS1 and SS2 pretty much cover the

majority of the AOI. Due to the wide spacing between the suction side hole and the in-line configuration between rows, the coolant traces from SS1 and SS2 are distinct as expected instead of laterally overlapping. The coolant carryover from LE remedies the situation by filling up the gap between holes in SS1. The surface static pressure along a given cooling hole row is found to be quite uniform along the vane span as shown in Figure 28(a). In this case, even the current plenum passage design might lead to more coolant stagnated near the vane tip, the difference between discharge coefficients for holes in a given row are considered to be small. All the contour plots showed in Figure 31 to Figure 34 prove this argument that most coolant traces from SS1 are quite uniform. The same argument is expected to be true for SS2. From the uniform traces along the vane span, it is verified that the individual M of each hole in a particular row is actually pretty close to the row-average M. However, the coolant trace from SS2 is visually affected by the perspective distortion from the steep data capturing/view angle. Under this distortion, the spacing between coolant trace is visually reduced. While the individual traces from the top 3 holes of SS2 is still distinguishable in most of the cases, the traces of bottom 4 holes are squeezed together. Two potential concerns about data in this region are 1. If the effectiveness value captured under steep angle is reliable; 2. If the perspective distortion affects the measurement value. As mentioned in the experimental method section and shown in Figure 11(c), it is proven that the camera captured PSP intensity is insensitive to the camera angle even if it's very steep. The authors, therefore, have the confidence that the effectiveness of this region is reliable. Also, to the authors' understanding, the perspective distortion deforms the area of interest with respect to the relative distance and the angle of

view, but it does not alter the measured value. For the laterally averaged effectiveness shown in Figure 35 - Figure 37, the authors have tried to use both the original contours (Figure 31-Figure 34) and the unwrapped ones to calculate the averaged effectiveness, and both results are in good agreement. Therefore, the averaged effectiveness presented in this study are directly calculated from the original contours.

4.5.3 Effect of Blowing Ratio

The level of coolant momentum is controlled by varying blowing ratio which directly affects the film cooling performance. Two extreme DR and exit Ma are selected to discuss the effects of M as shown in Figure 31 and Figure 32. The row-averaged blowing ratio is increasing from left to right (from 0.7 to 1.6). For low DR with low exit Ma cases shown in Figure 31(a) and Figure 32(a), there is a clear trend that while the coolant carryover from LE somewhat enhances when increasing blowing ratio, the effectiveness of SS1 and SS2 actually reduce when the blowing ratio increases. The coolant traces from SS1 and SS2 shrink both in streamwise and spanwise directions, indicating a jet separation with elevated blowing ratio. For the blowing ratio range in the present study, this trend may seem to be counterintuitive for the shaped hole. However, considering that SS1 is located in 32% surface length with convex curvature and high acceleration, the jet tends to lift-off even for the shaped hole as reported in the aforementioned literature [56-58]. With high DR at low exit Ma, the blowing ratio effect demonstrates a different behavior as shown in Figure 31(b) and Figure 32(b). The coolant carryover from LE is nearly monotonically enhanced with increasing blowing ratio. This

is considered beneficial to the suction side holes in high convex curvature region that jet lift-off will be lessened as reported by Najafabadi et al. [57,58]. For the SS1 and SS2, the jets tend to be adhered to the vane surface even at higher blowing ratio up to M = 1.0 then start to separate from the surface. This delayed jet separation is attributed to both the low momentum in heavy coolant as well as the strong contribution by LE carryover from showerhead cooling. At high exit Ma, the effectiveness seems to be even higher when blowing ratio reaches 1.6 with high DR especially after SS2, this is considered due to the oblique shock wave effect.

Laterally averaged effectiveness for all DR and two extreme exit Ma are shown in Figure 35(a)-(c). The trend in region R1 is quite ambiguous. But the mixing from low-density coolant with mainstream could be the reason lead to seem insensitive blowing ratio effect as reported for DR = 1.0 since the coolant lift-off is happening even in the lowest blowing ratio tested. In contrast, the coolant momentum for DR = 2.0 is lower, as long as this momentum is sufficient to overcome the surface pressure to form converge, a typical blowing ratio characteristic is observed. The effectiveness in this region is the result of the combined effect with pressure pulsating including higher uncertainty mentioned earlier. For region R2 with low and moderate DR, increasing blowing ratio demonstrates a negative impact on effectiveness. With high DR, the optimal blowing ratio shifts to 1.0 and the effectiveness shows an increasing then decreasing trend as blowing ratio increases, but the sensitivity of effectiveness on blowing ratio decreases. For region R3 with low DR at low exit Ma, the detrimental effect of increasing blowing ratio is observed. But at high exit Ma, the coverage from high momentum coolant is enhanced from the shock wave. On

the other hand, coolant coverage from low momentum coolant for high DR can further increase as blowing ratio is higher, but for the supersonic condition, the benefit from shock wave is not as much as the high momentum coolant (not penetrating mainstream).

4.5.4 Effect of Density Ratio

Coolant momentum is also varied when density ratio changes under the same M. For the same M, the effects of density ratio are also shown when comparing in Figure 31(a) and (b), as well as Figure 32(a) and (b). It is obvious that the density ratio effect is getting prominent when M increases. At low exit Ma, increasing the density ratio leads to a comprehensive effectiveness enhancement within nearly all the AOI. Due to the reduced momentum in high density ratio, the coolant is less susceptible to lift-off or penetration into the mainstream. It will directly lower the tendency of mixing between the coolant and mainstream and result in better spreading and higher effectiveness. At high exit Ma with high density ratio, LE carryover seems to be weaken compared with low density ratio case except for M = 1.6. The reason might be due to the largely increased surface static pressure near LE from high inlet total pressure which decreases the discharge coefficients of LE. Under low and moderate M, the heavier coolant does not have enough momentum to overcome the huge stagnation pressure. For the portion with lower static pressure like SS1, the jets demonstrate strong density ratio effect, especially near the hole exit. This is considered solely the contribution from reduced jet momentum. The density ratio effect is still observed for SS2 near the hole exit. However, downstream region after SS2 shows a complicated behavior where the low density ratio case actually outperforms the high

density ratio case. Since this is observed only in high exit Ma, the phenomenon can be explained by the shock wave as beneficial for the coolant attachment when the coolant is lifted-off (high momentum), which will be further discussed in the exit Mach number effect.

Laterally averaged effectiveness for all M and two extreme exit Ma are shown in Figure 36(a)-(c). For region R1 with low and moderate M at both exit Ma, effectiveness shows an increasing then decreasing trend when density ratio increases. Density ratio 1.5, therefore, is an optimal value for this high-pressure zone. For region R2 with low M, density ratio effect is the same as region R1. When M is elevated, positive density ratio effect on effectiveness is observed especially for high M at both exit Ma. For region R3 with low M, the density ratio effect on effectiveness is the same as region R2. For moderate and high M, especially at high exit Ma, random trend is observed considering the composite effect of both density ratio and non-uniform pressure from the oblique shock wave. From Figure 36, it is clear that the effectiveness when DR = 1.5 is consistently better than DR = 1.0, on the other hand, DR = 2.0 only outperforms DR = 1.5 for high M. It is because when density ratio increases, coolant momentum as well as the jet separation tendency simply get suppressed. This characteristic, however, can be detrimental to the effectiveness if the coolant momentum is insufficient. In other words, density ratio effect really stands out when the heavier coolant is accompanied with higher M.

4.5.5 Effect of Exit Mach Number

The effects of varying exit Ma on film cooling are shown in Figure 33 and Figure 34. When exit Ma increases from 0.7 to 0.9, all the jets become wider with the increased centerline and near hole effectiveness. However, this trend seems to reach a plateau when the exit Ma further increases to 1.1. From the vane surface Ma distribution showed in Figure 28(b) and Figure 29(b), it is clear that increasing exit Ma leads to increasing surface Ma. From subsonic to transonic condition, the effectiveness enhancement could be mainly due to the boundary layer (BL) behavior. The BL thickness on the vane surface is considered to reduce at higher exit Ma. This thinner BL leads to higher near wall mainstream velocity, causing stronger bending of the jets toward the wall and increasing effectiveness. It is found that the BL behavior also relieves the coolant lift-off as shown in Figure 33(b). This is similar to the finding reported by Saumweber and Schulz [53]. Following the same logic, at exit Ma = 1.1, the higher near wall velocity should further enhance the effectiveness. Surprisingly, this is not always the case as the jet is additionally affected by both showerhead behavior and the influence of oblique shock on the downstream portion of SS2. By carefully comparing the contours in Figure 33 and Figure 34, the centerline effectiveness for SS1 seems to be higher for exit Ma = 1.1 than Ma = 0.9. This is believed to be due to the elevated near wall velocity mentioned earlier. But at exit Ma = 1.1, the weakened coolant carryover from LE case does not have the equivalent superposition effect on downstream effectiveness as happened for Ma = 0.9 cases, therefore results show similar effectiveness for the region near SS1. For SS2, the higher centerline effectiveness for Ma = 1.1 compared to Ma = 0.9 is still noticeable. Conversely,

at both exit Ma = 0.9 and 1.1 under low M, film coverage in the region after SS2 seems to be indistinguishable as shown in Figure 33(a) or even detrimental as shown in Figure 34(a). According to the Ma distribution shown in Figure 28(a) and Figure 29(b), the reason can be attributed to the oblique shock. This shock wave is believed to have a mixed effect on the effectiveness confined in this supersonic flow region. The oblique shock impinges after SS2 altering the local pressure field, increasing the static pressure, and thickening the BL. In addition to the enhanced mixing, the local flow resistance for coolant increases under these circumstances. It is a counter effect to the effectiveness enhancement is the higher near wall velocity from thinner BL. On the other hand, from the understanding of gas dynamics, the oblique shock forces the flow after the shock to be parallel to the vane surface, which is considered beneficial to the film distribution. This effect is especially prominent when the coolant momentum is relatively high as the jet penetrates further into the mainstream. This can explain the reason that compared to the Ma = 0.9 cases, effectiveness enhancement after SS2 in Ma = 1.1 only existed at high M.

The laterally averaged effectiveness comparison for exit Ma effect can be observed in Figure 37 for two extreme DR at low and high M. For region R1 with low DR, increasing Ma demonstrates an increasing then decreasing trend on the effectiveness regardless of M; at high DR, monotonically decreasing tendency in effectiveness with increasing Ma is presented. For the same M, higher stagnation pressure at higher exit Ma condition directly restrains the showerhead cooling performance which further reduces the effectiveness from LE coolant carryover. For region R2, increasing exit Ma reveals a positive effect by the thinner BL. For region R3 with low DR, exit Ma pretty much has

the same positive effect on effectiveness as region R2. Especially at high exit Ma, the oblique shock wave impingement helps the high momentum coolant to be parallel/attached to the surface. For low momentum coolant (high DR), increasing exit Ma from 0.7 to 0.9 does not have any significant effect. The thinner BL might have a marginal effect on effectiveness due to the fact that the jet is considered not evenly penetrating the BL. With high M at high exit Ma, the oblique shock nature benefits the effectiveness by the mechanism mentioned earlier.

4.5.6 Engine-like Condition

Due to the complicated effect from varying blowing ratio, density ratio, and exit Mach number on the effectiveness, it is actually not easy to conclude a monotonic trend that is applicable for all the cases in this experiment. Therefore, the discussion here is attempted to focus on M and exit Ma effect for the engine-like temperature condition (DR = 2.0).

From Figure 31(b) and Figure 35(c) for Ma = 0.7, it is observed that for the R1 region, the increasing M directly leads to higher effectiveness. This is due to the increasing coolant amount of carryover from LE. For the R2 region, the M effect is not prominent. Although the width of the coolant trace from SS1 shows an increasing then slightly decreasing trend due to the surface curvature, this indicates that the coolant is about to lift-off. But from the stronger contribution of LE carryover when increasing M, the difference of laterally averaged effectiveness in different M is limited. For the R3 region, the trend of M effect is essentially the same as the R2 region. Coolant lift-off when M = 1.6 is pretty

clear for the R3 region in the laterally averaged effectiveness. This is due to lacking the contribution from LE film like the R2 region.

From Figure 32(b) and Figure 35(c) for Ma = 1.1, the positive M effect for the R1 region is the same as low Ma; nonetheless, since the surface static pressure near LE is very high, the coolant carryover is very weak until the highest M. For the R2 region, the trend is still the same as with low Ma. R3 region is the part which exclusively gets affected by the oblique shock wave and demonstrates a totally different behavior compared to low Ma. As mentioned in the previous discussion, the altered surface pressure from shock wave seems to make the effectiveness decrease until the highest M, where the shock wave helps the coolant to adhere to the surface.

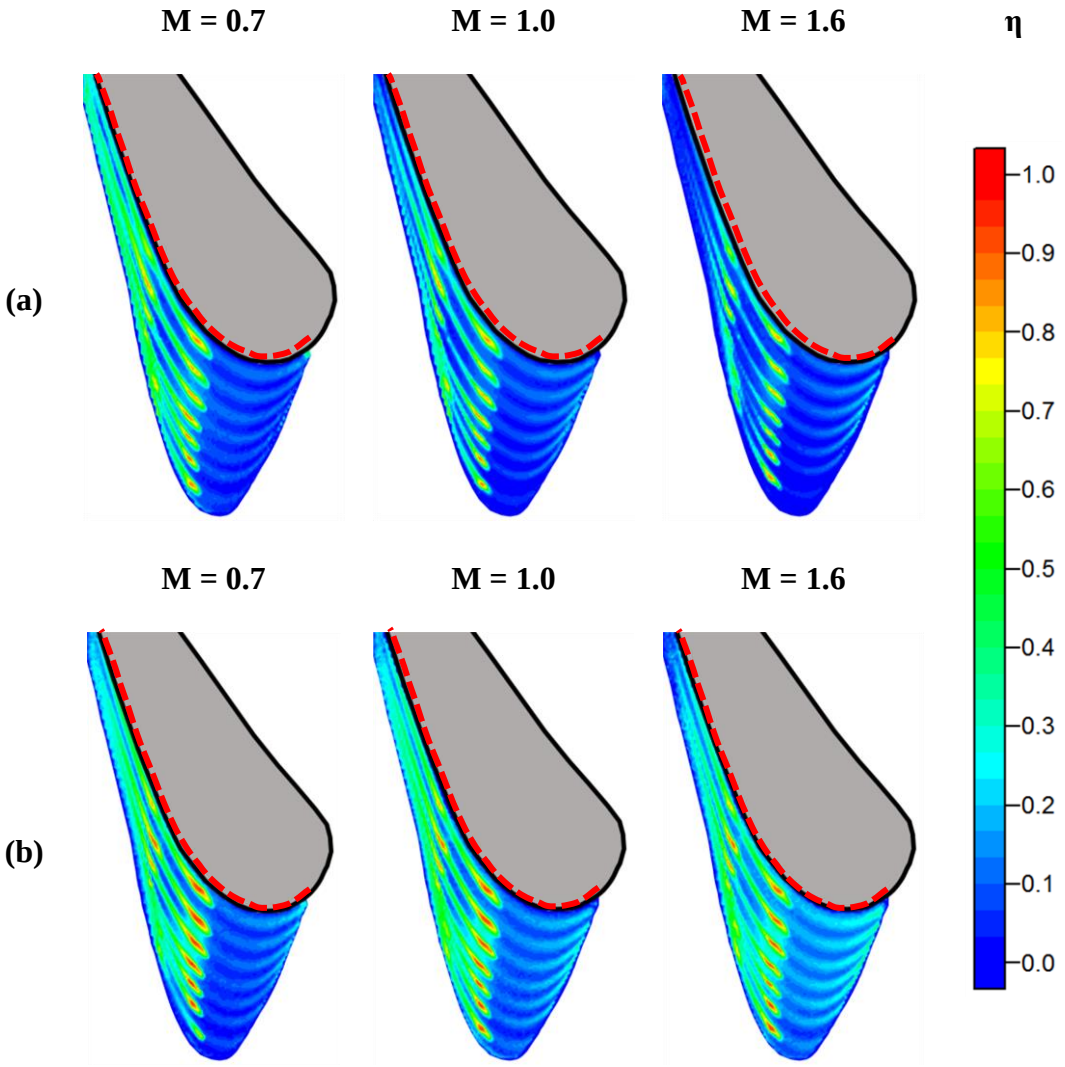

Figure 31. Film cooling effectiveness distribution on AOI for exit Ma = 0.7. (a) DR = 1.0; (b) DR = 2.0.

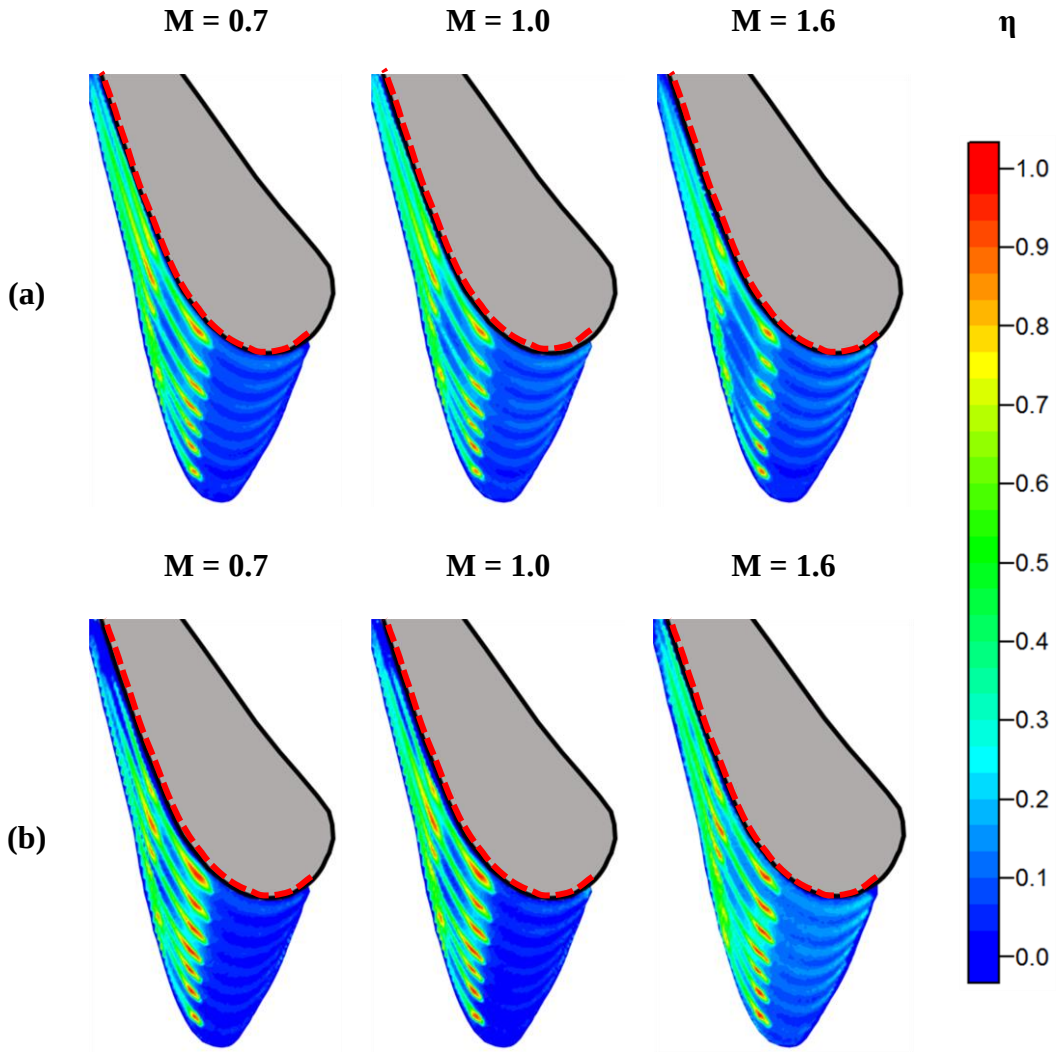

Figure 32. Film cooling effectiveness distribution on AOI for exit Ma = 1.1. (a) DR = 1.0; (b) DR = 2.0.

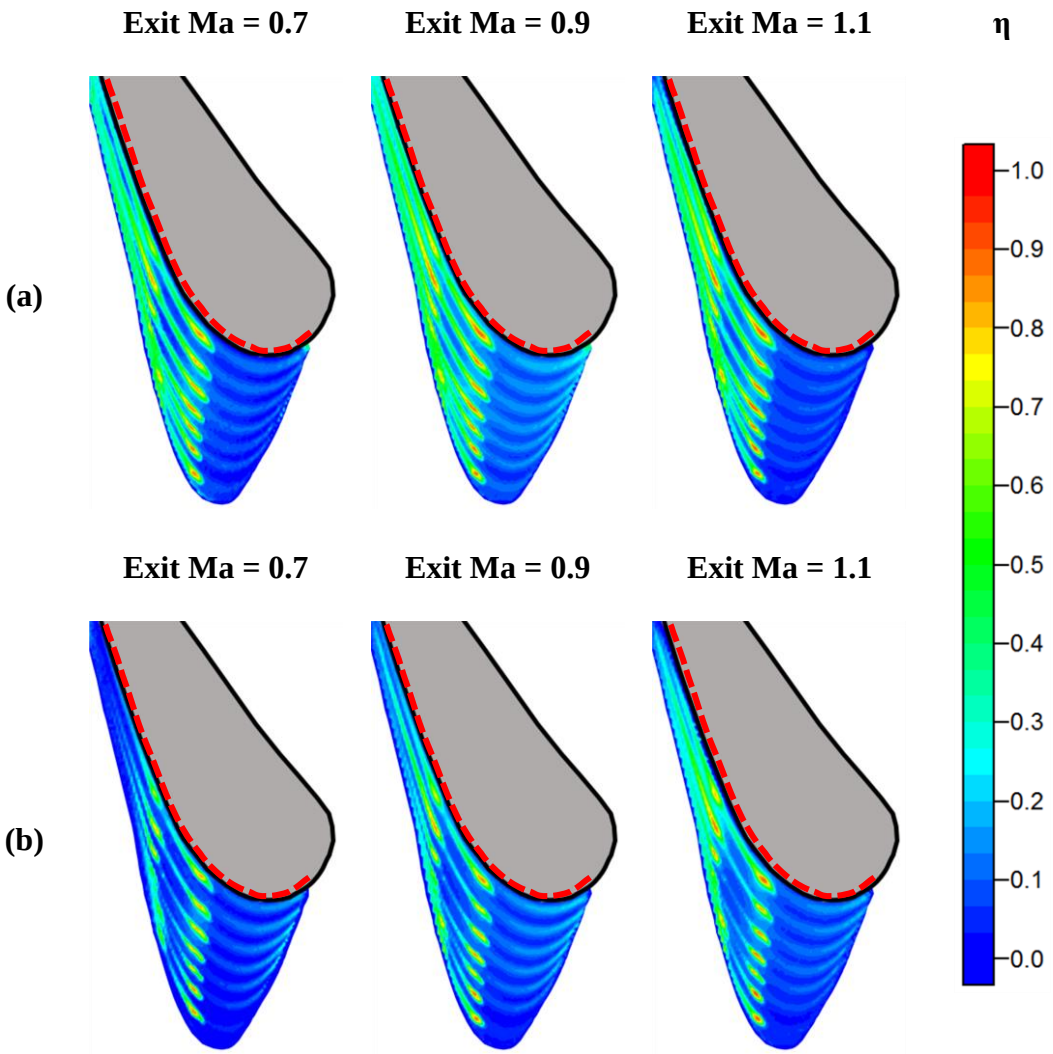

Figure 33. Film cooling effectiveness distribution on AOI for DR = 1.0. (a) M = 0.7; (b) M = 1.6.

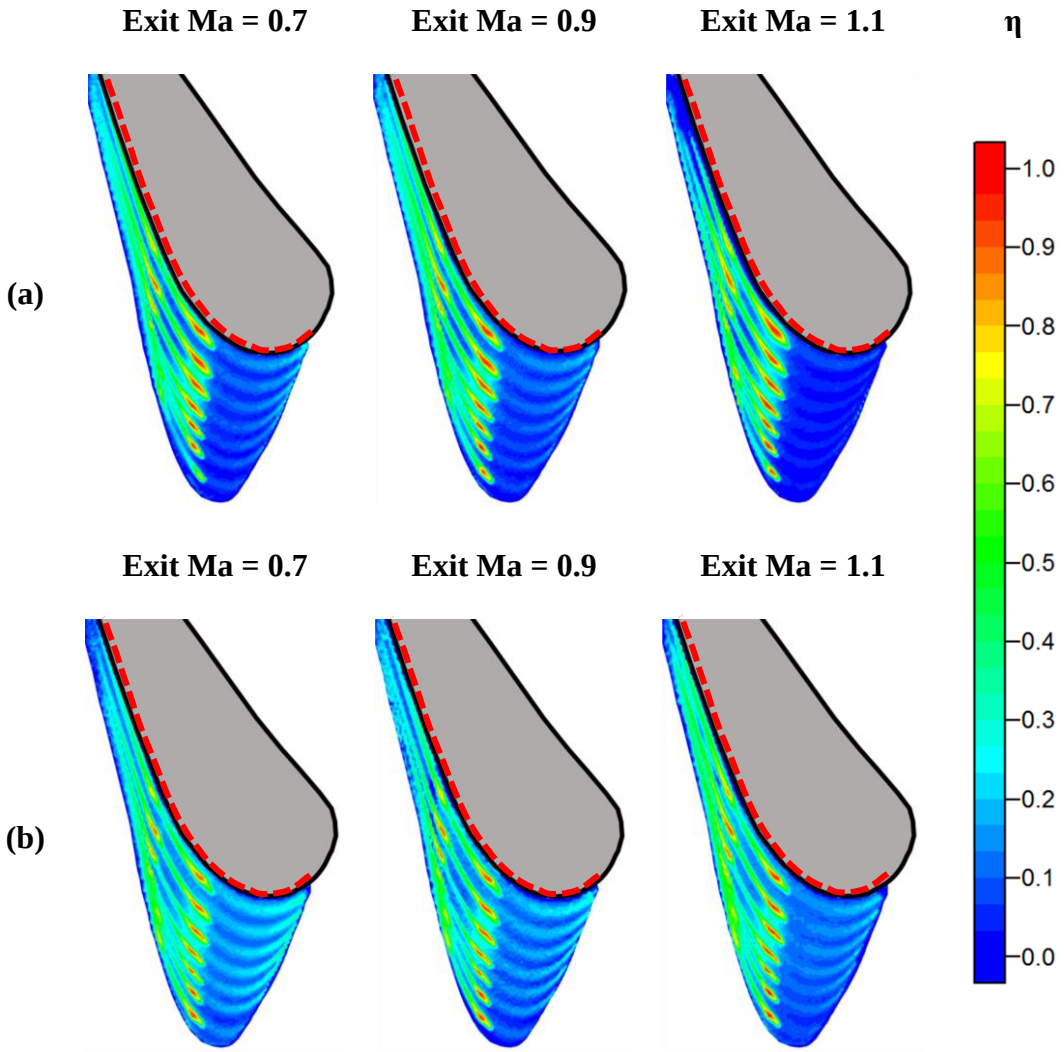

Figure 34. Film cooling effectiveness distribution on AOI for DR = 2.0. (a) M = 0.7; (b) M = 1.6.

(a)DR = 1.0

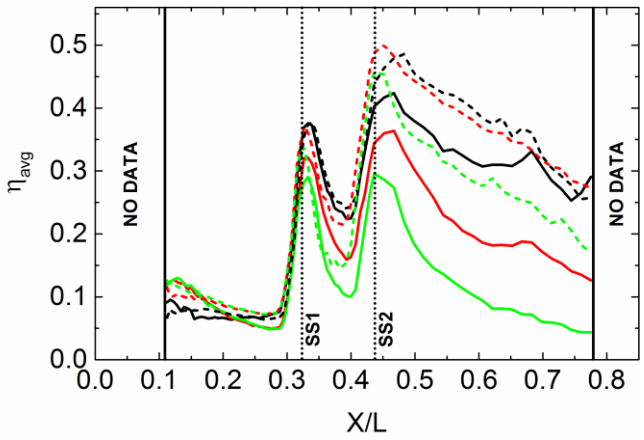

(b) DR = 1.5

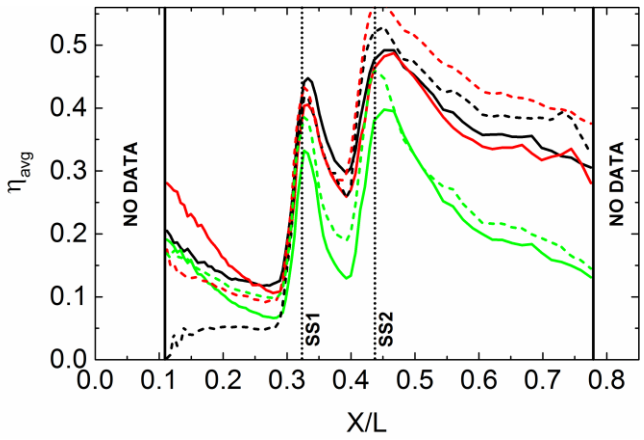

(c) DR = 2.0

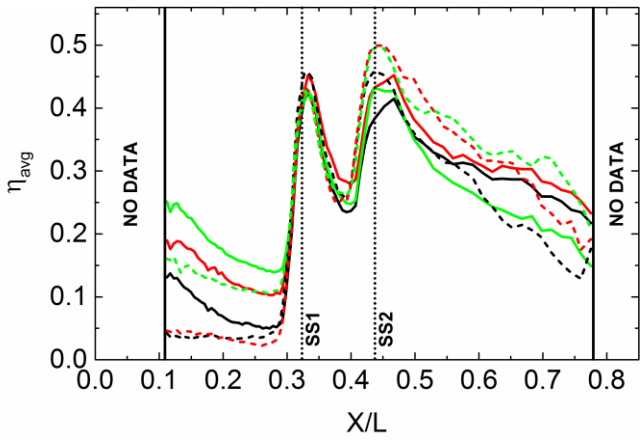

Ma = 0.7: M = 0.7 M = 1.0 M = 1.6
Ma = 1.1: M = 0.7 M = 1.0 M = 1.6

Figure 35. Laterally (spanwise) averaged effectiveness for M effect comparison.

(a) M = 0.7

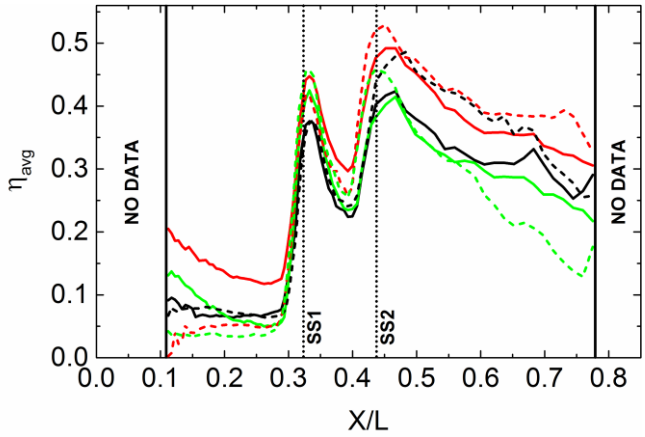

(b) M = 1.0

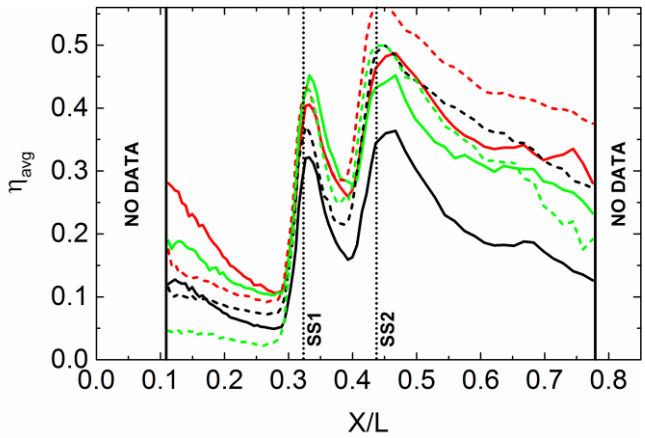

(c) M = 1.6

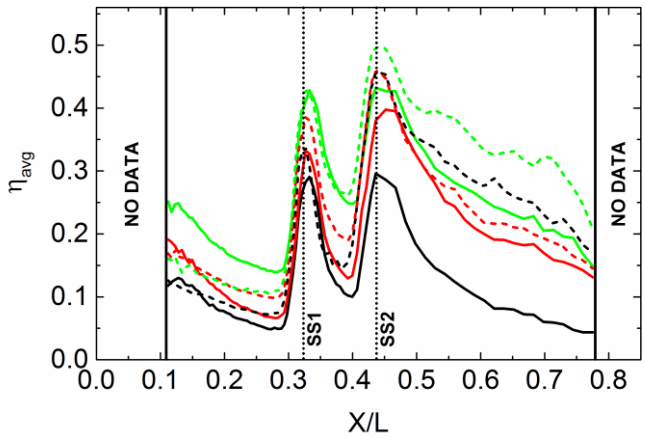

Ma = 0.7: DR = 1.0 DR = 1.5 DR = 2.0
Ma = 1.1: DR = 1.0 DR = 1.5 DR = 2.0

Figure 36. Laterally (spanwise) averaged effectiveness for DR effect comparison.

(a) M = 0.7

(b) M = 1.0

(c) M = 1.6

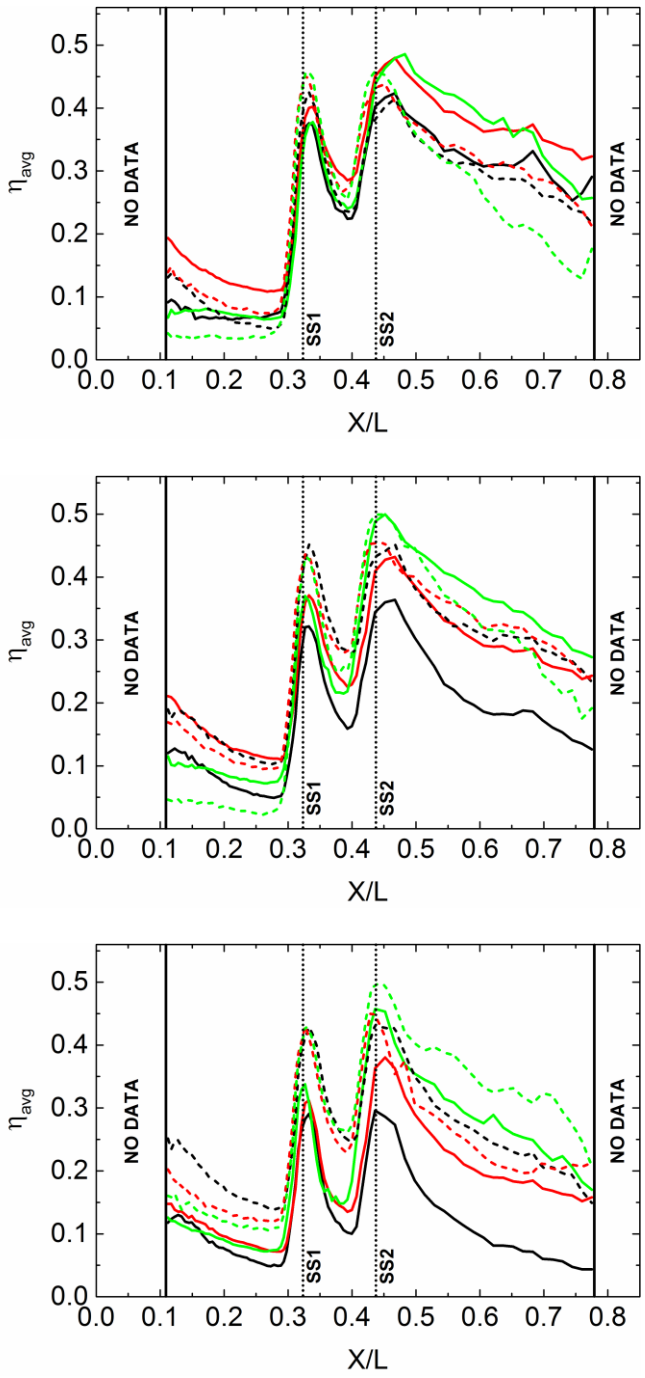

Figure 37. Laterally (spanwise) averaged effectiveness for exit Ma effect comparison.

5. TURBINE VANE ENDWALL FILM COOLING COMPARISON FROM DIFFERENT FILM-HOLE PATTERNS AND UPSTREAM LEAKAGE INJECTION ANGLES

5.1 Literature Review

Literature about the possible parameters that will affect the film cooling performance on either turbine endwall or vane/blade surface is selectively documented in Section 3.1 and 4.1. The literature survey here will focus more on the endwall film cooling accompanied with the introduction of upstream leakage and the injection angle effect that plays as an important variation factor in this study.

5.1.1 Endwall Film Cooling with Upstream Leakage

In real gas turbine engines, there is a gap/interface between the upstream part of the vane endwall and the combustor for the sake of assembly at the same time in consideration of the different thermal expansion from parts during operation. To prevent the hot gas ingestion, this gap is typically filled with pressurized coolant. This pressurized coolant, which referred as upstream leakage, not only can protect the frontal part of the endwall, but also has the potential to extend its coverage further into the passage depends on the particular design and the coolant momentum. Several studies are available in open literature describing the upstream leakage behavior on endwall film cooling by coolant injection using slots or cooling hole rows. Studies from Blair [22] and Granser and Schulenberg [67] reported that with the slot injection, the separation lines across the

channel move toward downstream, which means the secondary flow has been reduced due to the fact that upstream slot injection reduces the boundary layer thickness. Burd and Simon [68] concluded that the inclined-slot combustor bleed cooling flow imposes nearly no aerodynamic penalty. Besides, this type of cooling is capable to reduce secondary flow effect as the streamwise momentum from bleed flow thins the boundary layer and weakens the cross-stream flow. A parallel study by Burd et al. [69] pointed out this kind of bleed cooling upstream of the airfoil leading edge plane is able to provide considerable thermal protection within the passage. The coolant can spread to the entire endwall surface providing that coolant mass flow is increased. Oke et al. [70] studied the upstream include slot injection using one or two slots while keeping MFR constant. They conclude that due to the higher momentum flux ratio, the single slot has better uniformity of coolant distribution across the leading edge. To control the pitchwise coolant distribution from the upstream slot, Oke and Simon [71] studied the slots variations that are partially blocked to re-distribute the coolant by utilizing secondary flow. In general, they found that when momentum flux ratios are low, coolant migrates toward the suction side due to secondary flow. For higher ratios, the pressure side endwall region is protected more effectively.

In addition to the slot, cooling hole rows are adopted in lab testing in lieu of controlling the upstream leakage of the vane/blade endwall. By providing a more uniform coolant coverage with the merging of neighbor coolant traces, studies using two rows of staggered cooling hole are available in open literature. Oke at al. [72] found that although there is higher mixing accompanied with discrete holes than with full-slot injection, nearly no suction side coolant migration is seen compared with the slot injection when the coolant

flow rate is increased due to elevated momentum. Zhang and Jaiswal [73] compared the endwall film cooling from upstream injection from double-row hole injection with a single-row discrete slot injection. Their results indicated that uniform effectiveness distribution can be achieved using discrete slot injection for higher MFR, while higher effectiveness near the trailing edge can be obtained using injection from double- row of staggered hole. Liu et al. [74] studied the upstream injection using either one or two rows of hole. They found that while double row injection is always better than a single row in terms of averaged effectiveness, to improve the coolant coverage near the pressure side is not possible by simply increasing the coolant amount if the blowing ratio is low. Knost and Thole [75] studied the endwall film cooling combining both coolant from a flush slot and film cooling from two distinct hole patterns. They found that with slot and film cooling flows present, there was a large region in the center of the inlet to the passage that was overcooled. Also, the momentum flux ratios were shown to have a significant impact on cooling performance. Zhang et al. [76] investigated the optimal hole diameter for upstream injection using two rows of staggered cooling hole and found the optimized diameter/blowing ratio based on their particular design. Further, a complete information about film cooling effectiveness variation under different coolant-to-mainstream conditions on various endwall film-hole patterns when upstream leakage is realized by two rows of staggered cooling hole documented by Chowdhury et al. [77-79]. In general, higher blowing ratio is the key for better effectiveness. This is because coolant with lower momentum could not survive in the endwall secondary flows, resulting in poor film

coverage; when the coolant momentum is sufficiently high, the jets could counteract with the secondary flow and result in acceptable film effectiveness.

5.1.2 Effect of Injection Angle

As large injection angle is rarely used on turbine vane/blade except on the leading edge portion, compared with other parameters, the studies focus on the different injection angle of the cooling hole is relatively scarce in the open literature. The majority of the studies is based on 30^o or 35^o injection angle, moreover, the few large injection angle studies were conducted on flat plate test facility. Foster and Lampard [80] studied effectiveness variation for three different injection angles (35^o, 55^o, 90^o) of a row of cylindrical holes. They concluded that shallow injection angle gives the highest spanwise averaged effectiveness at small blowing rates and large injection angle performs better at high blowing rates. They also found that large injection angle produces more uniform cross-stream (spanwise) distribution of effectiveness. However, an investigation from Kohli and Bogard [81] indicated that for 35^o and 55^o injection angle, large angle holes offered similar lateral performance to their small angle counterparts when the momentum flux ratio is low. However, as the momentum flux ratio increases, the effectiveness of large angle holes decreases more rapidly than small angle holes. In a later study, Kohli and Bogard [82] showed that the cooling performance with shaped holes with large injection angle was even superior with the cylindrical holes with the typical 35^o injection angle. Baldauf et al. [83] conducted film cooling measurements on a row of cylindrical holes with injection angles ranging from 30^o, 60^o, and 90^o in a flat plate test section. They

concluded that the coolant is driven away from the wall because of higher surface normal momentum in larger injection angles. The jet trajectory is higher and coolant to hot gas interaction is intensified, both having an adverse influence on the effectiveness. Yuen and Martinez-Botas [84,85] also conducted film cooling characteristics studies with same injection angles (30^o, 60^o, and 90^o) in a flat plate wind tunnel. Their results indicated that the effectiveness decrease from shallow to steep injection angle is not monotonic. The effectiveness variation actually depends on the streamwise location with respect to the hole exit (near-hole, intermediate, or far downstream).

5.2 Experimental Setup and Method

5.2.1 Four-Passage Linear Cascade

The measurements were conducted in a four-passage linear cascade as shown in Figure 38. From Figure 39, the majority of the cascade is made by aluminum through machining. The area of interest, the center endwall is a removable part and made by SLA process using a material called Accura® Xtreme™ White 200. In addition, the upstream leakage plate is also a removable part. A portion of the top cover is equipped with a transparent Plexiglas window to ensure the optical access to the AOI. The mainstream air of this cascade is supplied by a blowdown facility including a 325 psi high-pressure compressor, a dryer, and a storage reservoir. The mainstream is regulated by an electronic controller that controls the diaphragm actuator through digital positioner using the feedback signal from the pressure transducer in the wind tunnel.

The inlet and exit velocities were continuously monitored by recording total and static pressure values using Pitot-static probes, which were stationed at 0.5 C_{ax} upstream of the vane's LE and TE planes. The mainstream temperature was also monitored by a T-type thermocouple. To simulate the turbulence flow approaching the turbine vane, a bar-type turbulence grid with bar width 1.27 cm and 48% porosity, located at 2.72 C_{ax} upstream of vane's LE plane was used. The corresponding turbulence intensity (Tu) is 19% with an integral length scale around 1.7 cm at 0.5 C_{ax} upstream of vanes' LE plane. Detailed information about the cascade geometry and turbulence measurement are listed and described in [42]. Two LED excitation lights and a monochrome CCD camera was used for measuring PSP emission intensity for film cooling effectiveness calculation under different test conditions.

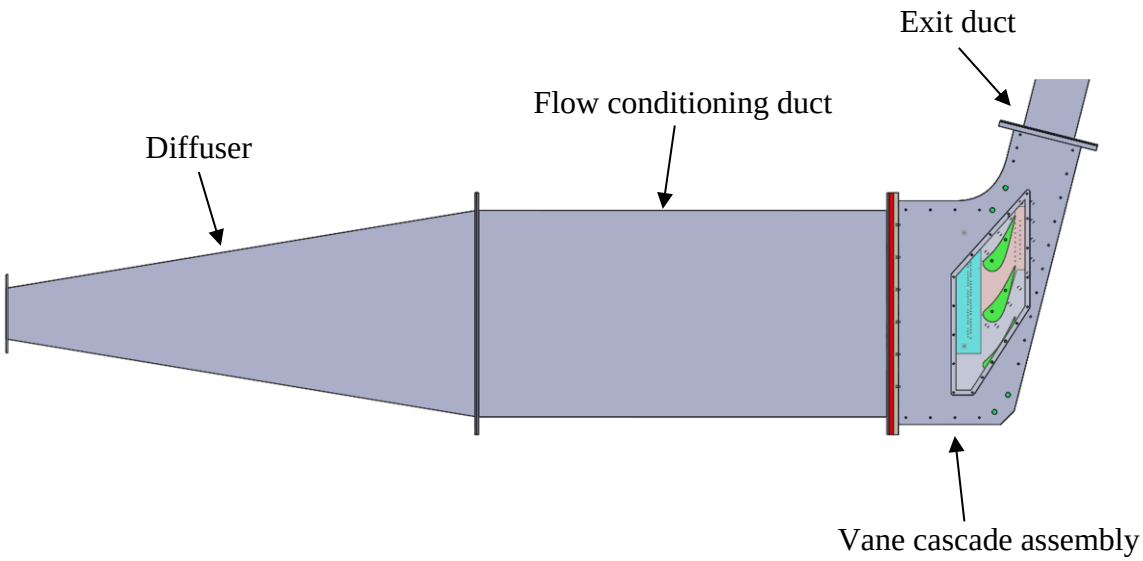

Figure 38. Flow loop for the test section and facility.

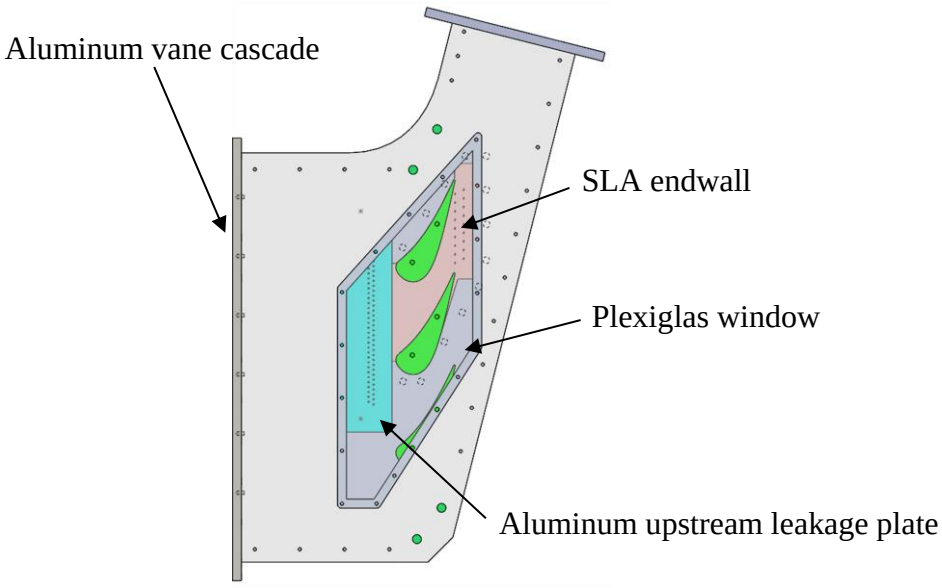

Figure 39. Schematic view of the vane cascade assembly.

5.2.2 Film Cooling System

The film cooling system consists of the upstream leakage and the endwall film cooling in the passage. The schematic of test section including upstream leakage holes and one of the representative endwall film cooling designs is shown in Figure 40. Two rows of staggered cylindrical holes covered middle and two half neighbor passages are used to simulate the leakage flow from the interface between the combustor and the first stage vane. There are total 75 holes (37 holes for 1st row, 38 holes for 2nd row) in these two rows with the diameter (d) of the cooling hole around 0.175 cm and the spacing between rows and neighbor holes are fixed to be 4d. The 2nd row is located on 0.38 C_{ax} upstream of the vane's LE plane. Three different injection angles of the upstream leakage hole (shown in Figure 41) can be achieved by changing the removable upstream plate. It is noted that due to the existing plenum design, the 2nd row of 50^{o} injection angle upstream plate is located

on 0.4 C_{ax} upstream of the vane's LE plane. For the film-hole pattern on the endwall, there are five removable endwall plates with different cooling hole design (shown in Figure 42). Each design has 18 cylindrical holes distributed on the endwall. The surface angle of all cylindrical holes is fixed to be 30^{o}. There are two plenums, one supplied the upstream leakage holes (two rows), the other supplied the holes inside the endwall passage (18 holes). The coolant source is either the dry air from the compressor loop or the compressed CO_2 (DR = 1.52 ≈ 1.5) cylinder as foreign gas. The coolant volume flow rate from each plenum is controlled by individual rotameter, the reading is adjusted with the specific gravity correction when flowing foreign gas and applied density correction from the pressure tap reading at the rotameter exit.

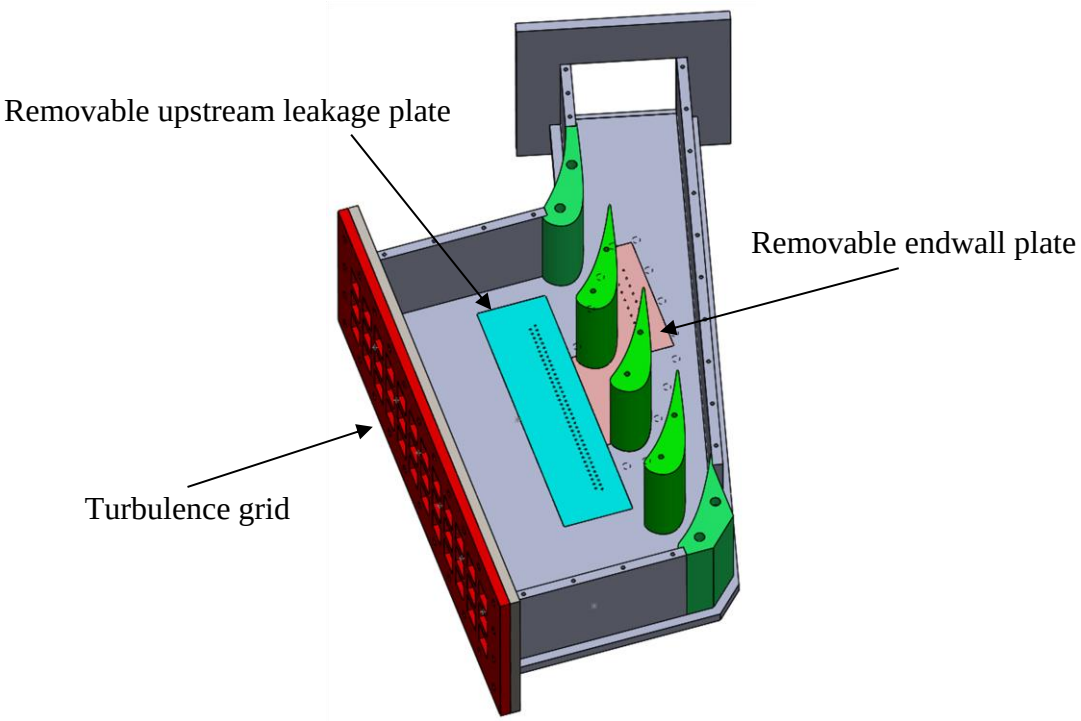

Figure 40. Schematic of the endwall test section.

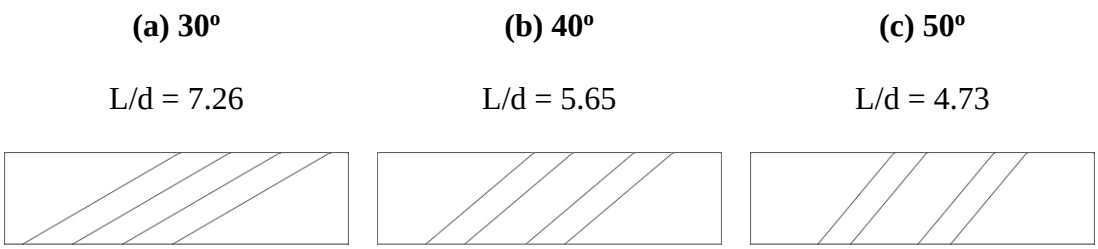

Figure 41. Schematic of different injection angle for two-row upstream leakage.

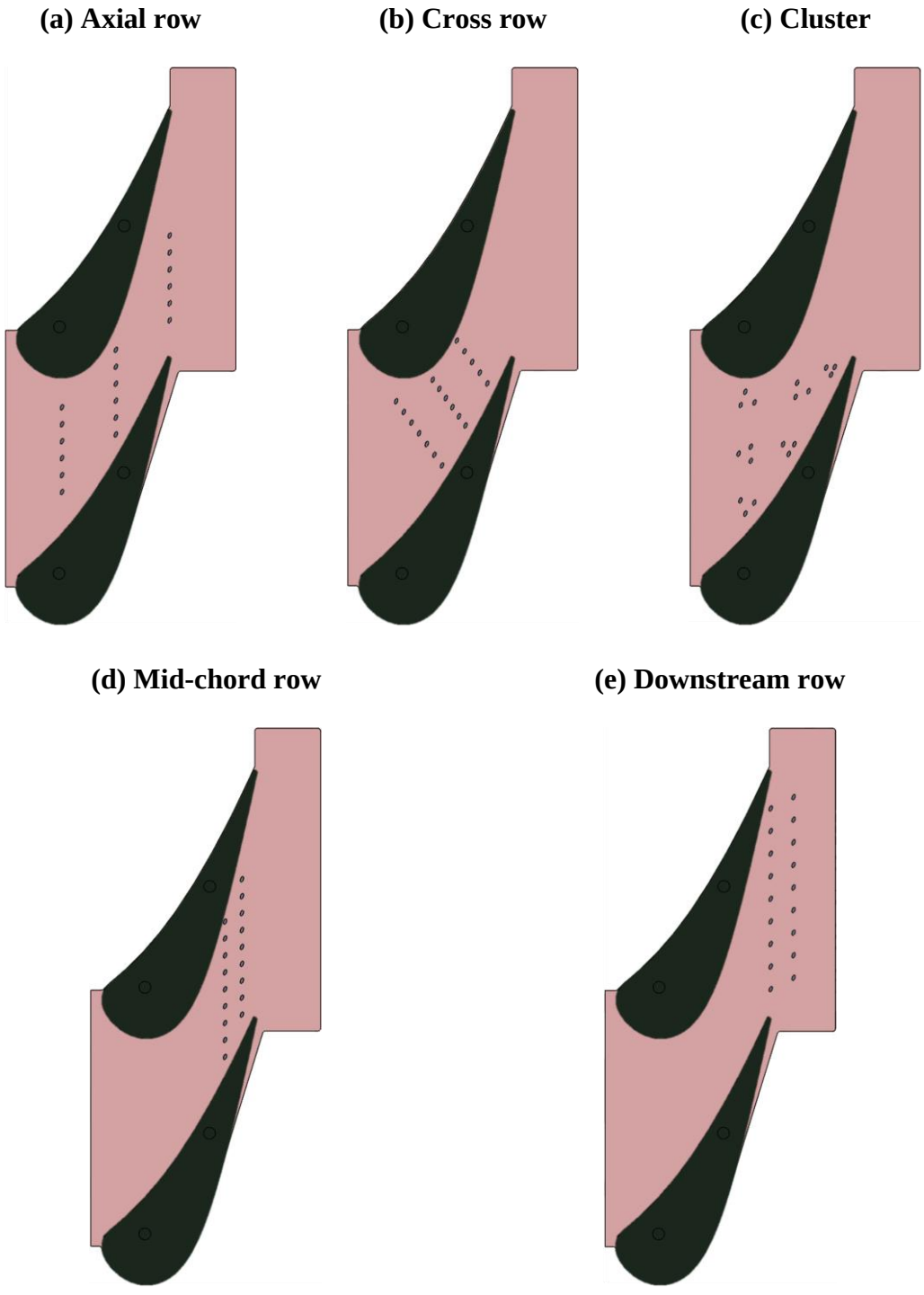

Figure 42. Schematic of film-hole patterns on endwall.

5.2.3 Experimental Method – Pressure-Sensitive Paint

The same experiment method and data acquisition setup are applied to this study. Different from the previous two studies, there were two LED lights simultaneously used in this study to achieve a better illumination on AOI. Detailed information can refer to either Section 3.2.3 or Section 4.2.3.

5.3 Test Matrix

Fifteen sets of experiment consist of three upstream leakage angles and five endwall film-hole pattern designs were conducted to study the endwall film cooling effectiveness under fixed mainstream (inlet Ma_{is} = 0.1, exit Ma_{is} = 0.5) and coolant condition (MFR = 1% for the upstream leakage and endwall plenum, respectively). Figure 43 is the exit Mach number history to demonstrate that steady flow is maintained for around 15 seconds. Since the endwall experienced surface temperature change from aerodynamic heating due to the high freestream velocity (compressible flow). The recovery temperature on the endwall varies locally according to surface Mach number distribution and it can be calculated using Eq. (4) mentioned in Section 4.3. The maximum temperature difference between the calculated recovery and freestream is around 1.1 ^{o}C at exit Ma = 0.5. Although the flow-induced temperature distribution is not reproducible in the reference condition (without flow), the corresponding deviation on intensity is found to be negligible according to the temperature sensitivity suggested by PSP manufacturer. Summary of the test matrix is shown in Table 3.

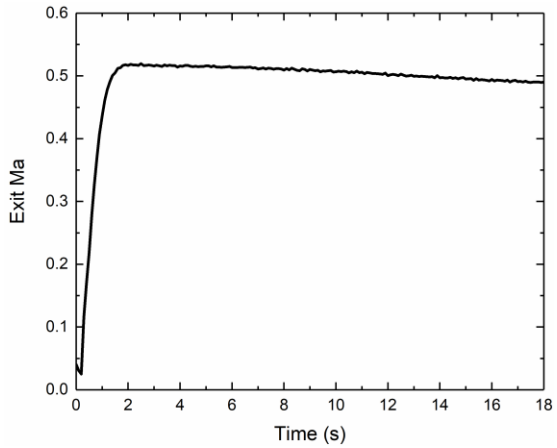

Figure 43. Exit Mach history for the current test section.

Table 3. Summary of the test matrix for the vane endwall film cooling study with upstream leakage.

Experiment no.	Film-hole pattern	Upstream leakage angle
1-3	Axial row	30º, 40º, 50º
4-6	Cross row	30º, 40º, 50º
7-9	Cluster	30º, 40º, 50º
10-12	Mid-chord row	30º, 40º, 50º
13-15	Downstream row	30º, 40º, 50º

5.4 Experimental Uncertainty

The uncertainty of the measurement in this experiment comes from the fluctuation of mainstream velocity (±2%), the fluctuation of coolant flow rate (±2%), and the thermocouple reading (±0.5℃). For the film cooling effectiveness calculation, the major uncertainty is the variation of PSP emission intensity value captured by the camera. Multiple reference and black images were first taken to quantify the intensity fluctuation.

By the method proposed by Kline and McClintock [46] based on a 95% confidence level, the uncertainty of film cooling effectiveness deduced from the calibration curve at $\eta = 0.1$, 0.3, 0.5 and 0.7 are 15%, 3.9%, 1.7% and 0.7%, respectively in the present study.

5.5 Results and Discussion

5.5.1 Upstream Injection Angle Effect

The adiabatic film cooling effectiveness contours for three different injection angles on five different endwall film-hole patterns are shown in Figure 44, 45, 47, 49, and 51. As a fixed coolant flow rate is used for all the tests in this study, the coolant momentum from the upstream leakage is considered identical regardless of the injection angle. In terms of flow physics, for a hole with an inclined injection angle, the coolant momentum can be decomposed into the streamwise and vertical components. When the incline angle increases, the streamwise component will be reduced in exchange for the increased vertical component. When using large injection angle, the streamwise coolant coverage is inherently weak due to the insufficient streamwise coolant momentum. Further, the strong vertical coolant momentum is prone to mix with the mainstream and being diffused, which essentially makes no contribution to film coverage on the surface. This is the reason that under a fixed coolant amount, a shallow injection angle, in general, has a better cooling performance. So, when we focus on the region in the proximity of the two-row upstream leakage, the film cooling effectiveness systematically decrease as we increase the injection angle from 30^o to 50^o, as shown in Figure 44, 45, 47, 49, and 51. This phenomenon is

evident whether referring to the contours or the laterally averaged effectiveness as shown in Figure 45, 46, 48, 50, and 52.

When the focus is inside the endwall passage, the interaction between the upstream leakage, secondary flows (horseshoe vortices, passage vortex, and corner vortices), inherent pressure gradient, and the film-hole pattern on the passage becomes very important. It is already a consensus that the coolant from upstream leakage can reduce the strength of the secondary flow (e.g. horseshoe vortices), so the cooling hole performance located near the vane's LE is expected to be enhanced. Second, if the coolant pretty much adheres to the surface, this film from the upstream would accumulate and reduce the local static pressure near the downstream cooling hole. This will slightly increase the pressure difference (driving force) of the cooling hole and lead to larger discharge coefficient. Based on the above two reasons, we can conclude that the if the cooling holes inside the passage are closer to the upstream, then their performance will be highly affected by the upstream leakage. Further, it is found that when injection angle is 30^{o} for this particular upstream design, the leakage film can nearly propagate to the full passage providing that there is no coolant injection from the film-hole pattern on the endwall passage [77], so it is expected that the cooling performance of holes on endwall will all be affected by either first or second factor or even both.

For the axial row configuration, we can see the coolant traces from 1^{st} row readily shrink when the injection angle increases to 40^{o}. Considering the visible pressure leg of the horseshoe vortex in Figure 44(b), this performance reduction can be attributed to the resultant effect from both less-suppressed horseshoe vortex and less coolant accumulation

from leakage. The declined performance of the 2nd row also came from the less accumulation from the both the leakage and the 1st row, with the additional effect of the presence of pressure side corner vortices. There is low effectiveness gap between 2nd and 3rd row, we can thus conclude that the cooling performance decrease for the 3rd row is mainly due to weak film accumulation from leakage. Without the contribution of upstream leakage, the coolant from 2nd row can barely make it to the 3rd row. It is also found that the nozzle wake portion becomes less-protected. From Figure 44(c), when the injection angle further increases to 50°, the aforementioned phenomena still hold as the performance of 1st row drops accordingly. However, the cooling performance decay from the 2nd and 3rd rows are minor although the unprotected wake region seems to be slightly enlarged. As 2nd and 3rd rows are located in X/C_{ax} = 0.65 and 1.0, the film accumulation from 40° injection angle upstream is already slim, local coolant coverages thus have only negligible change when a further reduction in upstream accumulation. Figure 45 is the spanwise averaged effectiveness for the axial row design. The 30° injection angle has the best laterally averaged effectiveness all over the AOI, for the 40° angle, the effectiveness uniformly decreases compared with 30° up to 2nd row, the effectiveness difference then gradually shrinks. For the 50° degree angle case, the averaged effectiveness from upstream leakage further reduces and merges with the 40° angle case at 1st row. After that, the averaged effectiveness from 40° and 50° cases are nearly indistinguishable.

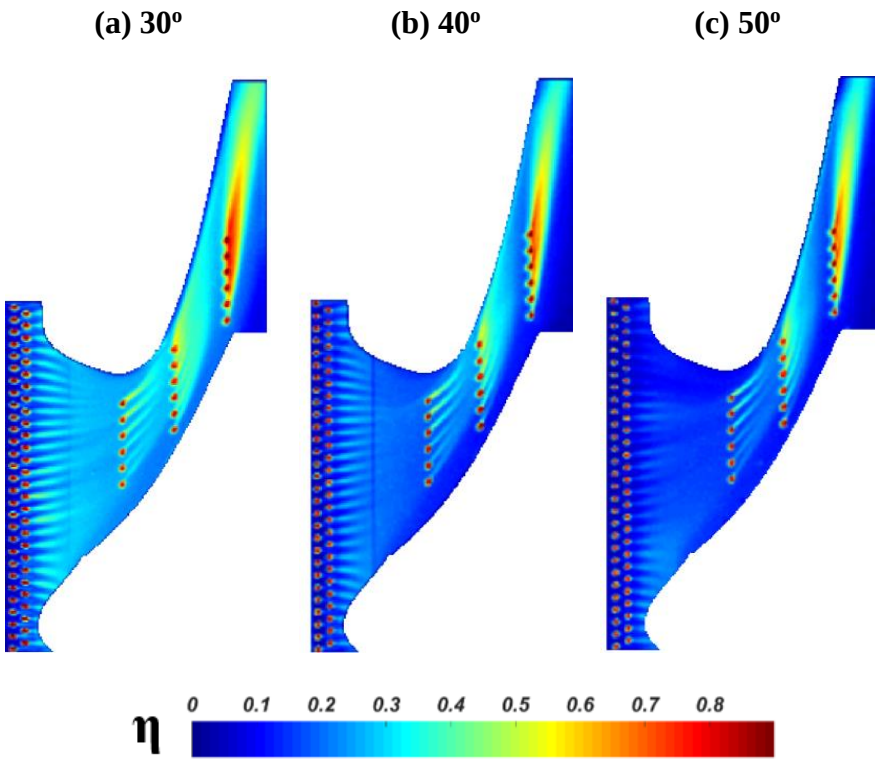

Figure 44. Film cooling effectiveness of axial row configuration under different upstream leakage injection angle.

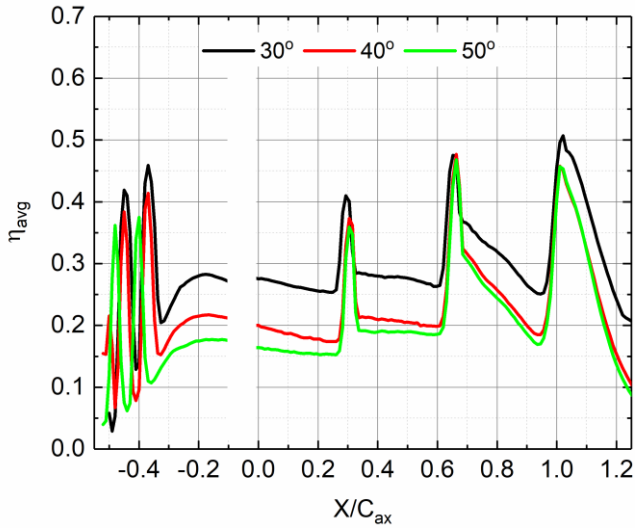

Figure 45. Laterally (spanwise) averaged film cooling effectiveness of axial row configuration under different upstream leakage angle.

For the cross row configuration, the cooling performance of 1st row is highly reduced due to the similar reason as axial row including the stronger pressure leg of horseshoe vortex and the weaker upstream accumulation when upstream injection angle is 40o as shown in Figure 46(b). One thing that worthy to mention is that for this design, the spacing between cooling hole rows are smaller, which means the film from upstream rows will most likely to accumulate to the downstream row. For the 2nd row, the declined coolant can be explained by the weak film from both upstream leakage and the 1st row. For the 3rd row, the effectiveness behavior is mainly from the contribution of 2nd row. As the case in the axial row, the nozzle wake region becomes non-protected in this injection angle. Interestingly, when the injection angle is 50o as shown in Figure 46(c), in addition to the 1st row, which is closer to the upstream leakage, the effectiveness from 2nd and 3rd further drop simultaneously, which is a different behavior compared with the axial row. It is possible that under the same coolant flow rate from the upstream and inside the endwall passage, each endwall film-hole pattern has its unique flow/pressure distribution. This unique local flow field will influence how far the upstream leakage can affect the entire endwall passage, by contributing a better hole performance located closer to the leakage and therefore a stronger contribution to film accumulation toward downstream holes. Figure 47 is the spanwise averaged effectiveness for the cross row design. The 30o angle one has the best laterally averaged effectiveness as expected. But the effectiveness drops systematically when the injection angle increases, which is attributable to weaken coolant coverage from the feeble upstream leakage and the resulting deficient film accumulation from upstream row to downstream row.

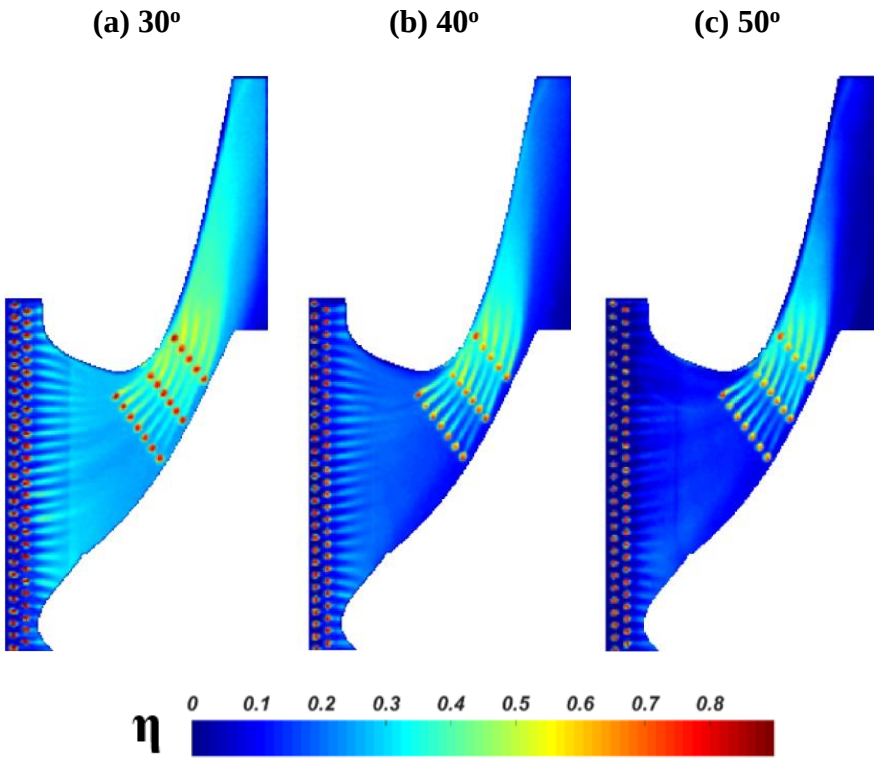

Figure 46. Film cooling effectiveness of cross row configuration under different upstream leakage injection angle.

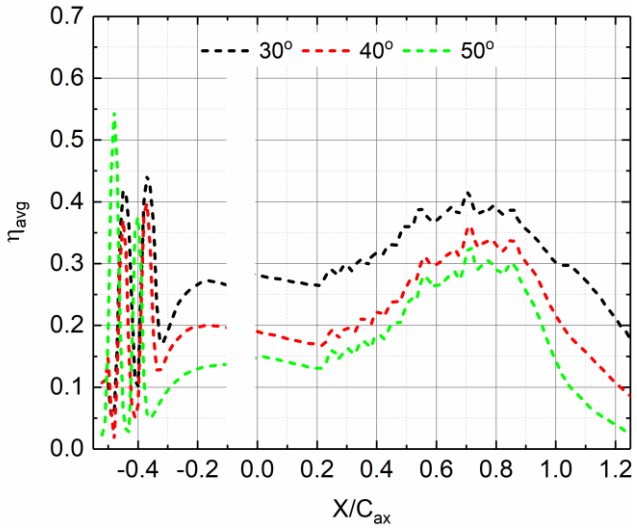

Figure 47. Laterally (spanwise) averaged film cooling effectiveness of cross row configuration under different upstream leakage injection angle.

For the cluster configuration, in order to have an easy identification of hole groups, the terminology can refer from [79]. Due to the fact that the first three groups (G1 to G3) of cluster holes are located at the similar location (X/C_{ax} = 0.3) as the 1st row of axial row configuration, the coolant behavior when increasing the injection angle to 40° is found to be similar to the reason described before. From Figure 48(b), we can see that the film from G4 and G5 also decrease, however, it is clear that the performance of these two clusters is still being weakly contributed by G1 and G2, respectively. Therefore, their performance is still influenced by the reduced accumulation from G1, G2, and the upstream leakage. The worse performance of G6 mainly comes from the low upstream leakage film as well as G5, as the accumulation contributed by G4 is limited. When the injection angle is 50° as shown in Figure 48(c), a significant film coverage drop is observed for G1 to G4, which are the clusters located within around X/C_{ax} = 0.55. Nonetheless, the coolant coverage decrease seems to be mild for G5 and minor for G6 compared with the 40° angle case. It is a direct evidence that for this cluster design when the leakage injection angle is larger than 40°, the leakage film is not able to penetrate farther than X/C_{ax} = 0.85. Figure 49 is the spanwise averaged effectiveness for the cluster design. Regardless of the best performance when upstream injection angle is 30°, the laterally averaged effectiveness of injection angle 40° demonstrates a nearly constant effectiveness drop up to X/C_{ax} = 0.8, the difference is getting smaller further downstream. The same trend is observed when injection angle is 50°, which is apparent that after this particular location, the upstream leakage film is unable to affect the local cooling holes' performance.

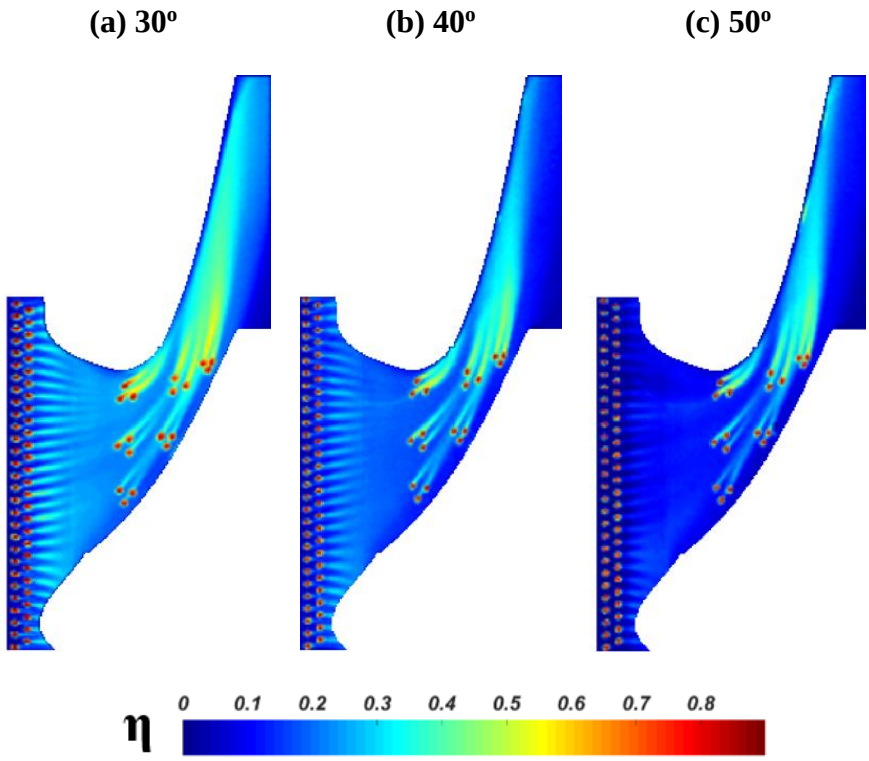

Figure 48. Film cooling effectiveness of cluster configuration under different upstream leakage injection angle.

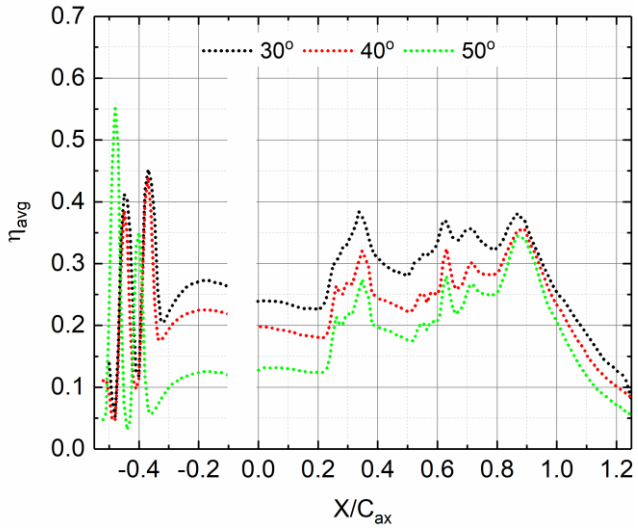

Figure 49. Laterally (spanwise) averaged film cooling effectiveness of cluster configuration under different upstream leakage injection angle.

For the mid-chord and downstream row configurations, different from the previous three designs, these two film-hole patterns are mainly to tackle the endwall region which has higher heat transfer coefficients due to the higher near-wall velocity (from close to the throat to vane's TE). As the cooling hole rows in these designs are both located at least after $X/C_{ax} = 0.8$, the cooling hole performance for both designs is considered to be less affected by the injection angle variation of the upstream leakage in this study. For the mid-chord design as shown in Figure 50, since there is no cooling hole within the majority of the endwall passage, most of the endwall passage coolant is directly from the upstream leakage. A monotonical effectiveness drop is observed when increasing the upstream injection angle. For the two rows of cooling hole, it is found that the cooling hole performance has no visible difference when varying the upstream injection angle. The only observable distinction could be the nozzle wake region very near the suction side. For the cooling hole arrangement like this mid-chord design, we can thus conclude that only if the leakage film could be further intensified, otherwise, the performance of endwall cooling hole is independent of the upstream leakage angle. Figure 51 is the spanwise averaged effectiveness of the mid-chord row design. The trend is basically consistent with our observation in contour plots. The effectiveness is decreasing when the injection angle of upstream leakage increases from 30^o to 50^o. For the endwall cooling hole portion, the difference in averaged effectiveness under different upstream injection angle is negligible.

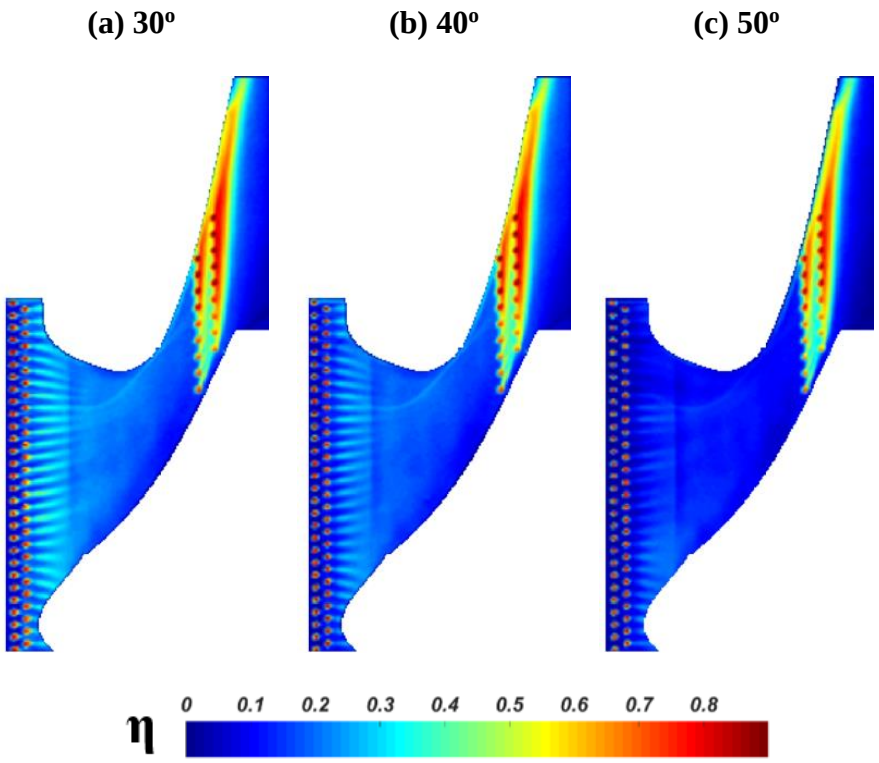

Figure 50. Film cooling effectiveness of mid-chord row configuration under different upstream leakage injection angle.

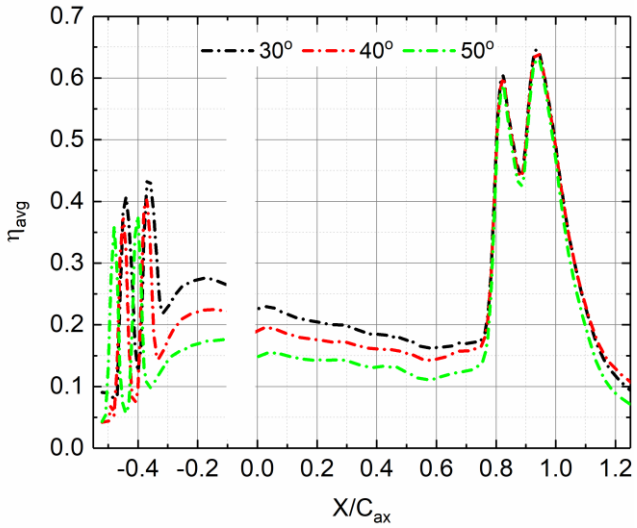

Figure 51. Laterally (spanwise) averaged film cooling effectiveness of mid-chord row configuration under different upstream leakage injection angle.

For the downstream row design, as the cooling hole rows are located further downstream (after X/C_{ax} = 1.0), the scenario should be similar to the mid-chord row. Which represents the monotonically decreasing effectiveness for the majority of the endwall passage accompanied by the nearly invariant performance of the two cooling hole rows. This is the case showed in Figure 52 as expected. Since the coolant momentum from upstream leakage is considered weak when propagated so far, the coolant traces from two downstream rows under different upstream injection angle is found to be pretty close. The tiny visible dissimilarity in effectiveness value falls into the inherent uncertainty between run-to-run. Figure 53 is the spanwise averaged effectiveness of the downstream row design. It is found that although the averaged effectiveness when upstream injection angle is 30^o constantly performs superior till the hole rows, the accumulation does not add up afterward. For the steeper upstream angles, the averaged effectiveness difference between 40^o and 50^o injection angle is difficult to detect as early as X/C_{ax} = 0.5. The reason could be that when injection angle is as steep as at least 40^o, the film from leakage is pretty lame due to low streamwise momentum, once it penetrates inside the passage, it decays pretty fast when it exposes under the strong effect of passage vortex and corner vortices from both pressure side and suction side.

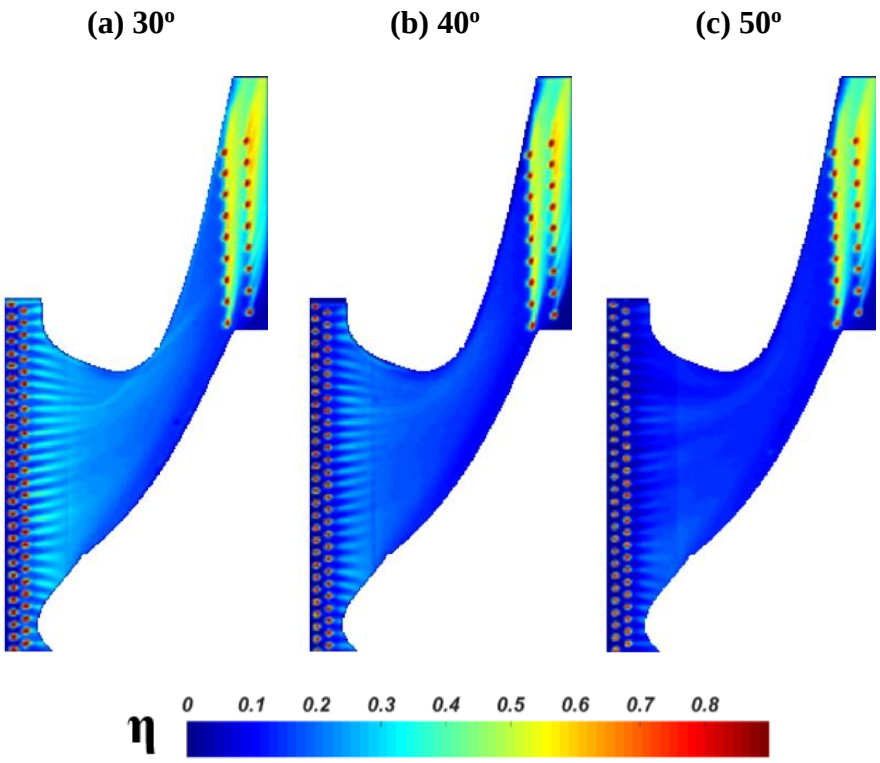

Figure 52. Film cooling effectiveness of downstream row configuration under different upstream leakage injection angle.

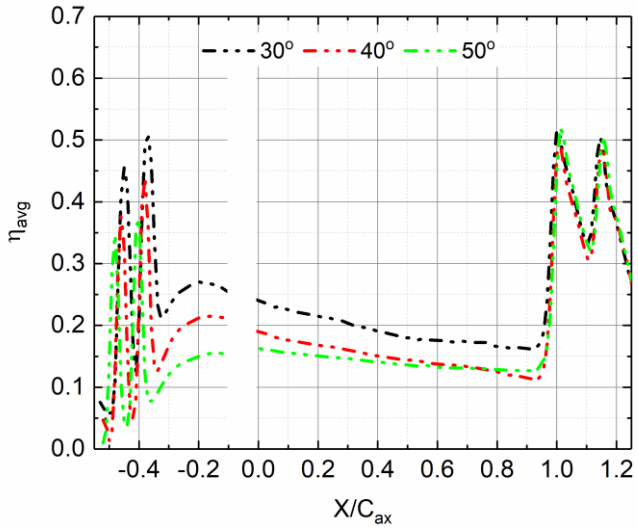

Figure 53. Laterally (spanwise) averaged film cooling effectiveness of downstream row configuration under different upstream leakage injection angle.

5.5.2 Design Comparison

The spanwise average effectiveness data for all the endwall film-hole patterns in different upstream injection angles are consolidated in Figure 54-55. For a given upstream injection angle, it is obvious that although the coolant amount from both leakage and endwall film-hole are kept the same, the different effectiveness distribution of each particular design is due to the distinctive hole arrangement on the endwall. For a more intuitive design comparison among all 15 cases in this study, the area-averaged effectiveness is also presented in Figure 57. When upstream injection angle is 30^o, it is found that from Figure 44(a) and Figure 46(a) that the axial row and cross row configuration are comparable but cross row provides a more uniform coolant coverage in the AOI. The cluster configuration also has uniform film coverage but relatively inferior protection after TE as shown in Figure 48(a). From Figure 50(a) and Figure 52(a), the effectiveness of mid-chord and downstream configurations are concentrated after X/C_{ax} = 0.8, and these intense local film coverages cannot remedy the deficit of the frontal part of the endwall passage. One point that is worthy of mentioning is that the laterally averaged effectiveness from the downstream configuration does not drop to between 0.1 and 0.2 as other four configurations do. It is due to the fact that the coolant traces do extend out of the AOI for downstream row configuration as shown in Figure 52. When the upstream injection angle is 40^o, it is found that the axial row, cross row and cluster configuration are all capable to sustain effectiveness value at least 0.2 within the most of the passage. Although the cross row configuration and cluster still achieve a uniform averaged effectiveness, the downstream protection of cross row drops to the similar level as the

cluster. Since the laterally averaged effectiveness from the configurations with cooling hole closer to the upstream leakage is highly reduced, the configurations including mid-chord and downstream row start to gain the advantage in terms of area-averaged effectiveness as shown in Fig. 16. Lastly, when the upstream injection angle is 50^{o}, while the axial row remains the benefit due to the strong contribution from the 2^{nd} and 3^{rd} row, the performance of cross row and cluster further decreases. Therefore, regarding the area-averaged effectiveness, the mid-chord and the downstream row configurations outperform the cross row and cluster configurations even under the condition that part of the film coverage from the downstream row is not taken into consideration (out of AOI). It is always important to bear in mind that as the cooling holes on the turbine vane endwall experience complicated flow field, it is better to consider both the local coolant distribution from contour plots and the averaged effectiveness when evaluating a particular cooling design. Therefore, the axial row configuration has the best overall performance concerning both local and averaged effectiveness in all the upstream injection angles in this study. However, from the results and the above descriptions, we can further reach an argument that for endwall with the film holes arranged before the throat, the cooling performances of those holes are heavily based on whether the upstream leakage (if there is) can sufficiently suppress the vortices (horseshoe, corner) at the same time contribute to downstream through film accumulation.

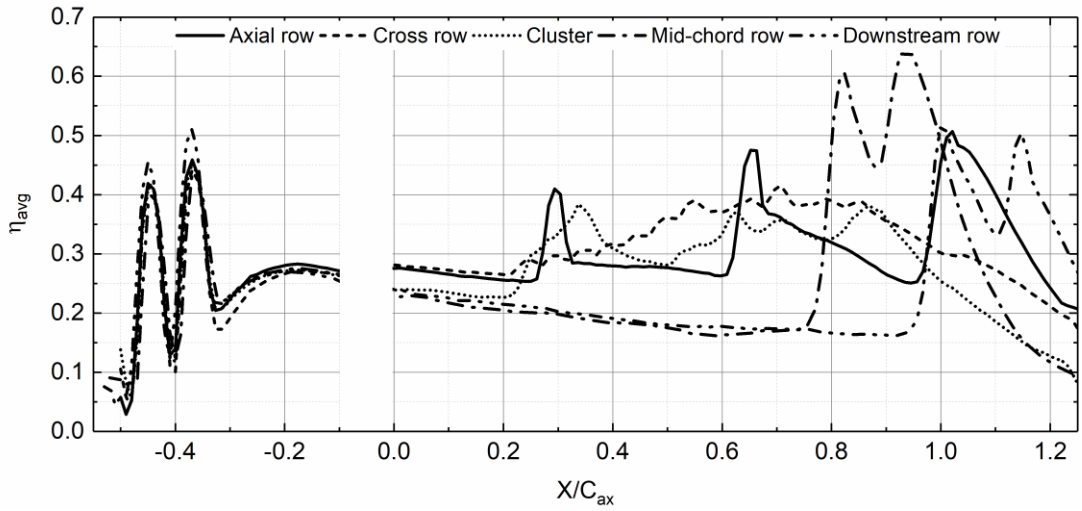

Figure 54. Laterally (spanwise) averaged film cooling effectiveness when upstream leakage injection angle is 30º.

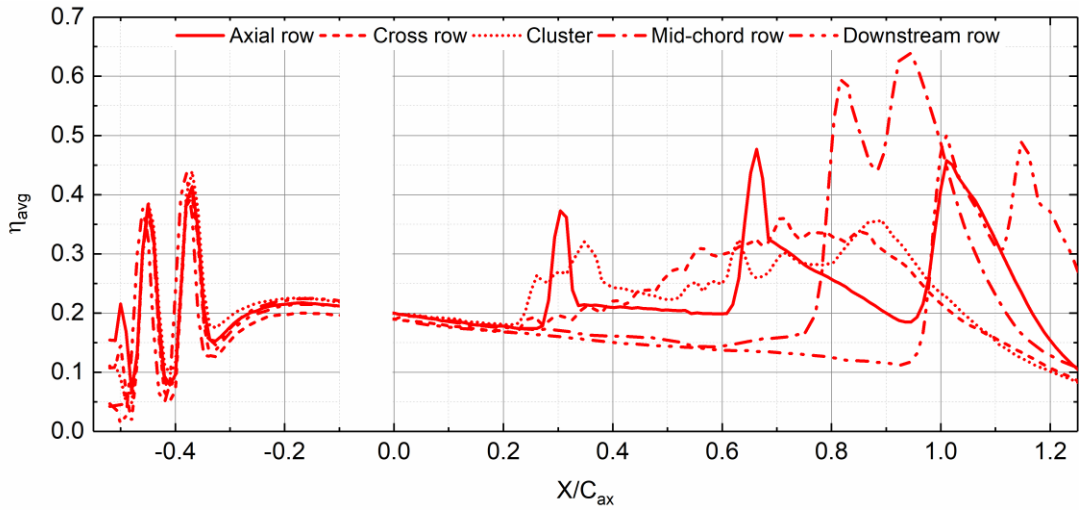

Figure 55. Laterally (spanwise) averaged film cooling effectiveness when upstream leakage injection angle is 40º.

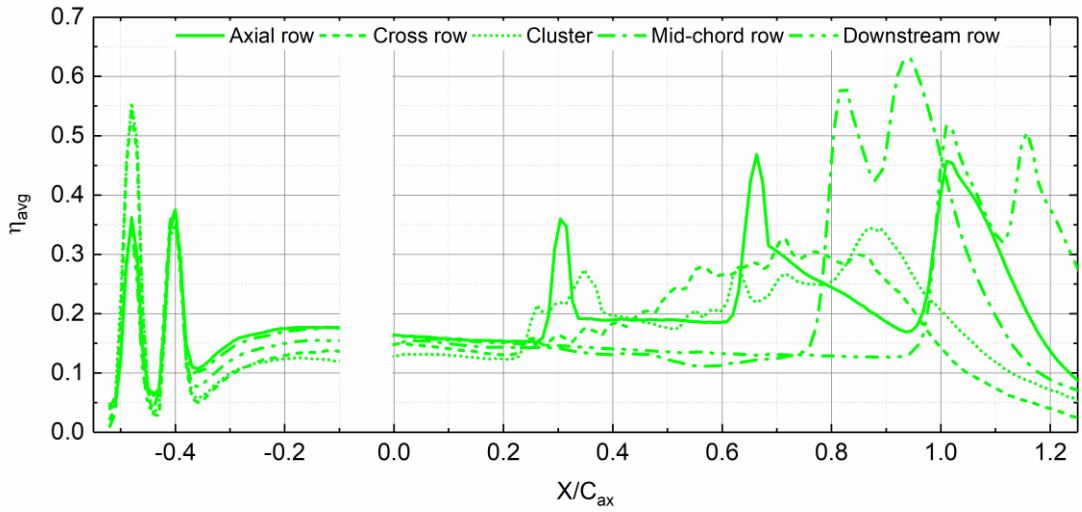

Figure 56. Laterally (spanwise) averaged film cooling effectiveness when upstream leakage injection angle is 50º.

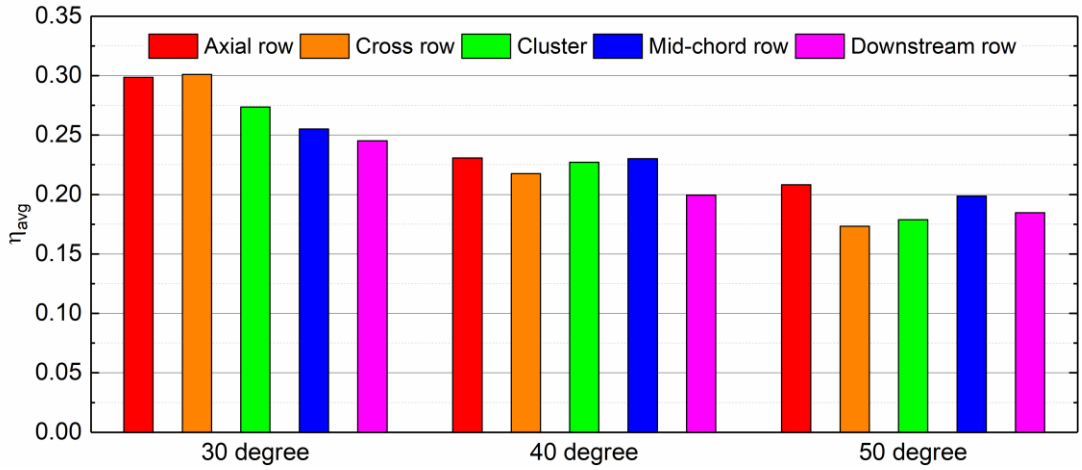

Figure 57. Area-averaged film cooling effectiveness for all the design combinations.

6. CONCLUSIONS

6.1 Film Cooling Effectiveness Comparison on Full-Scale Turbine Vane Endwalls

Film cooling effectiveness measurements on the inner endwall were conducted on a three-vane annular sector cascade with full-scale vane geometry. The influences of different MFR (MFR = 2%, 3%, 4%), DR (DR = 1.0, 1.5) on the film cooling effectiveness were performed on two different endwall cooling designs, respectively. A one-to-one cooling performance comparison of these two designs was also carried out. The key highlights of the presented study are as below:

a) The endwall film-hole arrangement, as well as the cooling hole arrangement inside the slashface, affect the corresponding local flow field which further influences the film cooling effectiveness distribution.

b) The higher the MFR, the longer the coolant trace, which implies the better film cooling distribution especially in the streamwise direction.

c) The larger the DR, the higher the film cooling effectiveness is obtained. The denser coolant, the better lateral spreading can be achieved. The lower momentum from denser coolant also leads to easy coolant deflection by the mainstream flow.

d) One-to-one cooling performance comparison is realized on the same full-scale endwall geometry with two different film-hole configurations. The results indicate a more uniform coolant coverage as design1 can be considered a better endwall cooling hole configuration on this particular vane/endwall geometry. However,

based on the current results, design2 can be further improved as suggested in the study.

6.2 Transonic Turbine Vane Suction Side Film Cooling with Showerhead Effect

Static pressure and film cooling effectiveness measurements on the vane suction side were conducted on a five-vane annular sector cascade. The influences of different M (M = 0.7, 1.0, 1.6), DR (DR = 1.0, 1.5, 2.0), and exit Ma (Ma = 0.7, 0.9, 1.1) on the film cooling effectiveness were performed. The key highlights of the presented study are as below:

a) A clear view capturing the film cooling distribution on the suction side of the vane in an annular sector cascade under the transonic condition is achieved by using PSP technique.
b) Due to the hole located in high curvature and acceleration zone, coolant jets tend to lift-off. Blowing ratio shows a negative effect on effectiveness for low density coolant. By adopting heavier density, the reduced coolant momentum results in higher optimal blowing ratio.
c) Heavy density coolant delays the cooling jet separation from vane surface. Density ratio effect is more prominent for higher blowing ratio as the jets need to have at least sufficient momentum.
d) Exit Mach number shows a positive effect by having thinner boundary layer and facilitates the jet to bend toward the surface. At supersonic flow, the effectiveness is enhanced by providing coolant with higher momentum such that the jets

penetrating to the mainstream are forced to stay parallel to surface due to the oblique shock wave.

e) For the engine-like temperature condition (DR = 2.0), increasing blowing ratio increases the LE coolant carryover. However, increasing blowing ratio leads to increasing then decreasing effectiveness on the majority of the vane's suction side. The supersonic flow with the shock wave is found to increase the film coverage only at the highest blowing ratio.

6.3 Turbine Vane Endwall Film Cooling Comparison from Different Film-Hole Patterns and Upstream Leakage Injection Angles

Film cooling effectiveness measurements on five different film-hole design patterns with three different upstream injection angles were performed on a four-passage linear cascade under a fixed coolant condition (MFR = 1%, DR = 1.5). The film cooling performance under different design combination is compared and discussed with regard to detailed film cooling effectiveness contours, spanwise averaged, as well as the area-averaged effectiveness.

The key highlights of the presented study are as below:

a) Increasing the upstream leakage injection angle has a negative effect on the downstream film cooling effectiveness due to the weaken streamwise momentum in exchange for the nearly useless vertical momentum.

b) Each endwall film-hole pattern has its unique flow/pressure distribution. This unique local flow distribution will influence how far the upstream leakage can penetrate/affect the entire endwall passage.

c) For film holes arranged before the throat of the endwall, the cooling performances of those holes are heavily based on whether the upstream leakage can sufficiently suppress the secondary flows (horseshoe and corner vortices) at the same time contribute to downstream through film accumulation.

d) Among the upstream injection angle range in this study, the axial row configuration has the best overall performance concerning both local and averaged effectiveness. Besides, the mid-chord and downstream row configurations outperform cross row and cluster in terms of area-averaged effectiveness when the upstream injection angle is 50^{o}.

REFERENCES

[1] Brooks, F. J., 1994, GE Gas Turbine Performance Characteristics, GE Power Systems, Schenectady, NY.

[2] Han, J. C., Dutta, S., and Ekkad, S., 2012, Gas Turbine Heat Transfer and Cooling Technology, 2nd edition, CRC Press- Taylor & Francis Group, Boca Raton, Florida.

[3] Goldstein, R. J., 1971, "Film Cooling," Advances in Heat Transfer, Vol. 7, Irvine, T. F., Jr and Hartnett, J. P., eds., Academic Press, New York, pp. 321-379.

[4] Han, J. C., 2013, "Fundamental Gas Turbine Heat Transfer," ASME J. Thermal Sci. Eng. Appl., 5(2), p. 021007.

[5] Luque, S. and Povey, T., 2010, "A Novel Technique for Assessing Turbine Cooling System Performance," ASME J. Turbomach., 133(3), p. 031013.

[6] Ligrani, P. M., Wigle, J. M., and Jackson, S. W., 1994, "Film-Cooling From Holes With Compound Angle Orientations: Part 2—Results Downstream of a Single Row of Holes With 6d Spanwise Spacing," ASME J. Heat Trans., 116(2), pp. 353-362.

[7] Schmidt, D. L., Sen, B., and Bogard, D. G., 1996, "Film Cooling With Compound Angle Holes: Adiabatic Effectiveness," ASME J. Turbomach., 118(4), pp. 807-813.

[8] Berhe, M. K. and Patankar, S. V., 1999, "Curvature Effects on Discrete-Hole Film Cooling," ASME J. Turbomach., 121(4), pp. 781-791.

[9] Gritsch, M., Colban W., Schär H., and Döbbeling K., 2005, "Effect of Hole Geometry on the Thermal Performance of Fan-Shaped Film Cooling Holes," ASME J. Turbomach., 127(4), pp. 718-725.

[10] Colban, W., Thole, K. A., and Haendler, M., 2008, "A Comparison of Cylindrical and Fan-Shaped Film-Cooling Holes on a Vane Endwall at Low and High Freestream Turbulence Levels," ASME J. Turbomach., 130(3), p. 031007.

[11] Bunker, R. S., 2005, "A Review of Shaped Hole Turbine Film-Cooling Technology," ASME J. Heat Trans., 127(4), pp. 441-453.

[12] Ekkad, S. and Han, J. C., 2015, "A Review of Hole Geometry and Coolant Density Effect on Film Cooling," Frontiers in Heat and Mass Transfer, 6(8).

[13] Pietrzyk, J. R., Bogard, D. G., and Crawford, M. E., 1990, "Effects of Density Ratio on the Hydrodynamics of Film Cooling," ASME J. Turbomach., 112(3), pp. 437-443.

[14] Sinha, A. K., Bogard, D. G., and Crawford, M. E., 1991, "Film-Cooling Effectiveness Downstream of a Single Row of Holes With Variable Density Ratio," ASME J. Turbomach., 113(3), pp. 442-449.

[15] Jones, T. V., 1999, "Theory for the use of foreign gas in simulating film cooling," International Journal of Heat and Fluid Flow, 20(3), pp. 349-354.

[16] Goldstein, R. J., Eckert, E. R. G., and Burggraf, F., 1974, "Effects of Hole Geometry and Density on Three-Dimensional Film Cooling," International Journal of Heat and Mass Transfer, 17(5), pp. 595-607.

[17] Pedersen, D. R., Eckert, E. R. G., and Goldstein, R. J., 1977, "Film Cooling With Large Density Differences Between the Mainstream and the Secondary Fluid Measured by the Heat-Mass Transfer Analogy," ASME J. Heat Trans., 99(4), pp. 620-627.

[18] Chen, A. F, Li, S. J., and Han, J. C., 2015, “Film Cooling for Cylindrical and Fan-Shaped Holes Using Pressure Sensitive Paint Measurement Technique,” AIAA J. Thermophys. Heat Transfer, 29(4), pp. 1-10.

[19] Vinton, K. R., Watson, T. B., Wright, L. M., Crites, D. C., Morris, M. C., and Riahi, A.,2016, "Combined Effects of Freestream Pressure Gradient and Density Ratio on the Film Cooling Effectiveness of Round and Shaped Holes on a Flat Plate," ASME Paper No. GT2016-56210.

[20] Narzary, D. P., Liu K. C., Rallabandi, A. P., and Han, J. C., 2011, "Influence of Coolant Density on Turbine Blade Film-Cooling Using Pressure Sensitive Paint Technique," ASME J. Turbomach., 134(3), p. 031006.

[21] Liu, K., Yang, S. F., and Han, J. C., 2014, "Influence of Coolant Density on Turbine Platform Film-Cooling With Stator–Rotor Purge Flow and Compound-Angle Holes," ASME J. Thermal. Sci. Eng. Appl., 6(4), p. 041007.

[22] Blair, M. F., 1974, "An Experimental Study of Heat Transfer and Film Cooling on Large-Scale Turbine Endwalls," ASME J. Heat Trans., 96(4), pp. 524-529.

[23] Langston, L. S., 1980, "Crossflows in a Turbine Cascade Passage," ASME J. Eng. Gas Turbine Power, 102(4), pp. 866-874.

[24] Graziani, R. A, Blair, M. F., Taylor, J. R., and Mayle, R.E., 1980, "An Experimental Study of Endwall and Airfoil Surface Heat Transfer in a Large Scale Turbine Blade Cascade," ASME J. Eng. Gas Turbine Power, 102(2), pp. 257-267.

[25] Goldstein, R. J. and Spores, R. A., 1988, "Turbulent Transport on the Endwall in the Region Between Adjacent Turbine Blades," ASME J. Heat Trans., 110(4a), pp. 862-869.

[26] Chyu, M. K., 2001, "Heat Transfer near Turbine Nozzle Endwall," Annals of the New York Academy of Sciences, 934(1), pp. 27-36.

[27] Takeishi, K., Matsuura, M., Aoki, S., and Sato, T., 1990, "An Experimental-Study of Heat-Transfer and Film Cooling on Low Aspect Ratio Turbine Nozzles," ASME J. Turbomach., 112(3), pp. 488-496.

[28] Harasgama, S. P. and Burton, C. D., 1992, "Film Cooling Research on the Endwall of a Turbine Nozzle Guide Vane in a Short Duration Annular Cascade: Part 1—Experimental Technique and Results," ASME J. Turbomach., 114(4), pp. 734-740.

[29] Jabbari, M. Y., Marston, K. C., Eckert, E. R. G., and Goldstein, R. J., 1996, "Film Cooling of the Gas Turbine Endwall by Discrete-Hole Injection," ASME J. Turbomach., 118(2), pp. 278-284.

[30] Friedrichs, S., Hodson, H. P., and Dawes, W. N., 1996, "Distribution of Film-Cooling Effectiveness on a Turbine Endwall Measured Using the Ammonia and Diazo Technique," ASME J. Turbomach., 118(4), pp. 613-621.

[31] Friedrichs, S., Hodson, H. P., and Dawes, W. N., 1997, “Aerodynamic Aspects of Endwall Film-Cooling,” ASME J. Turbomach., 119(4), pp. 786-793.

[32] Simon, T. W. and Piggush, J. D., 2006, "Turbine Endwall Aerodynamics and Heat Transfer," AIAA J. Propul. Power, 22(2), pp. 301-312.

[33] Kwak, J. S., Lee, J. H., and Han, J. C., 2002, "Heat Transfer and Pressure Distributions on A Gas Turbine Vane End-Wall," Proceeding of International Heat Transfer Conference, Grenoble, France.

[34] Barigozzi, G., Franchini, G., and Perdichizzi, A., 2006, "End-Wall Film Cooling through Fan-Shaped Holes with Different Area Ratios," ASME J. Turbomach., 129(2), pp. 212-220.

[35] Mahmood, G. I., Ross, G., and Sumanta, A., 2009, "Flow Dynamics and Film Cooling Effectiveness on a Non-Axisymmetric Contour Endwall in a Two-Dimensional Cascade Passage," ASME Paper No. GT2009-60236.

[36] Andrei, L., Facchini, B., Caciolli, G., Picchi, A., Tarchi, L., D'Ercole, M., Innocenti, L., and Russo, A., 2014, "Performance Improvement of a Heavy-Duty GT: Adiabatic Effectiveness Measurements on First Stage Vanes in Representative Engine Conditions," ASME Paper No. GT2014-26894.

[37] Cardwell, N. D., Sundaram, N., and Thole, K. A., 2005, "Effect of Midpassage Gap, Endwall Misalignment, and Roughness on Endwall Film-Cooling," ASME J. Turbomach., 128(1), pp. 62-70.

[38] Cardwell, N. D., Sundaram, N., and Thole, K. A., 2006, "The Effects of Varying the Combustor-Turbine Gap," ASME J. Turbomach., 129(4), pp. 756-764.

[39] Piggush, J. D. and Simon, T. W., 2012, "Flow Measurements in a First Stage Nozzle Cascade Having Endwall Contouring, Leakage, and Assembly Features," ASME J. Turbomach., 135(1), p. 011002.

[40] Roy, A., Jain, S., Ekkad, S. V., Ng, W. F., Lohaus, A. S., and Crawford, M. E., 2014, "Heat Transfer Performance of a Transonic Turbine Blade Passage in Presence of Leakage Flow Through Upstream Slot and Mateface Gap with Endwall Contouring," ASME Paper No. GT2014-26476.

[41] Shiau, C. C., Chen, A. F, Han, J. C., Azad, S., and Lee, C. P., 2016, “Full-Scale Turbine Vane Endwall Film-Cooling Effectiveness Distribution Using Pressure-Sensitive Paint Technique,” ASME J. Turbomach., 138(5), p. 051002.

[42] Chowdhury, N. H. K., Shiau, C. C., Han, J. C., Zhang, L., and Moon, H. K., 2016, “Turbine Vane Endwall Film Cooling with Slashface Leakage and Discrete Hole Configuration,” ASME J. Turbomach., 139(6), p. 061003.

[43] Chen, A. F, Shiau, C. C., and Han, J. C., 2016, “Turbine Blade Platform Film Cooling with Simulated Swirl Purge Flow and Slashface Leakage Conditions,” ASME J. Turbomach., 139(3), p. 031012.

[44] Baines, W. D. and Peterson, E. G., 1951, "An Investigation of Flow Through Screens," Trans. ASME, Vol. 73, pp. 467-480.

[45] Han, J. C. and Rallabandi, A. P., 2010, “Turbine Blade Film Cooling Using PSP Technique,” Frontiers in Heat and Mass Transfer, 1(1), pp. 1-21.

[46] Kline, S. J. and McClintock, F. A., 1953, "Describing Uncertainties in a Single Sample Experiment," Mechanical Engineering (Am. Soc. Mech. Eng.), 75, pp. 3-8.

[47] Ranson, W., Thole, K. A., and Cunha, F., 2005, “Adiabatic Effectiveness Measurements and Predictions of Leakage Flows Along a Blade Endwall,” ASME J. Turbomach., 127(3), pp. 609-618.

[48] Anderson, J. B., Wilkes, E. K., McClintic, J. W., and Bogard, D. G., 2016, “Effects of Freestream Mach number, Reynolds number, and boundary Layer Thickness of Film Cooling Effectiveness of Shaped Holes,” ASME Paper No. GT2016-56152.

[49] Liess, C., 1975, “Experimental Investigation of Film Cooling With Ejection From a Row of Holes for the Application to Gas Turbine Blades,” ASME J. Eng. Gas Turbine Power, 97(1), pp. 21-27.

[50] Gritsch, M., Schulz, A., and Wittig. S., 1998, “Adiabatic Wall Effectiveness Measurements of Film-Cooling Holes With Expanded Exits,” ASME J. Turbomach., 120(3), pp. 549-556.

[51] Lutum, E., von Wolfersdorf, J., Semmler, K., Naik, and S. Weigand, B., 2001, “Film cooling on a convex surface: influence of external pressure gradient and Mach number on film cooling performance,” Heat and Mass Transfer, 38(1), pp. 7-16.

[52] Ochs, M., Schulz, A., and Bauer, H. –J., 2007, “Investigation of the Influence of Trailing Edge Shock Waves on Film Cooling Performance of Gas Turbine Airfoils,” ASME Paper No. GT2007-27482.

[53] Saumweber, C. and Schulz, A., 2012, “Free-Stream Effects on the Cooling Performance of Cylindrical and Fan-Shaped Cooling Holes,” ASME J. Turbomach., 134(6), p. 061007.

[54] Xue, S., Arisi, A., and Ng. W., 2015, “Experimental and Numerical Investigations of Shock-Film Cooling Interaction on a Turbine Blade With Fan-Shaped Cooling Holes,” ASME J. Therm. Sci. Eng. Appl., 7(4), p. 044502.

[55] Wright, L. M., McCain, S. T., and Clemenson, M. D., 2011, “Effect of Density Ratio on Flat Plate Film Cooling With Shaped Holes Using PSP,” ASME J. Turbomach., 133(4), p. 041011.

[56] Colban, W. Gratton, A., Thole, K. A., and Haendler, M., 2005, “Heat Transfer and Film-Cooling Measurements on a Stator Vane With Fan-Shaped Cooling Holes,” ASME J. Turbomach., 128(1), pp.53-61.

[57] Najafabadi, H. N., Karlsson, M., Kinell, M., and Utriainen, E., 2015, “Film-Cooling Performance of a Turbine Vane Suction Side: The Showerhead Effect on Film-Cooling Hole Placement for Cylindrical and Fan-Shaped Holes,” ASME J. Turbomach., 137(9), p. 091005.

[58] Najafabadi, H. N., Karlsson, M., Utriainen, E., Kinell, and M., Wang, L., 2015, “Film-Cooling Performance of Multiple Arrays of Cylindrical and Fan-Shaped Holes,” AIAA J. Propul. Power, 31(6), pp. 1621-1630.

[59] Liu, K., Narzary, D. P., Han, J. C., Mirzamoghadam, A. V., and Riahi, A., 2011, “Influence of Shock Wave on Turbine Vane Suction Side Film Cooling with Compound-Angle Shaped Holes,” ASME Paper No. GT2011-45927.

[60] Yang, S. F., Han, J. C., Mirzamoghadam, A. V., and Riahi, A., 2015 “Film Cooling Effectiveness of Transonic Turbine Vane Suction Side with Compound-Angle Shaped Hole Configuration,” ASME Paper No. GT2015-42184.

[61] Shiau, C. C., Chowdhury, N. H. K., Yang, S. F., Han, J. C., Mirzamoghadam, A. V., and Riahi, A., 2016, “Heat Transfer Coefficients and Film Cooling Effectiveness of Transonic Turbine Vane Suction Surface Using TSP Technique,” ASME Paper No. GT2016-56264.

[62] Häring, M. and Weigand, B., 1995, “A New Analogy Function for The Naphthalene Sublimation Technique to Measure Heat Transfer Coefficients on Turbine Airfoils,” ASME Paper No. 95-GT-017.

[63] Häring, M., Hoffs, A., Bolcs, A., and Weigand, B., 1995, “An Experimental Study to Compare The Naphthalene Sublimation with The Liquid Crystal Technique in Compressible Flow,” ASME Paper No. 95-GT-016.

[64] Wright, L. M., Gao, Z., Varvel, T. A., and Han, J. C., 2005, “Assessment of Steady State PSP, TSP, and IR Measurement Techniques for Flat Plate Film Cooling,” ASME Paper No. HT2005-72363.

[65] Wiese, C. J., Rutledge, J. L., and Polanka, M. D., 2017, “Experimental Evaluation of Thermal and Mass Transfer Techniques to Measure Adiabatic Effectiveness with Various Coolant to Freestream Property Ratios,” ASME Paper No. GT2017-65019.

[66] Jones, T. V., 1999, “Theory for the use of foreign gas in simulating film cooling”, International Journal of Heat and Fluid Flow, 20(3), pp. 349-354.

[67] Granser, D. and Schulenberg, T., 1990, “Prediction and Measurement of Film Cooling Effectiveness for a First-Stage Turbine Vane Shroud,” ASME Paper No. 90-GT-95.

[68] Burd, S. W. and Simon, T. W., 2000, “Effects of Slot Bleed Injection Over a Contoured Endwall on Nozzle Guide Vane Cooling Performance: Part I: Flow Field Measurements,” ASME Paper No. 2000-GT-199.

[69] Burd, S. W., Satterness, C. J., and Simon, T. W., 2000. “Effects of Slot Bleed Injection Over a Contoured Endwall on Nozzle Guide Vane Cooling Performance: Part II: Thermal Measurements,” ASME Paper No. 2000-GT-200.

[70] Oke, R., Simon, T., Shih, T., Zhu, B., Lin, Y. L., and Chyu, M., 2001. “Measurements Over a Film-Cooled, Contoured Endwall with Various Coolant Injection Rates,” ASME Paper No. 2001-GT-140.

[71] Oke, R. and Simon, T., 2002, “Film-Cooling Experiments with Flow Introduced Upstream of a First Stage Nozzle Guide Vane through Slots of Various Geometries,” ASME Paper No. GT2002-30169.

[72] Oke, R., Simon, T. W., Burd, S. W., and Vahlberg, R., 2000, “Measurements in a Turbine Cascade Over a Contoured Endwall: Discrete Hole Injection of Bleed Flow,” ASME Paper No. 2000-GT-0214.

[73] Zhang, L. and Jaiswal, R. S., 2001, “Turbine Nozzle Endwall Film Cooling Study Using Pressure-Sensitive Paint,” ASME J. Turbomach., 123(4), pp. 730-738.

[74] Liu, G., Liu, S., Zhu, H., Lapworth, B. C., and Forest, A.E., 2004, “Endwall Heat Transfer and Film Cooling Measurements in a Turbine Cascade with Injection Upstream of Leading Edge,” Heat Transfer–Asian Research, 33, pp. 141-152.

[75] Knost, D. G. and Thole, K. A., 2005, “Adiabatic Effectiveness Measurements of Endwall Film-Cooling for a First-Stage Vane,” ASME J. Turbomach., 127(2), pp. 297-305.

[76] Zhang, L., Yin, J., Liu, K., and Moon, H. K., 2015, “Effect of Hole Diameter on Nozzle Endwall Film Cooling and Associated Phantom Cooling,” ASME Paper No. GT2015-42541.

[77] Chowdhury, N. H. K., Shiau, C. C., Han, J. C., Zhang, L., and Moon H. K., 2017, “Turbine Vane Endwall Film Cooling Study from Axial-Row Configuration with Simulated Upstream Leakage Flow,” ASME Paper No. GT2017-63144.

[78] Chowdhury, N. H. K., Shiau, C. C., Han, J. C., Zhang, L., and Moon H. K., 2017, “Turbine Vane Endwall Film Cooling from Cross-Row Configuration with Simulated Upstream Leakage Flow,” ASME Paper No. GT2017-63145.

[79] Chowdhury, N. H. K., Shiau, C. C., Han, J. C., Xu, H., and Fox M., 2017, “Film Cooling Effectiveness Comparison on Turbine Vane Endwall with Cluster Configurations Using PSP Measurement Technique," ASME Paper No. IMECE2017-72157.

[80] Foster N. W. and Lampard, D., 1984, "The Flow and Film Cooling Effectiveness Following Injection through a Row of Holes," ASME J. Eng. Power, 102(3), pp. 584-588.

[81] Kohli, A. and Bogard D. G., 1997, "Adiabatic Effectiveness, Thermal Fields, and Velocity Fields for Film Cooling with Large Angle Injection," ASME J. Turbomach., 119(2), pp. 352-358.

[82] Kohli, A. and Bogard, D. G., 1999, "Effects of Hole Shape on Film Cooling with Large Angle Injection," ASME Paper No. 99-GT-165.

[83] Baldauf, S., Schulz, A., and Wittig, S., 1999, "High-Resolution Measurements of Local Effectiveness from Discrete Hole Film Cooling," ASME J. Turbomach., 123(4), pp. 758-765.

[84] Yuen, C. H. N. and Martinez-Botas, R. F., 2003, " Film cooling characteristics of a single round hole at various streamwise angles in a crossflow: Part I effectiveness," International Journal of Heat and Mass Transfer, 46(2), pp. 221-235.

[85] Yuen, C. H. N. and Martinez-Botas, R. F., 2005, " Film cooling characteristics of rows of round holes at various streamwise angles in a crossflow: Part I. Effectiveness," International Journal of Heat and Mass Transfer, 48(23), pp. 4995-5016.